

Bachelor's Degree in Aerospace Engineering
Aerospace Engineering Department (UC3M)
Academic Year 2017-2018

Bachelor Thesis

Electromagnetic wave propagation and absorption in electrodeless plasma thrusters

Pedro José Jiménez Jiménez

Supervised by
Dr. Mario Merino Martínez
Madrid, September 2018



This work is licensed under Creative Commons **Attribution – Non Commercial – Non Derivatives**

Universidad Carlos III de Madrid
Bioengineering and Aerospace Department
Bachelor Thesis

Abstract

Electromagnetic wave propagation and absorption in electrodeless plasma thrusters

by Pedro José Jiménez Jiménez

The thesis aims at developing a numerical code to study the electromagnetic wave-plasma interaction phenomena critical for the operation of electrodeless thrusters, particularly, the Electron Cyclotron Resonance (ECR) Thruster under development in the European H2020 MINOTOR project.

Current in-space Electric Propulsion technologies are presented with special attention to their advantageous characteristics compared to conventional techniques. Among those, electrodeless thrusters emerge as efficient and durable alternatives for future propulsion systems. The main limitation hindering the implementation of these devices is the complicated physical phenomena governing the fundamental operational stages i.e. the plasma heating and ionization, and the acceleration of charged particles.

The present work is devoted to the study of the plasma heating mechanism by electromagnetic wave interaction. As presented in the chapter on electromagnetic theory, this is a complex physical problem with a considerable amount of phenomena going on; such as absorption, reflection, resonance or cutoff. Numerical methods are a suitable tool to address the specific behavior taking place inside a thruster and better understand the physics underneath. Furthermore, future numerical codes should be capable of simulating the complete thruster operation by integrating the plasma wave interaction code with additional ion and neutral, electron, and magnetic nozzle codes. Full simulations will serve to shorten design cycles and complement laboratory testing during the preliminary design phase.

This thesis mainly focuses on the implementation and verification of the 2D wave-plasma code *fdwaves* while presenting important concepts on electromagnetism, plasma physics and numerical methods. Specifically, a two dimensional Finite Difference and Frequency Domain method is used to discretize the Maxwell's Equations.

Numerical wave normal surfaces are plotted using von Neumann stability analysis implemented in the *wave-explorer* code and compared using solutions to the analytic dispersion relation. This is shown to be truly useful to evaluate the behavior of numerical schemes in terms of spurious propagation and divergence from the physical solution.

Preliminary results are shown, firstly, propagation through vacuum serving as a verification method for the code due to the existence of straightforward analytic solutions, then, wave behavior in homogeneous cold plasma media is presented.

The work carried out in this thesis is intended to be continued in the future, as a consequence, a considerable number of tools currently under study or development are presented. Special mention should be made of the new code for arbitrary geometry simulation *fdmesher*, non-uniform grids and the Perfectly Matched Layer (PML) boundary conditions.

Keywords: Electric Propulsion, Electrodeless Thrusters, ECR Thruster, Plasma Physics, Computational Electromagnetism, Finite Difference Methods, Electromagnetic Waves

Agradecimientos/Acknowledgments

En primer lugar, debo dar las gracias a mi tutor Mario Merino. Han sido muchas las horas en reuniones y resolviendo innumerables dudas. Considero que su implicación en este proyecto ha sido extraordinaria. También debo agradecerle el interés que me ha inculcado hacia la investigación y la confianza que ha depositado en mí para seguir colaborando con él.

A mis padres y mi hermano, que siempre me han apoyado y que han potenciado desde que era pequeño mi curiosidad y ganas de aprender. Mis compañeros de carrera han sido un apoyo fundamental, ellos comprenden mejor que nadie lo que significa este proyecto.

Finalmente, me gustaría dar las gracias a la Universidad Carlos III como institución y en su nombre, a todos los profesores y personal que me han proporcionado una educación de calidad durante los últimos cuatro años. Gracias a esta universidad tuve la oportunidad de estudiar un año en Estados Unidos, realizar prácticas en un líder mundial en el sector aeroespacial y vivir una experiencia de introducción a la investigación que ha dado como resultado este trabajo. He asistido a clases impartidas por profesores brillantes y, ante todo, he conocido a personas excepcionales. En definitiva, finalizo mis estudios en el grado de Ingeniería Aeroespacial aún más convencido que cuando llegué de que este es el mejor lugar para mi formación.

Contents

List of Symbols	9
List of Figures	11
List of Tables	15
1 Introduction	16
1.1 Motivation	16
1.2 Objectives	16
1.3 Project Budget	17
1.4 Socio-Economic and Regulatory Environment	18
2 Electric Propulsion and State of the Art	20
2.1 Overview	20
2.2 Types of Thrusters	23
2.3 State of the Art: Electrodeless Thrusters	24
2.3.1 ECR Thrusters	25
2.3.2 ECRA and the MINOTOR Project	26
2.4 State of the Art: Numerical methods for the wave-plasma interaction problem	27
3 Electromagnetic Waves in Plasma	28
3.1 Basic Electromagnetic Theory	28
3.1.1 Maxwell's Equations	28
3.1.2 The Dispersion Relation	30
3.2 Waves in a cold plasma	31
3.2.1 Plasma dielectric tensor	31
3.2.2 Wave Phase and Polarization	34
3.2.3 Wave normal surfaces, cutoff and resonance and the CMA diagram	35
3.2.4 The Electron Cyclotron Resonance	38
4 Finite Difference Methods	40
4.1 Problem formulation: Frequency domain method	41
4.2 Scheme Equations	43

4.2.1	Non staggered grid: Sofd3 scheme	43
4.2.2	Yee staggered grid modification: Sofd5 scheme	45
4.3	Boundary conditions	46
4.3.1	Periodic Conditions	46
4.3.2	Perfect Electric Conductor (PEC)	47
5	Von Neumann Analysis of Numerical Dispersion	49
5.1	Formulation	49
5.2	The <i>wave-explorer</i> tool	50
5.3	Numerical wave normal surfaces	53
5.3.1	Vacuum: Grid Anisotropy	54
5.3.2	Magnetize Collisionless plasma: Static Magnetic Field Anisotropy	56
5.3.3	Collisional plasma: Damping	58
5.4	Non-uniform grid wave normal surfaces	59
6	Simulation software: <i>fdwaves</i>	60
6.1	Preprocessor	60
6.1.1	Mesh and Node Classification	61
6.1.2	Forcing terms: Sofd5 Grid Uncoupling	62
6.2	Coefficient Assembler and Solver	63
6.3	Computational Performance and Limitations	66
6.4	Finite difference method accuracy: Analytic Solutions	67
6.5	Finite difference method accuracy: Convergence	69
6.5.1	Vacuum Convergence	71
6.5.2	Plasma Convergence	71
6.5.3	Z-Harmonic Field Convergence	73
6.5.4	In-plane dipole antenna convergence	73
6.5.5	Order of the simulation from convergence plot	74
7	Analysis of solutions	75
7.1	Eigenfrequencies of a resonant cavity (PEC)	75
7.1.1	Vacuum Resonant Modes in a Rectangular Cavity	77

7.1.2	Vacuum Resonant Modes with Complex Geometry	83
7.1.3	Plasma Resonant Modes	84
7.2	ECR waves in Plasma	85
8	Future work	89
8.1	Non-uniform grids: <i>fdschemes</i>	89
8.2	Arbitrary geometry: <i>fdmesher</i> code	92
8.3	Types of Meshes	92
8.3.1	Mesh construction	93
8.4	Interpolation	94
8.5	Expected Issues and Limitations	96
8.6	Perfectly Matched Layer (PML)	96
9	Concluding Remarks	97

List of Symbols

The following table shows symbols used across the thesis, the associated definition and the most used International System units. The second table also presents useful fundamental constants and their value in SI units.

Symbol	Definition	SI Units
\mathbf{E}	Electric field vector	N/C or V/m
\mathbf{B}	Magnetic flux density vector (magnetic induction)	T or V s/m ²
ρ	Electric charge density	C/m ³
ω	Monochromatic wave angular excitation frequency	rad/s
\mathbf{j}	Current density vector	A/m ²
$\bar{\bar{\kappa}}$	Dielectric tensor	Non-dimensional
$\bar{\bar{\chi}}$	Susceptibility tensor	Non-dimensional
$\bar{\sigma}$	Conductivity tensor	S/m
$\hat{\mathbf{E}}$	Time-expanded electric field complex amplitude	N/C or V/m
$\hat{\mathbf{j}}$	Time-expanded current density complex amplitude	A/m ²
$\tilde{\mathbf{E}}$	Space-time-expanded electric field complex amplitude	N/C or V/m
$\tilde{\mathbf{j}}$	Space-time-expanded current density complex amplitude	A/m ²
\mathbf{k}	Wave number vector or spatial frequency	1/m
\mathbf{n}	Electric length normalized wave number vector (refractive index)	Non-dimensional
q_s	Charge of species s	C
m_s	Mass of species s	kg
n_s	Number density of species s	1/m ³
\mathbf{v}_s	Velocity vector of species s	1/m ³
ω_{ps}	Plasma frequency	rad/s
Ω_e	Electron Cyclotron frequency	rad/s
Ω_i	Ion Cyclotron frequency	rad/s
B_0	Background Magnetic Flux Density	T
ν_m	Effective momentum transfer collision frequency	1/s
λ	Ion-to-electron mass ratio	Non-dimensional
$\hat{\mathbf{x}}$	Unitary vector in x-direction (Cartesian basis)	Non-dimensional
$\hat{\mathbf{y}}$	Unitary vector in y-direction (Cartesian basis)	Non-dimensional
$\hat{\mathbf{z}}$	Unitary vector in z-direction (Cartesian basis)	Non-dimensional
t	Time	s
\mathbf{r}	Position vector	m
Z	Ion normalized charge	Non-dimensional

Table 1: List of symbols

Constant	Definition	Value SI Units
ϵ_0	Vacuum electric permittivity	8.854188×10^{-12} F/m
μ_0	Vacuum magnetic permeability	$4\pi \times 10^{-7}$ H/m
c	Vacuum light speed	2.997925×10^8 m/s
q_e	Electron or fundamental charge	$-1.602177 \times 10^{-19}$ C
m_e	Electron rest mass	9.109384×10^{-31} kg

Table 2: List of constants

List of Figures

1.1	The global space economy at a glance (2016). Courtesy of Bryce Space and Technology [10]	18
2.1	Payload ratio for a $\Delta v = 10^4 m/s$ mission with several structural mass ratios	21
2.2	Several Plasma Thrusters. Schematic of working principle [1]	23
2.3	Schematic of the ECR prototype built by ONERA	25
2.4	MINOTOR Logo	26
3.1	Circular Polarization with respect to the propagation direction [4]	35
3.2	Wave normal surfaces of a fast wave (exterior in (a)) and an ion cyclotron wave. Figure (a) corresponds to Stix's [44] representation with $u = 1/n$, namely phase velocity, and (b) was obtained with <i>wave-explorer</i> for n , namely normalized wave number or index of refraction.	36
3.3	Clemmow-Mullaly-Allis diagram for the classification of waves in a cold plasma [44]	37
4.1	Sofd3 Computational Cell	43
4.2	Sofd5 Computational Cell	45
4.3	1D vacuum simulation at 500MHz. Central foil of current in z-direction. Showing the norm of E_z field. PEC lateral walls.	46
5.1	Contour plots for numerical dispersion Sofd3 left and analytic dispersion right. The points of intersection are solutions. Note that the numerical scheme has spurious solutions.	51
5.2	<i>Wave-explorer</i> code Flow Chart	52
5.3	Vacuum numerical wave normal surfaces of the finite difference schemes Sofd3 and Sofd5 with $h = 0.2c/\omega$ and uniform stencils. Continuous line representing the real part of the refractive index. Discontinuous line representing the imaginary part of the refractive index. Different colors for different branches.	54
5.4	Zoom at the Analytic (Black), Sofd3 scheme (Red) and Sofd5 scheme (Green) normal surfaces with $h = 0.8c/\omega$ and uniform stencils. Continuous line representing the real part of the refractive index. Discontinuous line representing the imaginary part of the refractive index.	55
5.5	Numerical wave normal surfaces for Sofd3 FD scheme with $\omega_{pe} = 1.5\omega$ and $\omega_{ce} = 2\omega$. Node distance $h = 0.2c/\omega$ and uniform stencil. Discontinuous line representing the imaginary part of the refractive index. Different colors for different branches.	56
5.6	Numerical wave normal surfaces for Sofd5 FD scheme with $\omega_{pe} = 1.05\omega$ and $\omega_{ce} = 2\omega$. Node distance $h = 0.2c/\omega$ and uniform stencil. Continuous line representing the real part of the refraction index. Discontinuous line representing the imaginary part of the refractive index. Different colors for different branches.	57

5.7	Numerical wave normal surfaces for Sofd5 FD scheme with $\omega_{pe} = 1.5\omega$ and $\omega_{ce} = 2\omega$ at different static magnetic field \mathbf{B}_0 angles. Node distance $h = 0.2c/\omega$ and uniform stencil. No collisions. Continuous line representing the real part of the refractive index. Discontinuous line representing the imaginary part of the refractive index. Different colors for different branches.	57
5.8	Numerical wave normal surfaces for Sofd3 FD scheme with $\omega_{pe} = 1.5\omega$ and $\omega_{ce} = 2\omega$ with different collision frequencies. Magnetic field align with x-axis. Node distance $h = 0.2c/\omega$ and uniform stencil. Continuous line representing the real part of the refractive index. Discontinuous line representing the imaginary part of the refractive index. Different colors for different branches.	58
5.9	Non Uniform Stencil Vacuum Numerical Wave Normal Surfaces, red (Sofd3) and green (Sofd3). Continuous line representing the real part of the refraction index. Discontinuous line representing the imaginary part of the refractive index.	59
6.1	<i>fdwaves</i> code Flow Chart	60
6.2	Preprocessor package Flow Chart	61
6.3	Node classification from boundary type input. 0 \rightarrow Center Node, 1 \rightarrow Neighbor Node, 2 \rightarrow Right Wall, 3 \rightarrow Left Wall, 4 \rightarrow Upper Wall, 5 \rightarrow Lower Wall, 5 \rightarrow Corner	62
6.4	Sofd5 uncoupling issue and Gaussian Forcing model of a perpendicular antenna. In a real simulation the function is sharper around the central excitation node.	63
6.5	Simulation domain layout for the tests	64
6.6	Complete set of solution fields of an electromagnetic problem. Simulation with $k_z = 0$, field shown at $z = 2m$ and $t = 7.5s$. Vacuum. Cartesian mesh with 401×401 nodes	65
6.7	Complete set of solution fields of an electromagnetic problem. Simulation with $k_z = 0$, field shown at $z = 2m$ and $t = 7.5s$. Plasma parameters $\omega_{pe} = 1.5\omega$, $\Omega_{ce} = 2\omega$, $\nu_m = 0.5\omega$. Excitation angular frequency $\omega = 3.3301 \times 10^9 rad$. Cartesian mesh with 401×401 nodes	65
6.8	Residual error between interactions and elapsed time as a function of the number of nodes. Simulation with $k_z = 0$. Plasma parameters $\omega_{pe} = 1.5\omega$, $\Omega_{ce} = 2\omega$, $\nu_m = 0.2\omega$. Excitation angular frequency $f = 1.5GHz$	66
6.9	Elapsed time in <i>fdwaves</i> functions. Plasma Simulation with 401×401 nodes.	67
6.10	Maximum error in the field norm. Sofd3 scheme in vacuum, periodic conditions $\bar{h}_x = \bar{h}_y = 0.2$. 2500 simulations with different \bar{k}_x and \bar{k}_y . Configurations inside the Nyquist sampling box (red line).	68
6.11	Numerical Field Norm and Phase Error $\bar{h}_x = \bar{h}_y = 0.1$. Analytic periodic wave with $\bar{k}_x = k_x \times c/\omega = 20$ and $\bar{k}_y = 10$	69
6.12	Vacuum Convergence Plots.	71
6.13	Plasma Convergence Plots at $f=2.95GHz$. Cold plasma with parameters $\Omega_{ce} = 2\omega$, $\omega_p = 1.5\omega$. Ions assume static due to low mobility. Electron collisionality indicated in each plot. Magnetic field aligned with x-axis.	72
6.14	Plasma Convergence Plots at $f=2.95GHz$. Not aligned background magnetic field, θ denotes the angle with the x-axis. Cold plasma with parameters $\Omega_e = 2\omega$, $\omega_p = 1.5\omega$. Ions assume static due to low mobility. Electron collisionality indicated in each plot.	72

6.15	Convergence Plots with propagation in z-direction, $k_z = 1.3$, $f=295\text{MHz}$	73
6.16	Convergence Plots with a central dipole antenna, $f=2.95\text{GHz}$. The simulation has been extended to a larger number of nodes.	73
6.17	Power fit to the err vs. nodes convergence plot of an arbitrary plasma simulation. . . .	74
7.1	ECR domain for the full simulation objective [37]	75
7.2	Comparison of peak amplitudes near two eigenvalues of \bar{C} under TM_z mode excitation. 51 simulations per plot with 100×100 cells per domain. 10 random antennas at random phases and magnitudes (1 to 10 A).	78
7.3	Eigenmodes (as field norm) representation for a confirmed resonance and an unidentified eigenvalue. Notice that these are modal shapes, the eigenvector is normalized to unity. 101×101 degrees of freedom.	79
7.4	Two simulation results using <i>fdwaves</i> at an arbitrary (non resonant) frequency. 1m x 1m PEC cavity with 10 random antennas perpendicular to the propagation plane at random phases and magnitudes (-5A to 5A). 101×101 nodes, Sofd3 FD scheme.	80
7.5	Principal resonant modes. 1m x 1m PEC cavity with 10 random antennas perpendicular to the propagation plane at random phases and magnitudes (-5A to 5A). 101×101 nodes, <i>fdwaves</i> Sofd3 FD scheme.	81
7.6	Simulation results using <i>fdwaves</i> at an off-diagonal eigenfrequency. 1m x 1m PEC cavity with 1 central antenna perpendicular to the propagation plane (1A and 0 rad phase shift). 101×101 nodes, Sofd3 FD scheme.	82
7.7	Two simulation results using <i>fdwaves</i> at an off-diagonal eigenfrequency. 1m x 1m PEC cavity with 10 random antennas perpendicular to the propagation plane at random phases and magnitudes (-5A to 5A). 101×101 nodes, Sofd3 FD scheme.	83
7.8	Resonant field in a complex geometry PEC cavity. 10 random antennas perpendicular to the propagation plane at random phases and magnitudes (-5A to 5A). 101×101 nodes, <i>fdwaves</i> Sofd3 FD scheme.	84
7.9	Resonant field in a complex geometry PEC cavity. 10 random antennas perpendicular to the propagation plane at random phases and magnitudes (-5A to 5A). 101×101 nodes, <i>fdwaves</i> Sofd3 FD scheme.	85
7.10	Interference pattern from reflection, quasi-standing ECR waves. Plasma parameters $\Omega_e = 2\omega$, $\omega_p = 2\omega$, $\nu_e = 0.1\omega$. 501×501 nodes <i>fdwaves</i> simulation	86
7.11	Highly damped ECR waves, E_z field phase. Plasma parameters $\Omega_e = 2\omega$, $\omega_p = 2\omega$, $\nu_e = 0.8\omega$. Magnetic field at 30deg with x-axis. Excitation frequency $f=1.5\text{GHz}$. 501×501 nodes <i>fdwaves</i> simulation	87
7.12	E_z field Logarithmic Scale of the field shown in Figure 7.11	87
7.13	Spurious free normal surfaces, high precision $h = 0.005c/\omega$. Fast L wave (red), R wave (green). Plasma parameters $\Omega_e = 2\omega$, $\omega_p = 2\omega$, $\nu_e = 0.8\omega$. Magnetic field at 30deg with x-axis.	88
7.14	Resonant cones and R wave fronts with high and low collisionality.	88
8.1	Truncation error as a function of the node spacing. First derivative with $s = [0, 1, 3]$ stencil. Results show $b=2.026$ in the power curve fitting $f(x) = ax^b$. We conclude that this scheme is order 2.	91

8.2	Mesh created with <i>fdmesher</i> , 233728 nodes, maximum curvature limited to 0.47 deg. . .	92
8.3	Wall Mesh Structure	93
8.4	Comparison of nearest-neighbour, linear, cubic, bilinear and bicubic interpolation methods courtesy of CMG Lee [16]. The black dots correspond to the point being interpolated, and the red, yellow, green and blue dots correspond to the neighbouring samples.	95
8.5	Relative Error in the Bicubic Interpolation of a sinusoidal function with 10 wavelengths per domain. Real wall nodes from the mesh shown in Figure 8.2 were used.	95
8.6	Perfectly Matched Layer (PML) boundary conditions schematic.	96

List of Tables

1	List of symbols	9
2	List of constants	10
3	Theoretical Specific Impulses for several types of propulsion systems [35]	22
4	Arrangement of coefficients in \bar{M} . Where i_u, j_u, c_u denote the node computational coordinates and the Cartesian component (x, y, z) of the unknown or degree of freedom. Similarly, i_e, j_e, d_e are used for the equation in a node defined by the coordinates (i_e, j_e) and in the direction established by $d_e \equiv (x, y, z)$	63
5	Resonant Frequencies of a cavity with dimensions $L_x = 1m$ and $L_y = 1m$ in vacuum .	77

1 Introduction

1.1 Motivation

Despite having been studied and flown for many decades, the last few years have seen the advent of electric propulsion technologies as powerful alternatives to chemical propulsion for in-space applications. The prospects for the future are equally optimistic.

On March 2015 the first all-electric communication satellites, the ABS 3A and Eutelsat 115 West B, were launched. Both were built in the Boeing 702SP platform. Their Xenon Electrostatic ion thruster System (XIPS) was able to perform both insertion to geostationary orbit and station keeping up to 10 times more fuel efficiently than a conventional liquid apogee engine [14]. Furthermore, an increasing number of small satellites such cubeSats are adopting different Electric Propulsion systems for attitude control and station keeping.

Regarding Deep Space exploration, the Dawn mission to Vestas and Ceres (NASA), BepiColombo Mercury Explorer and SMART-1 (ESA) or the Japanese probe Hayabusa to the asteroid Itokawa [31] are among the examples showing that electric propulsion is not only the future of in-space propulsion but it has actually been used to accomplish extraordinary scientific missions.

This ‘New Dawn’ [13] for electric propulsion could represent, together with the arrival of reusable and cheaper launchers, a new revolution in space technology leading to breakthroughs not seen since the Cold War era. Among the electric propulsion technologies, *electrodeless thrusters* represent a new generation of more efficient and durable systems.

1.2 Objectives

Despite the good performance expectations, the complicated mechanisms governing the physics inside this kind of thrusters limit their current applicability. As it will be shown throughout this thesis, plasma heating by interaction with electromagnetic waves comprises complex phenomena under extensive research. Working thruster prototypes are extremely expensive both due to the infrastructure required (vacuum chambers) and their actual components. Furthermore, plasma and thrust diagnostics are complicated.

Experiments will always be necessary for design and verification, nonetheless, specially during preliminary design phases, numerical models capable of accurately simulating real devices are an important and necessary complement to the experimental approach. This allows for rapid prototyping and reduces the design cycles. However, guaranteeing the accuracy of these codes whilst simulating complex features and subtleties of the actual physical problem is not an easy task. This thesis addresses the development of one such numerical models through a series of objectives:

1. To provide a concise overview of electric propulsion technologies and the design alternatives.
2. To present the theoretical background needed to understand the wave propagation phenomena.
3. To study the fundamental characteristics of numerical methods, particularly, different alternatives for Finite Difference discretizations and their validity and accuracy in vacuum and plasma propagation problems.
4. To develop a fully working simulation code in MATLAB including periodic and perfect electric conductor (PEC) boundary conditions.
5. To present the results of several simulations using the abovementioned code.

6. To set the foundations for the future development of more advanced tools (including arbitrary geometries, non uniform meshes and PML boundaries) and for an in-deph analysis on the plasma propagation and absorption problem.

Regarding the proposed future work, many of the mentioned tools are already under development and presented in Chapter 8. This work is a preliminary study of the numerical method and programming tools that are intended to be further developed at a Master's Thesis at UC3M. Future work will also include a more detailed study of the results obtained in the simulations. Particularly, the Perfectly Matched Layer (PML) boundary conditions are thought to be specially advantageous for this task. The present thesis is, therefore, devoted to the development of numerical tools whilst the future work is planned to focus on the analysis and the physical interpretation of the results.

1.3 Project Budget

This section summarizes the main costs derived from the realization of the project. This financial plan is an estimate and does not represent real expenditure.

This thesis was partially founded by a Spanish Department of Education scholarship for the introduction to research of Bachelor and Master students '**Beca de colaboración en Departamentos 2017-2018**'. The terms of this scholarship established 3 daily hours workload during 8 months for the accomplishment of the aforementioned objectives.

Software costs¹ include the licenses for *Matlab R2018a*, the operating system *Microsoft Windows 10Pro* and the *Microsoft Office 365* package. Taking into account the noncommercial character of the present thesis, student licenses could be used. According to *Mathworks*² the *Matlab* yearly educational license cost is 250€. Office 365 University is sold for 70€ annually³. For *Microsoft Windows 10Pro*, the computation of the yearly price is more complicated because it is distributed with a perpetual license for 259€.

Considering a linear 10 year depreciation for this software, justified by its obsolescence due to the appearance of new operating systems, we can roughly estimate a 25€ annual cost⁴. Taking into account that the approximate duration of this project was 8 month, we can calculate the total software costs from the annual expenses:

$$Software_{cost} = \frac{8}{12}(Matlab_{cost} + Windows_{cost} + Office_{cost}) = 230€$$

Hardware costs basically comprise the depreciation of a 1200€ laptop over the thesis writing period. Considering 8 months and a linear depreciation until the 6th year, this item might account for 160€.

As described by the Spanish Department of Labor in the procedural resolution 'Convenio colectivo del sector de empresas de ingeniería y oficinas de estudios técnicos'⁵ the standard salary for a junior engineer is 17,544.24€ annually, which gives 9.75€ per hour. Due to the highly technical characteristics of this project, the author considers that the base salary should be increased to at least 12€/hour. About 500 hours were devoted to the project during an 8 month period (following the requirements of the awarded scholarship), hence, the total salary expenses would sum up to 6000€.

¹Notice that all these licenses may be issued under University agreements (no data available) being actually cheaper than the personal licenses hereby projected

²<https://es.mathworks.com/pricing-licensing>

³<https://www.microsoft.com/es-es/store>

⁴<http://www.depreciationguru.com/2016/02/computer-software-depreciation-calculation>

⁵<https://www.boe.es/boe/dias/2017/01/18/pdfs/BOE-A-2017-542.pdf>

Taking into account all the above expenses, the total cost of the project is estimated to be 6390€.

$$Project_{cost} = Software_{cost} + Hardware_{cost} + Labor_{cost} = 230€ + 160€ + 6000€ = 6390€$$

1.4 Socio-Economic and Regulatory Environment

According to the Space Report 2017 Overview [46] the global space industry grew 7.4% in 2017, up to \$383.5B. The industry has now been growing for more than a decade and the prospects are that it will continue to steeply grow in the near future. The 2016 market structure is shown in Figure 1.1. This growth might be explained by two factors. Firstly, the increase in the demand for space based services, mainly related to the telecommunication business. Secondly, the development of new disruptive technologies creating expectations for cheaper and more profitable access to space [20]. These technologies, like reusable launchers or cubeSat and nanoSat constellations, are changing the spaceflight business model and electric propulsion can be included among them.

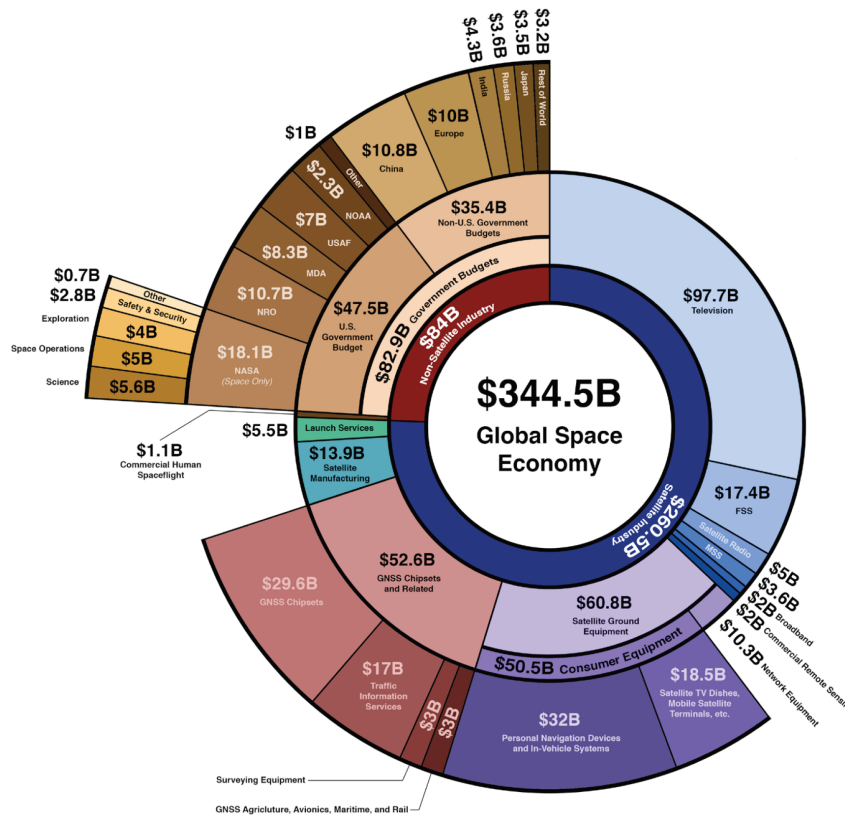


Figure 1.1: The global space economy at a glance (2016). Courtesy of Bryce Space and Technology [10]

Governmental expenditure accounts for about one quarter of the industry, the main actors being Europe, China and, by far the most important, the United States. Among US budget, less than one third is devoted to space research agencies (NASA), the rest corresponds to military and reconnaissance services (USAF and NRO) or other civil services (NOAA weather agency). This distribution is similar in other countries. Almost three quarters of the total space economy is driven by commercial operations. Virtually all commercial products and services are related to either navigation (Global Navigation Satellite Systems GNSS) or communications (Television and Fixed Satellite Service FSS). Commercial launch systems and satellite manufacturing account for about \$20B.

As a matter of fact, electric propulsion is the natural future choice to launch satellites providing commercial services. GNSS satellites are generally located at medium earth orbit (MEO) about

20000km above Earth's surface and FSS orbit around 35000km high in the geostationary orbit (GEO). A solution sought by many telecommunication companies is to launch their satellites to a low Earth orbit (LEO) or geosynchronous transfer orbit (GTO) and, then, elevate this orbit or perform orbital insertion using satellite built-in propulsion systems. Electric propulsion is the natural choice to carry out this task because it saves weight avoiding the use of heavy launch systems and upper stages. As the technology matures and the telecommunication industry continues to grow, it is expected that the demand for electric thrusters will accordingly expand.

Regarding the regulatory environment, the basic legal frame for space activities is the 1967 Outer Space Treaty. Due to the obvious international characteristics of spaceflight (spacecraft fly above the whole globe), international law is fundamental for space regulations. Consequently, there exist several international organizations managing access to space. For instance, the International Telecommunication Union (ITU) is in charge of coordinating orbits and frequencies for telecommunication satellites [10]. National law is also applicable to other space related fields like launches or R&D.

2 Electric Propulsion and State of the Art

2.1 Overview

In order to understand the specific details of electric propulsion, it is convenient to firstly inspect how thrust is generated in any rocket engine. **Newton's Second Law of Motion** is the foundation of mechanics. It provides the fundamental relation between motion and the forces applied on any particle s .

$$\frac{dP_s}{dt} = \frac{d(m_s \mathbf{v}_s)}{dt} = \Sigma \mathbf{F}_s \quad (2.1)$$

Additionally, **Newton's Third Law** states that, accompanying any force, an equal counterpart opposing it must appear. The combination of both laws leads to the **Principle of Conservation of Linear Momentum**. If Equation 2.1 were applied to a closed system of N particles, under forces satisfying the Third Law (which are all on classical mechanics, gravitational, electromagnetic...), the result would yield no change in the total momentum $\Sigma_N \dot{\mathbf{P}}_s = 0$.

This means that the only way of producing acceleration, besides the effect of external forces, is by accelerating part of the mass of the system and guiding it away with direction opposed to the desired change in velocity. This is the mechanism of thrust production in jet and rocket engines. Equation 2.1 may be split into the vehicle momentum (under the solid rigid assumption) and the exhaust particles momentum. Consequently, any change in the former, or thrust force \mathbf{F}_T , must equal the change in the later. Below \mathbf{u}_e is the effective exhaust velocity (equals the exhaust velocity only for a perfectly expanded jet).

$$\mathbf{F}_T = \dot{m} \mathbf{u}_e \quad (2.2)$$

It is assumed that the flow of exhaust particles has an uniform velocity in magnitude and direction. Lastly, external forces are included. These forces are, in general and for in-space propulsion, produced by gravitational interaction although other types can appear such as aerodynamic drag (at atmospheric flight or low orbits) and radiation pressure (significant for solar sail systems). Considering differential thrust vectoring (exhaust jet opposed to velocity at a first approximation)

$$\frac{dv}{dt} = \frac{F_T}{m} + \frac{\Sigma F_{\parallel}}{m} = \frac{1}{m} \frac{dm}{dt} u_e + \frac{\Sigma F_{\parallel}}{m} \quad (2.3)$$

Where F_{\parallel} is any other force acting along the velocity direction apart from the thrust, notice that the above equation is written for the velocity magnitude. Equation 2.3 can be integrated in time to find an expression relating the change in velocity to the ratio of initial to final masses. This is known as the Tsiolkovsky rocket equation

$$\Delta v = u_e \log \frac{m_0}{m_f} + \int_{t_0}^{t_f} \frac{\Sigma F_{\parallel}}{m} dt \quad (2.4)$$

The integral term in Equation 2.4 is typically very small for in-space propulsion where the gravitational force is always perpendicular to the orbit. However, it can be very significant during launch where, prior to the gravity turn, it is almost parallel to the velocity. Not to mention atmospheric drag which is, indeed always directed along the trajectory. Parallel forces can be included into the Δv **budget** of the mission. The other contribution to this mission figure, and the one normally targeted by electric propulsion, is the change of velocity needed for orbital maneuvers. Each mission has its own required Δv .

$$\Delta v_{tot} = \Delta v_{orb} - \int_{t_0}^{t_f} \frac{\Sigma F_{\parallel}}{m} dt = \Delta v_{orb} + \Delta v_{\parallel} \quad (2.5)$$

For a given mass ratio, the available Δv is proportional to the exhaust velocity. On the other hand, for a given mission, the mass ratio decreases exponentially with the exhaust velocity. More importantly, the payload ratio to total initial mass $p = m_p/m_0$ can be shown to follow

$$p = \frac{\exp\left(-\frac{\Delta v_{tot}}{u_e}\right) - \epsilon}{1 - \epsilon} \quad (2.6)$$

Where ϵ is the structural mass ratio i.e. the ratio of the vehicle's empty weight to the zero-payload and full-fuel weight. Here we consider a single stage spacecraft. The structural term only depends upon the technology used. Figure 2.1 shows the payload ratios for several structural mass ratios. As an example of a rather ambitious interplanetary mission, let's say from Earth's low orbit (LEO) to Mars orbit and return, we chose $\Delta v_{tot} = 10^4 m/s$ [27]. Note that this is a very rough approximation and depends on many factors like the choice of impulsive or low-thrust maneuvers, the type of transfer and the use of gravity assists which have not been included.

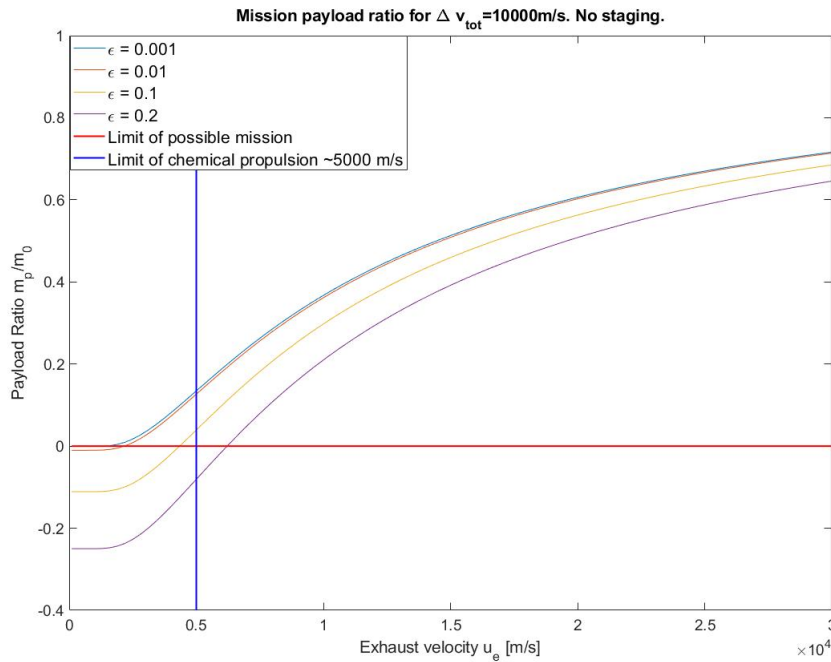


Figure 2.1: Payload ratio for a $\Delta v = 10^4 m/s$ mission with several structural mass ratios

A widely used figure of merit in propulsion is the **Specific Impulse** $I_{sp} = \frac{u_e}{g_0}$ measured in seconds. This is just a mean Earth's surface gravity acceleration normalized effective speed. The efficiency of propulsion systems is typically evaluated in terms of I_{sp} .

It becomes clear that specific impulses needed to accomplish the mission proposed in Figure 2.1 are not achievable with chemical propulsion besides for a really low structural mass ratio $\epsilon \approx 0.01$ (not reachable with current technology). Even with that ratio, the payload ratio is still quite small meaning super-heavy vehicles must be used to achieve a minimum useful payload. What is more, this mission starts at Earth's low orbit (LEO), as a consequence, the spacecraft should be assembled in orbit, probably implying that many launches would be necessary. As a consequence, staging is almost surely necessary for a mission of this kind, this increases complexity and costs.

In order to increase payload reducing the total mass and without need for staging it is evident

that we must move to the right of the plot. For the sake of reaching these extremely high exhaust velocities another acceleration mechanism is needed. The key factor is the deposition of energy into the propellant [1]. In chemical rocket engines, the energy in the bonds of molecules of the fuel and oxidizer is liberated in a very exothermic reaction. Accordingly, the product or propellant kinetic energy is limited by the chemical energy of those bonds.

On the other hand, electric propulsion systems apply power generated externally to produce either the heating of the propellant or electrostatic and electromagnetic forces accelerating the propellant particles. The decoupling of the power generation system (solar arrays, radioisotope thermoelectric generators or even future nuclear plants or microwave power receivers) from the propellant internal energy allows for a much greater energy deposition. The limit is now the available power and the physics governing the acceleration of the particles.

Propulsion System	Attainable I_{sp} [s]
Solid Fuel Booster	< 300
Liquid Fuel Engine	< 500
Nuclear thermal rocket	850 – 1000
Electrothermal thruster	< 1000
Electrostatic ion thruster	3000 – 20000
Electromagnetic thrusters	3000 – 12000

Table 3: Theoretical Specific Impulses for several types of propulsion systems [35]

From Table 3 ⁶ it is clear that electric propulsion (specially the last two types) is much more fuel efficient than any other current technology. Nonetheless, electric propulsion has limitations that make it non suitable for tasks besides in-space propulsion.

Electric thrusters usually produce a very little thrust (most often below 1N). This is not a problem when the system is working for a very long time as enormous Δv s are achievable. In other words, the mass flow rate in 2.2 is very small. This makes electric thrusters a good option for orbital maneuvering, station keeping and deep space missions (attainable with non impulsive propulsion).

On the other hand, whenever strong forces in the direction of the velocity vector in 2.3 appear, the small thrust may not be able to overcome those forces. As it was already stated, this is very significant during launch and inside the atmosphere. For those cases, the immense amount of thrust and power available with chemical engines is needed, despite the fact that this always means a less efficient use of the propellant.

Although there are no expectations that electric propulsion could substitute chemical rockets for launcher or lander technologies, increasing the thrust while maintaining the high Specific Impulse is a key objective to shorter mission times and propel larger vehicles. In this regard, there are two main concerns. Firstly, the scalability of the devices which depends almost completely upon the thruster technology used.

Secondly, and probably most importantly, is the energy efficiency of the system used. Because the power available is really limited by nowadays power plants (mostly solar arrays), mounting many thrusters together is not a solution unless they can convert most of the power delivered into useful thrust power. Therefore there is a second important figure of merit apart from the specific impulse. The thruster energy efficiency is defined as the ratio of the thrust power to the total power provided by the generation system [1]

$$\eta_T = \frac{F_T u_e}{2P_a} = \frac{F_T^2}{2\dot{m}P_a} \quad (2.7)$$

⁶The Highest efficiency ion thruster I_{sp} is based on Dual-stage Gridded Ion Thruster-DS4G which has not flown yet. Nuclear thermal rocket have not flown yet.

There are proposed and even tested technologies like magnetoplasmadynamic thrusters (MPDTs) which could deliver up to tens of Newtons but with a very large power consumption in the range of hundreds of kilowatts and up to megawatts. Largest space power systems in space today, such as the International Space Station (ISS) solar arrays, provide no more than $100kW$. Even with perfect efficiency, those systems will not be able to fly until powerful spacecraft power plants appear.

2.2 Types of Thrusters

The classification of plasma thrusters is usually done according to the mechanism of charge particle acceleration. It is important to notice that acceleration is not the only important process that takes place during the thruster operation. Indeed, ionization is always necessary because charged particles cannot be simply stored to be later accelerated. Instead, a gas has to be fed and ionized into the thruster ⁷. Additionally, recombination or diffusion to the walls should also be considered as losses of charged particles. Nevertheless, it is usual to look at the **fully ionized plasma momentum equation** to analyze different types of thrusters [1]

$$\nabla \cdot \rho \mathbf{u} \mathbf{u} = \epsilon_0 (\nabla \cdot \mathbf{E}) \mathbf{E} + \mathbf{j} \times \mathbf{B} - \nabla \cdot \bar{\bar{P}} \quad (2.8)$$

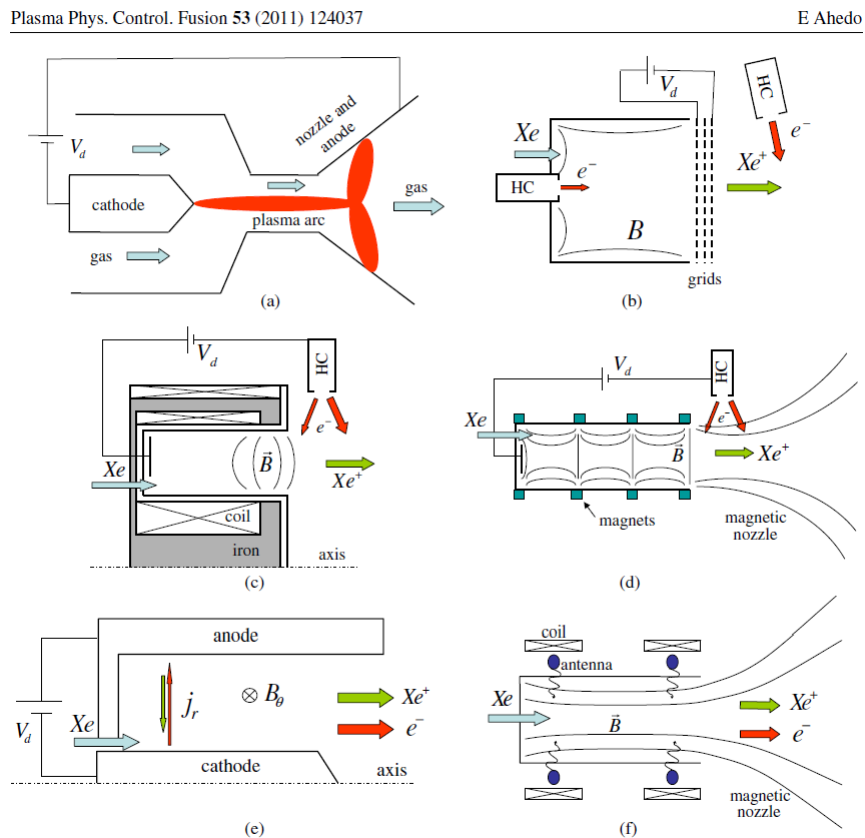


Figure 2.2: Several Plasma Thrusters. Schematic of working principle [1]

Where ρ is the mass density of the plasma, \mathbf{u} is the fluid velocity, ϵ_0 is the vacuum permittivity constant, \mathbf{j} is the current density and $\bar{\bar{P}}$ is the pressure tensor. The electromagnetic fields \mathbf{E} and \mathbf{B} are the sum of the fields applied externally and the ones generated by the plasma response currents.

⁷Pulsed plasma thrusters use the ablation or sublimation of solid fuel to produce charged particles

According to the different possible contributions to the plasma momentum in Equation 2.8 we can classify the thrusters that take advantage of each of those mechanisms

- **Electrothermal Thrusters:**

These devices work creating a pressure imbalance $\nabla \cdot \bar{\bar{P}}$ that produces an expansion accelerating the gas or plasma. The most representative electrothermal thruster is the Arcjet shown in Figure 2.2.(a) Pressure gradients are driven by the heating of the gas around a narrow hot plasma arc produced by the potential difference between a cathode and the downstream anode walls. The hot gas is subsequently expanded through a nozzle gaining axial momentum. This heating technique can be used to increase the specific impulse of chemical propulsion systems. However, the specific impulse is lower than for other devices ($< 1000s$) and electrode erosion is significant.

- **Electrostatic Thrusters. The ion gridded thruster:**

The next family of plasma thrusters accelerates ions by applying a strong electric field ($\nabla \cdot \rho \mathbf{u} \approx \epsilon_0 (\nabla \cdot \mathbf{E}) \mathbf{E}$) by means of a large electric potential difference between the cathode and a metallic grid located close to the exit of the chamber (See Figure 2.2.(b)). These thrusters are the most efficient technology flown today in terms of I_{sp} , with attainable expected values up to $20000s^8$. The main concern in gridded ion thrusters is the erosion caused by highly energized ions impacting on the grid surface and limiting the lifetime. Notice that a magnetic field may be applied inside the chamber to induce azimuthal electron velocity and enhance ionization. Nonetheless, this field does not produce axial acceleration and, consequently, does not contribute to thrust. Several IT modifications have been developed such as substitution of the internal hollow cathode by an RF microwave antenna for the gas ionization [31].

- **Electromagnetic Thrusters**

The last type of thrusters exploits the magnetic forces in Equation 2.8 ($\mathbf{j} \times \mathbf{B}$, either externally applied or induced) in addition to the usual electrostatics forces (both combining into a Lorentz Force). Electrodeless thrusters (explained in a later section) like the Helicon thruster shown in Figure 2.2.(f) fall under this category. The attainable specific impulse is slightly lower than the one expected for IT thrusters but still quite high compared to electrothermal and chemical propulsion. The physical phenomena governing the heating and acceleration in this devices is the most complicated of all three types. The Hall effect thruster (Figure 2.2.(c) and (d)) is a direct competitor of IT [1]. Its principle of operation relies on the inception of a voltage difference in a conductor, being this potential gradient (electric field) transverse to an applied current and a magnetic field perpendicular to the current (Hall effect). Lastly, Magnetoplasmadynamic (MPD) thrusters are devices that would ideally work at high power $> 100kW$ but could provide a very high thrust density. Their architecture is relatively simple (see Figure 2.2.(e)), a high voltage difference is imposed between the anode and the central cathode walls, an azimuthal magnetic field induces an axial force in the radially moving particles. Wall erosion and the availability of powerful enough in-space power-plants hinder the current implementation of this technology.

Although not mentioned above, there are some other technologies using electrical power to produce thrust. Notably, space tethers can be used for attitude control and Pulsed Plasma Thrusters (PPT) are a simple system suitable for small spacecraft.

2.3 State of the Art: Electrodeless Thrusters

Electrodeless thrusters are a proposed new generation of electric propulsion systems that heat up a plasma by electromagnetic radiation and accelerate the ionized particles in a magnetic nozzle. Ionization is enhanced by the heating of the plasma. Using this thrust generation mechanism, high

⁸Dual-stage 4-grid ion thruster concept[9]

specific impulse could be obtained without the need for a charged grid to accelerate ions and a neutralization electron beam because the propellant is exhausted as a quasi-neutral jet. The lack of emission cathode and grid prevents the erosion of electrodes making these devices more durable. Additionally, electrodeless thrusters are expected to be more easily scalable than current technologies which means that they could also be used for higher thrust applications, nowadays monopolized by Hall effect thrusters. Moreover, these systems are usually simpler to build and use less parts, for instance, the power processing unit (PPU) is cheaper than the high voltage devices used for ion gridded engines. One of the more significant advantages of Electrodeless thrusters is their ability to provide a large thrust density as opposed to conventional thruster where grid screening or the Hall parameter limit the maximum attainable value [27].

Among the more promising technologies under development, we can find **Helicon** thrusters [2] or the **VASIMR** rocket concept [19], the main difference being the mechanism of energy deposition and heating of the plasma. Instead of working in the high radiofrequency range, **Electron Cyclotron Resonance** thrusters use microwaves to heat up the plasma and produce ionization.

2.3.1 ECR Thrusters

Electron Cyclotron Resonance (ECR) has been used to ionize and heat plasma for a wide range of applications mainly since the second half of the 20th century. Some relevant technologies exploiting this phenomenon are ECR ion sources (ECRIS) employed in solid state physics research and the semiconductor industry (plasma etching) or the research in ECR applicability for nuclear fusion [37].

The ECR thruster basic assemble comprises a chamber where the gas-plasma mixture is heated by absorption of electromagnetic waves. A noble gas, generally Argon or Xenon is fed into the chamber through a gas injector. Alternatively, and contrary to traditional thrusters, it is expected that ECR thrusters will be able to work with other gases [37]. Especially interesting is the utilization of Nitrogen for airbreathing electric propulsion.

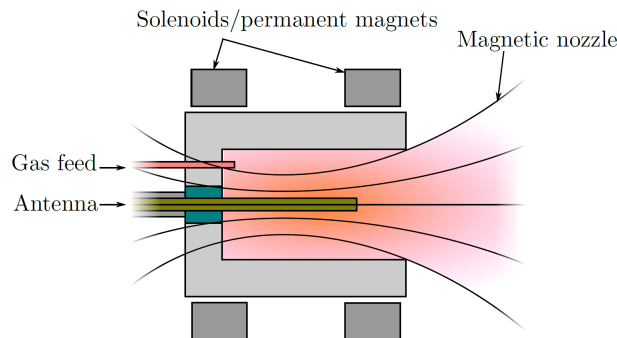


Figure 2.3: Schematic of the ECR prototype built by ONERA

Ionization takes place due to the heating of the plasma and the increase in the collision rate of charged particles. There are different setups for the positioning of the antennas and the applied magnetic field topology inside the thruster. The objective is to generate wave propagation in a certain direction and with a certain excitation frequency depending on the static magnetic field. We will see that wave resonance can occur when the parameters are tuned in a particular configuration. Resonance is linked to high energy deposition in the plasma i.e. the objective of the electromagnetic bombardment.

Downstream, the charged particles are accelerated by solenoids and magnets forming a magnetic nozzle (they can be the same ones used inside chamber). The magnetic field topology can also be used to steer the plasma jet and provide thrust vector control[36]. The magnetic field is also essential for the internal domain as it is one of the factors determining the wave propagation and absorption.

It creates the suitable conditions for resonance and maintains the charge particles away from the chamber walls preventing excessive diffusion losses.

Preliminary studies and prototypes of ECR thrusters, first appeared in the 1960s, such as the works by Miller[38] and Sercel [43], predicted an attainable specific impulse on the order of $\sim 3000s$ with $\sim 40\%$ thrust efficiency. Notably, a low power small prototype of about 30mm diameter was built by ONERA [28]. This thruster, shown in Figure 2.3 changed the conventional setup with axial waveguides by utilizing a coaxial dipole antenna. The model showed very high thrust efficiency not expected for such a low power range $\sim 100W$. A careful study of the magnetic nozzle topology and plasma diagnostic were proposed as future work for the attainment of larger and more efficient thrusters.

2.3.2 ECRA and the MINOTOR Project

The MINOTOR project (Magnetic NOzzle thruster with elecTron cyclOtron Resonance), was selected by the European Commission during the H2020 call for emerging technologies of electric propulsion. Coordinated by ONERA, the consortium institutions are:

- ONERA (France)
- Universidad Carlos III de Madrid (Spain)
- Thales Microelectronics (France)
- Justus-Liebig-Universitaet Giessen (Germany)
- Thales Alenia Space Belgium (Belgium)
- SAFRAN Aircraft Engines (France)
- LUP (France)

The Electron Cyclotron Resonance Accelerator (ECRA) is proposed as a new griddless and cathodeless thruster with thrust vectoring. This system will utilize ECR as the ionization and acceleration process together with a magnetic nozzle. MINOTOR aims at better defining the capabilities of this new technology and bringing it to TLR 4/5. As defined by the European Commission, this Technology Readiness Level means that the technology has been validated first in lab and later in a relevant environment.

Despite the expectations of improved reliability, cost and performance when compared to mature technologies; there are many challenges, specially, those concerned with not fully understood physical phenomena which is hindering the development of the technology. Therefore, a complete mathematical and numerical model and extensive testing are needed to step forward.

The contribution of EP2 team at UC3M is “to establish a complete mathematical model of the thruster, and develop a numerical simulation code composed of four interlinked modules: plasma-wave interaction, ion and neutral code, electron code, and magnetic nozzle code” [21].

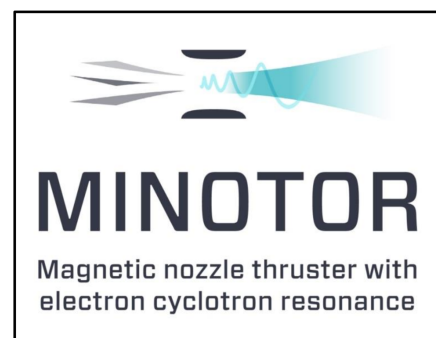


Figure 2.4: MINOTOR Logo

2.4 State of the Art: Numerical methods for the wave-plasma interaction problem

The behavior of electromagnetic waves traveling through a plasma is complex and not fully understood besides for easy problems with simple geometry. When designing a thruster, a wide range of phenomena should be studied. Firstly, electromagnetic waves should be able to arrive from the antennas to the region where ionization is sought, a problem known as accessibility. Then, there must be a net energy transfer from the wave to the plasma in order to heat it up. Throughout the whole process, reflection, cutoff, resonances and wave mode conversion can occur [37]. The above-mentioned phenomena are fundamentally controlled by plasma parameters, electromagnetic wave emission, the topology of the background magnetic field and the domain's geometry and boundary conditions. Moreover, there is a strong coupling with the kinetics of the plasma, in particular the electrons. Wave propagation affects the plasma parameters due to the absorption of electromagnetic energy and, conversely, the plasma parameters affect wave propagation. Consequently, we are facing a coupled problem that is no longer linear. Notice that electromagnetic propagation in a uniform stationary cold plasma is linear. Even the linear propagation problem is too complex to be tractable analytically. Numerical methods are unavoidable to characterize the fields and plasma parameters inside a thruster.

Ray tracing methods have been used to study propagation and accessibility [12], however, this approach is only accurate when the wavelengths are significantly shorter than the gradients in plasma properties (WKB approximation) [37]. This condition is not satisfied in ECR thrusters (specially near resonances), as a consequence, Maxwell's equations should be solved in all the domain without possible simplification.

Historically, the prevailing method for electromagnetic propagation modeling and simulation was the **Finite Difference Time Domain (FDTD)**. This explicit method was first proposed for vacuum by Yee[47] (also known as Yee method) in 1966. It is advantageous in vacuum due to its consistency, lack of spurious solutions and the ease to implement simple boundary conditions. Being explicit, it also does not use as much computer memory as comparable implicit methods for large problems [45]. Arguably, FDTD is not the most suitable method for the study of plasma propagation. The original vacuum method is only valid for isotropic media, accordingly, modifications are mandatory for magnetized plasma simulation. Stability of time domain methods requires the time step-size to be proportional to the spatial node distance (Courant Stability Condition [8]). Near the plasma resonances there might be waves with a very short wavelength, therefore, the required mesh needs to be very fine to resolve them. This affects the time step as well, at the end the number of iterations to assure stability increases non-linearly with the wavelength (the exact relation depends on the problem dimensions). There have been successful simulations of magnetoplasma wave propagation using exotic FDTD variants that overcome the stability issue, such as the Exponential Time Differencing (FDTD ETD) technique [25] or the Symplectic Finite Difference Time Domain (SFDTD) [42] method, however, these methods are too computationally demanding to be applied to a full thruster model with inhomogeneous plasma.

Although it is not the best option to study transients (inverse Fourier transforms and a laborious process is needed), **Finite Difference Frequency Domain** methods can be powerful tools for the simulation of the thruster steady state operation. Computationally, these methods are lighter than FDTD because the field is solved once and then analytically propagated with time. On the other hand, the basic method is implicit which implies a high memory usage (see Chapter 6 for an analysis of the performance). This method was used to obtain the results presented in this thesis.

Lastly, **Finite Elements (FEM)** methods for electromagnetic propagation appeared to supersede FDTD for some applications⁹. This family of methods is capable of modeling complex geometries. As a drawback, they are complex and difficult to implement and require great computer power and memory to solve large systems of linear equations. These methods can also be frequency domain [41].

⁹It took some effort to arrive to vector elements, which are needed to simulate correctly the wave problem.

3 Electromagnetic Waves in Plasma

The mechanism of heating and ionization in the Electron Cyclotron Resonance Accelerator (ECRA) relies on the interaction of microwaves in plasma. Before using numerical methods to address this complicated physical phenomenon, fundamental considerations can arise from the study of a simplified analytic electromagnetic model.

Moreover, some of the concepts presented in the next section are key to the understanding of electromagnetism and unavoidable to be explored if a deep knowledge on the principles of this technology is sought.

3.1 Basic Electromagnetic Theory

3.1.1 Maxwell's Equations

The complete set of equations describing all non relativistic electromagnetic phenomena are:

$$\nabla \cdot \mathbf{E} = \frac{\rho}{\epsilon_0}, \quad (3.1)$$

$$\nabla \times \mathbf{E} = -\frac{\partial \mathbf{B}}{\partial t}, \quad (3.2)$$

$$\nabla \cdot \mathbf{B} = 0, \quad (3.3)$$

$$c^2 \nabla \times \mathbf{B} = \frac{\mathbf{j}}{\epsilon_0} + \frac{\partial \mathbf{E}}{\partial t}. \quad (3.4)$$

Where \mathbf{E} is the electric field vector and \mathbf{B} is the magnetic flux density vector (normally referred as magnetic induction), we will simply call this term magnetic field.¹⁰ The constant vacuum electric permittivity and magnetic permeability (used later) are ϵ_0 and μ_0 , c is the speed of light in vacuum. The spatial electric charge density is denoted by ρ and \mathbf{j} stands for the electric current density vector.

Equation 3.2 is the Faraday's Law of Induction. Equation 3.3 establishes the nonexistence of magnetic monopole sources. Equation 3.4 is the Ampère's Circuital Law with the addition of the so-called Displacement Current due to J.C.Maxwell [26]. The combination of Equations 3.1 and 3.4 leads to the Law of Charge Conservation:

$$\frac{\partial \rho}{\partial t} + \nabla \cdot \mathbf{j} = 0 \quad (3.5)$$

After taking the curl of 3.2, substituting into 3.4 and recalling that $c^2 = \frac{1}{\epsilon_0 \mu_0}$; the **wave equation** for the electric field is obtained

$$\nabla \times (\nabla \times \mathbf{E}) + \frac{1}{c^2} \frac{\partial \mathbf{E}}{\partial t} = -\mu_0 \frac{\partial \mathbf{j}}{\partial t} \quad (3.6)$$

This is a hyperbolic partial differential equation. The time derivatives disappear if a current density and an electric field in terms of a complex exponential are imposed, the real part representing the

¹⁰Strictly, this is the \mathbf{H} vector field proportional to \mathbf{B} in vacuum. For the phenomena studied in this thesis both can be used indistinctly with a minor change in the equations.

actual field and current density. The time-harmonic field and current density vectors for a monochromatic¹¹ wave with a given excitation angular frequency ω are

$$\mathbf{E}(\mathbf{r}, t) = \Re[\hat{\mathbf{E}}(\mathbf{r}, \omega) \exp(-i\omega t)]; \quad \mathbf{j}(\mathbf{r}, t) = \Re[\hat{\mathbf{j}}(\mathbf{r}, \omega) \exp(-i\omega t)] \quad (3.7)$$

Note that the terms $\hat{\mathbf{E}}$ and $\hat{\mathbf{j}}$ multiplying the exponential factors are complex amplitudes containing information both about the magnitude and phase of the varying field. If the vacuum wave equation is sought, it is possible to only consider externally applied currents $\hat{\mathbf{j}}_a$ ('a' stands for antenna) and neglect any contribution due to induced current density in the overall $\hat{\mathbf{j}}$ term. This is the case not only for vacuum but also for isotropic dielectric media where there are not free charges producing current or any material polarization. The vacuum frequency domain wave equation finally reads

$$\nabla \times \nabla \times \hat{\mathbf{E}} = -\nabla^2 \hat{\mathbf{E}} + \nabla(\nabla \cdot \hat{\mathbf{E}}) = \frac{\omega^2}{c^2} \hat{\mathbf{E}} + i\omega\mu_0 \hat{\mathbf{j}}_a \quad (3.8)$$

Additionally, Equation 3.8 for vacuum propagation can be modified to account for the response field created by the charge redistribution current inside plasma media. The introduction of a conveniently modeled dielectric tensor multiplying the right hand side field vector in 3.8 provides a representation of any linear anisotropic medium including a magnetized cold plasma [44]. A linear material is any medium producing a polarization response field proportional to the exterior field.

$$\nabla \times (\nabla \times \hat{\mathbf{E}}) = -\nabla^2 \hat{\mathbf{E}} + \nabla(\nabla \cdot \hat{\mathbf{E}}) = \frac{\omega^2}{c^2} \bar{\bar{\mathbf{k}}} \cdot \hat{\mathbf{E}} + i\omega\mu_0 \hat{\mathbf{j}}_a \quad (3.9)$$

It is easy to realize that the vacuum equation is recovered by setting the dielectric tensor to the identity matrix. The plasma dielectric tensor will be derived in a later section. Equation 3.9 will be expanded into finite difference schemes and the arising linear system of equations will be solved to find $\hat{\mathbf{E}}$ at every point in space.

The field can be expressed in complex exponential form, not only in time but in space as well for certain cases, particularly, this approach is valid in an homogeneous and infinite linear medium¹². By virtue of linearity, the solution to a full electromagnetic propagation problem with different excitation frequencies is the superposition of many terms of the form 3.10. Fourier analysis may be used to decompose a time function (for instance the current density) into its frequency analogs.

$$\mathbf{E}(\mathbf{r}, t) = \Re[\hat{\mathbf{E}}(\mathbf{r}, \omega) \exp(-i\omega t)] = \Re[\tilde{\mathbf{E}}(\mathbf{k}, \omega) \exp(-i\omega t + i\mathbf{k} \cdot \mathbf{r})] \quad (3.10)$$

Where $\tilde{\mathbf{E}}$ is the complex amplitude for the time and space-harmonic electric field. It is easy to observe the completeness of this approach and its ability to represent any harmonic wave. The phase and magnitude information is compactly contained in the complex amplitude multiplying the exponential. The excitation frequency ω and the spatial frequency or wavenumber vector \mathbf{k} (which provides the direction of propagation) are factors in the exponential. Finally, as it will be shown later, the speed of the wavefront can be derived from the ratio of the spatial and excitation frequencies.

The exponential form of the propagated field permits the attainment of analytic solutions for problems with simple boundary conditions and forcing terms. This feature will be exploit later as a means of verification for the numerical method used.

¹¹Monochromatic is the correct term for vacuum where, for a certain excitation frequency, 2 polarizations with the same wavelength appear. In the most general case, with different wavelengths, mono-frequency would be more accurate.

¹²The specific condition is that the spatial eigenfunctions should have exponential form.

3.1.2 The Dispersion Relation

Let's now explore 3.9 under the wave described by 3.10 and a forcing term of the same form. We would like to simplify the term $\nabla \times \tilde{\mathbf{E}}$ in Equation 3.9. The curl term can be expanded, after which we obtain

$$\nabla \times (\nabla \times \tilde{\mathbf{E}}) = -\exp(i\mathbf{k} \cdot \mathbf{r})\mathbf{k} \times (\mathbf{k} \times \tilde{\mathbf{E}}) \quad (3.11)$$

After substitution into the wave equation 3.9, the exponential term cancels out on both sides of the equality eliminating any position dependence from the expression. In a similar manner was the time dependence canceled out in equation 3.6

$$\mathbf{k} \times (\mathbf{k} \times \tilde{\mathbf{E}}) + \frac{\omega^2}{c^2} \tilde{\mathbf{E}} = -i\omega\mu_0\tilde{\mathbf{j}}_a \quad (3.12)$$

For the sake of studying the propagation of electromagnetic waves through a medium, it is useful to solve the unforced system, disregarding the forcing term in the right hand side of 3.12. Writing the equation in Cartesian coordinates and matrix form

$$\left[\begin{pmatrix} -k_y^2 - k_z^2 & k_x k_y & k_x k_z \\ k_x k_y & -k_x^2 - k_z^2 & k_y k_z \\ k_x k_z & k_y k_z & -k_x^2 - k_y^2 \end{pmatrix} + \frac{\omega^2}{c^2} \begin{pmatrix} \kappa_{xx} & \kappa_{xy} & \kappa_{xz} \\ \kappa_{yx} & \kappa_{yy} & \kappa_{yz} \\ \kappa_{zx} & \kappa_{zy} & \kappa_{zz} \end{pmatrix} \right] \begin{pmatrix} \tilde{E}_x \\ \tilde{E}_y \\ \tilde{E}_z \end{pmatrix} = \begin{pmatrix} 0 \\ 0 \\ 0 \end{pmatrix} \quad (3.13)$$

For the system described by 3.13 to have a non-trivial solution, the determinant of the coefficient matrix must be null. For instance, taking the vacuum dielectric tensor (identity matrix) the solution is

$$k_x^2 + k_y^2 + k_z^2 = |\mathbf{k}|^2 = \frac{\omega^2}{c^2} \quad (3.14)$$

Inspection of Equation 3.10 provides physical insight into the significance of the **Dispersion Relation** 3.14. Taking an arbitrary point in space at $t = t_0$ it is easy to notice that the value of the field will be repeated at $t = t_1$ at a distance $x = \pm c(t_1 - t_0)$ and in the direction of the propagation or wavenumber vector \mathbf{k} . Therefore, the speed of an electromagnetic wavefront traveling through vacuum is equal to the speed of light c . This is called **Phase Velocity** and depends on the medium as modeled by the dielectric tensor. There are quite interesting phenomena explained by Equation 3.13, for example, waves with different frequencies travel at different speeds and directions in certain media, this effect is called Dispersion.

Equation 3.14 shows the **natural modes** of propagation of electromagnetic waves through vacuum. In the parametric space of wavenumbers (with k_x, k_y, k_z in Cartesian axes) the solution is a sphere with radius ω/c . It can be shown that electromagnetic modes always appear as pairs of solution surfaces. The particular vacuum propagation dispersion relation has a double root corresponding to the abovementioned sphere. Moreover, a third mode can always appear in which $\mathbf{k} = 0$ and $\omega = 0$, this corresponds to an electrostatic field with zero space and time derivatives in 3.6.

3.2 Waves in a cold plasma

3.2.1 Plasma dielectric tensor

It is not feasible to describe and trace the motion and interactions of each of the enormous number of particles contained within a small volume of plasma. Moreover, the absorption and propagation of electromagnetic waves in plasma media is closely related to that motion due to charge redistribution. Therefore, a simplified and mathematically tractable model is sought. This model should be able to retain the characteristic behaviour of a plasma while been based on reasonable assumptions.

The main simplification will be that electrons and ions have not net motion in the unperturbed state. In other words, plasma temperature, and as a consequence thermal motion, is completely neglected. Quasi-neutrality (neutrality beyond the Debye sphere) of the electron-ion mixture is also imposed. Finally, though the numerical simulations may include slowly changing spatial properties, the plasma is assumed locally homogeneous.

This cold plasma model comprises much of the literature on plasma waves. Plasma modes of motion have been successfully studied and commonly recognized types of plasma waves (Alfvén, Langmuir-Tonks, cyclotron...) arise naturally when the abovementioned simplifications are introduced [44].

It will be shown that, under these assumptions, a cold plasma can be modeled as a linear material i.e. a dielectric plasma tensor can be introduced into the Maxwell's equations accounting for the motion of the charged particles. The objective of this section is to find that tensor as a function of the plasma properties at each point of space.

Furthermore, it is possible to model the effect of a background, externally applied and uniform magnetic field just by changing the tensor. The orientation of the magnetic field is important as it leads to the spatial anisotropy of the medium giving rise to different behavior in terms of wave velocity and absorption and depending on the propagation direction.

Previously, the dielectric tensor was introduced to go from the vacuum wave equation in frequency domain 3.8 to 3.9 without further explanation. Let's now follow the steps to obtain the tensor. In a generic medium, after Fourier analysis in space and time

$$\mathbf{k} \times (\mathbf{k} \times \mathbf{E}) + \frac{\omega^2}{c^2} \mathbf{E} = -i\omega\mu_0(\mathbf{j}_a + \mathbf{j}_c) \quad (3.15)$$

For the sake of convenience the tildes have been removed from the complex amplitude field and current . Note, however, that all first order quantities are expanded by the usual exponential term both in space and time $f(\mathbf{r}, t) = g(\mathbf{k}, \omega) \exp(-i\omega t + \mathbf{k} \cdot \mathbf{r})$. This includes electric field, current densities and particle velocities whilst, from this point on, the number densities and background field will be considered zeroth order when they appear (undoubtedly the charge of individual plasma species and their masses are also constants).

Notice also that, above, the current has been split into two contributions. The first one is the usual source current \mathbf{j}_a . It is a current applied externally for example by a wire or antenna. The second one \mathbf{j}_p is the current due the movement of charge particles within the plasma. In a dielectric medium there is also a polarization current which is normally expressed as the rate of change of the polarization density vector field [23] \mathbf{P} . This definition is not equally valid for plasma so it may lead to confusion. Plasma is neither a dielectric nor a perfect conductor although it contains free charged particles.

According to Ohm's law for linear materials, the plasma current can be related to the applied electric field using a conductivity tensor

$$\mathbf{j}_p = \bar{\sigma} \cdot \mathbf{E} \quad (3.16)$$

At this point, it is helpful to introduce the concept of electric displacement field including the vacuum displacement (2nd term in left hand side of 3.15) and the plasma current

$$\mathbf{D} = \epsilon_0 \mathbf{E} + \frac{i}{\omega} \mathbf{j}_c = \epsilon_0 \left(\bar{\mathbf{1}} + \frac{i}{\omega \epsilon_0} \bar{\boldsymbol{\sigma}} \right) \cdot \mathbf{E} = \epsilon_0 \bar{\boldsymbol{\kappa}} \cdot \mathbf{E} \quad (3.17)$$

$$\bar{\boldsymbol{\kappa}} = \bar{\mathbf{1}} + \frac{i}{\omega \epsilon_0} \bar{\boldsymbol{\sigma}} \quad (3.18)$$

Substituting the equality for $\bar{\boldsymbol{\kappa}}$ from 3.18 into Equation 3.9 one would recover 3.15 showing that the inclusion of the dielectric tensor is a suitable means of modeling the plasma current as long as it obeys Ohm's Law. The total current is the sum of the current of each species. As a result, the conductivity tensor of the plasma is obtained adding the conductivities of the ions and electrons within it. The susceptibility is defined as the contribution of each species to the dielectric tensor, its relation to the conductivity tensor is easily noticed

$$\bar{\boldsymbol{\kappa}}(\omega) = \bar{\mathbf{1}} + \sum_s \bar{\chi}_s(\omega) = \bar{\mathbf{1}} + \sum_s \frac{i}{\omega \epsilon_0} \bar{\boldsymbol{\sigma}}_s \quad (3.19)$$

The current of each species s can be studied separately to find the corresponding susceptibility. The charge density is the charge times the number density of the particle n_s , therefore the flux through a cross section of unit area or simply current density is

$$\mathbf{j}_s = n_s q_s \mathbf{v}_s \quad (3.20)$$

Where q_s is the electric charge of a single particle of the type s and v_s is its velocity. From Ohm's Law 3.16 and the definition of susceptibility

$$\mathbf{j}_s = -i\omega \bar{\chi}_s \cdot \mathbf{E} = n_s q_s \mathbf{v}_s \quad (3.21)$$

Clearly, the next step is to look at the dynamics of charged particles to relate the velocity to the electromagnetic fields. Neglecting thermal motion, Newton's Second Law for a particle subjected to a Lorenz force reads

$$m_s \frac{d\mathbf{v}_s}{dt} = q_s (\mathbf{E} + \mathbf{v}_s \times \mathbf{B}) - m_s \nu_m \mathbf{v}_s \quad (3.22)$$

The last term includes the effective momentum loss due to charged particles' collisions (Coulomb collisions). After Fourier analysis in the first order quantities

$$-i\mathbf{v}_s(\omega + i\nu_m) = \frac{q_s}{m_s} (\mathbf{E} + \mathbf{v}_s \times \mathbf{B}_0) \quad (3.23)$$

The nomenclature has not been changed to keep a simple equation formulation, however, notice that all the Fourier expanded quantities should be written as $v_s \rightarrow \tilde{v}_s$. Note also that the magnetic field appearing in 3.23 is externally applied. The wave induced magnetic field is much weaker than the electric field and is usually neglected. Choosing an appropriate reference frame can greatly simplify the task of solving for the susceptibility tensor. Firstly, let's take the magnetic field directed along z-direction in Cartesian coordinates $\mathbf{B}_0 = B_0 \mathbf{1}_z$.

For convenience we chose a reference frame with the propagation vector in the x-z-plane, recalling that $\mathbf{1}_z$ is defined by the direction of the applied magnetic field, the unit vectors in the two other directions are

$$\mathbf{1}_y = \frac{\mathbf{k} \times \mathbf{1}_z}{\|\mathbf{k} \times \mathbf{1}_z\|} \quad \mathbf{1}_x = \mathbf{1}_y \times \mathbf{1}_z \quad (3.24)$$

It will be shown that the use of a complex basis allows the dielectric matrix to be written in diagonal form, thus, uncoupling the equations. The change of basis yields

$$v^\pm = \frac{1}{2}(v_x \pm iv_y) \quad E^\pm = \frac{1}{2}(E_x \pm iE_y) \quad (3.25)$$

One may substitute into 3.23 to find that the following solution satisfies the system arising from the vector equation. Note that the z components are decoupled

$$v_s^\pm = \frac{iq_s}{m_s} \frac{E^\pm}{\omega + i\nu_m \mp \Omega_s} \quad (3.26)$$

$$v_{zs} = \frac{iq_s}{m_s} \frac{E_z}{\omega + i\nu_m} \quad (3.27)$$

The algebraic cyclotron frequency of a particle of type s is

$$\Omega_s = \omega_{cs} = \frac{q_s B_0}{m_s} \quad (3.28)$$

It is important to notice that Ω_s changes sign with q_s and B_0 . Moreover the plasma frequency is defined as

$$\omega_{ps}^2 = \frac{n_s q_s^2}{m_s \epsilon_0} \quad (3.29)$$

Now, solving for the susceptibility components according to equation 3.21

$$\chi_s^\pm = -\frac{\omega_{ps}^2}{\omega(\omega + i\nu_m \mp \Omega_s)} \quad (3.30)$$

$$\chi_{zs} = -\frac{\omega_{ps}^2}{\omega^2} \quad (3.31)$$

The original basis can be recovered to go back from this diagonal form to the tensor in Cartesian coordinates yielding

$$\chi_{xx} = \chi_{yy} = \frac{\chi^+ + \chi^-}{2} \quad (3.32)$$

$$\chi_{xy} = -\chi_{yx} = \frac{i(\chi^+ - \chi^-)}{2} \quad (3.33)$$

The following notation after Stix [44] will be useful later as it provides valuable information regarding polarization and phase relations once the dispersion relation is obtained

$$R \equiv 1 + \sum_s \chi_s^- = 1 - \sum_s \frac{\omega_{ps}^2}{\omega(\omega + i\nu_m + \Omega_s)} \quad (3.34)$$

$$L \equiv 1 + \sum_s \chi_s^+ = 1 - \sum_s \frac{\omega_{ps}^2}{\omega(\omega + i\nu_m - \Omega_s)} \quad (3.35)$$

$$S \equiv \frac{1}{2}(R + L) \quad (3.36)$$

$$D \equiv \frac{1}{2}(R - L) \quad (3.37)$$

$$P \equiv 1 - \sum_s \frac{\omega_{ps}^2}{\omega(\omega + i\nu_m)} \quad (3.38)$$

Where S stands for sum, D for difference and P for plasma. Direct substitution into the expressions for the susceptibility components leads to the cold plasma dielectric tensor as defined by 3.19

$$\bar{\kappa} \cdot \mathbf{E} = \begin{pmatrix} S & -iD & 0 \\ iD & S & 0 \\ 0 & 0 & P \end{pmatrix} \begin{pmatrix} E_x \\ E_y \\ E_z \end{pmatrix} \quad (3.39)$$

The dispersion relation is obtained plugging back the dielectric tensor into the homogeneous wave equation 3.12. For simplicity the change of variable $\mathbf{n} = \mathbf{k}c/\omega$ is applied.

$$\mathbf{n} \times (\mathbf{n} \times \mathbf{E}) + \bar{\kappa} \cdot \mathbf{E} = 0 \quad (3.40)$$

It is useful to define the angle between the propagation vector and the static magnetic field

$$\theta = \cos^{-1} \left(\frac{\mathbf{1}_z \cdot \mathbf{n}}{\|\mathbf{n}\|} \right) \quad (3.41)$$

Note that the magnitude n is the refractive index. The homogeneous plasma wave equation is shown below. The dispersion relation arises from the determinant of the matrix in 3.42.

$$\begin{pmatrix} S - n^2 \cos^2 \theta & -iD & n^2 \cos \theta \sin \theta \\ iD & S - n^2 & 0 \\ n^2 \cos \theta \sin \theta & 0 & P - n^2 \sin^2 \theta \end{pmatrix} \begin{pmatrix} E_x \\ E_y \\ E_z \end{pmatrix} = \begin{pmatrix} 0 \\ 0 \\ 0 \end{pmatrix} \quad (3.42)$$

3.2.2 Wave Phase and Polarization

Polarization refers to the orientation of the electric field vector. For instance, for a wave propagating through vacuum, the electric and magnetic fields are always transverse to the propagation direction and perpendicular one to the other. However, the orientation in the transverse plane can remain constant (linear polarization) or change with time (circular and elliptical polarization). A wave would have circular polarization if the tip of the electric field vector describes a circumference in the perpendicular plane (a spiral trajectory in 3D space). Then, for a wave propagating in the magnetic field direction $\mathbf{1}_z$, circular polarization in terms of the real field (time domain not frequency domain) occurs when

$$E_x^{real} = a \cos(-\omega t) \qquad E_y^{real} = a \sin(-\omega t) \qquad (3.43)$$

This condition expressed in complex amplitudes gives $i\tilde{E}_x/\tilde{E}_y = 1$ for a positively rotating field with respect to the magnetic field and with positive ω , namely right-hand circular polarization. Conversely $i\tilde{E}_x/\tilde{E}_y = -1$ gives a left-hand circular polarization. Looking at the second row of equation 3.42

$$\frac{i\tilde{E}_x}{\tilde{E}_y} = \frac{n^2 - S}{D} \qquad (3.44)$$

Equation 3.36 together with 3.44 implies that right-hand circular polarization corresponds to $n^2 = R$ and left-hand circular polarization to $n^2 = L$ with $\theta = 0$. Polarization is an important parameter for reflection, absorption and mode conversion of plasma waves.

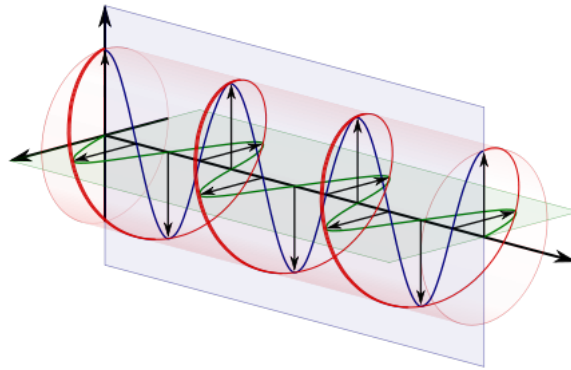


Figure 3.1: Circular Polarization with respect to the propagation direction [4]

3.2.3 Wave normal surfaces, cutoff and resonance and the CMA diagram

There exists a helpful tool to characterize the different waves that may propagate on plasma. The locus of the tip of a vector having the direction of wave propagation and the magnitude of the phase vector is called **wave normal surface** [44]. That vector is completely defined by $1/n$ and θ in 3.42 for a given static magnetic field vector. Accordingly, wave normal surfaces represent solutions of the dispersion relation, hence being straightforward representations of the modes of propagation.

The main advantage of this approach relies on the fact that the topology of normal surfaces is constant across regions of the parametric space of plasma properties. Therefore, the propagation of electromagnetic waves in a cold plasma can be classified in well defined bounded regimes. As it was mentioned when studying propagation in vacuum, the modes, and thus the normal surfaces, appear always in pairs. Unlike through vacuum, the wave surfaces in plasma are generally not coincident.

The plasma dispersion relation was independently found in works by E.O. Åström [6] and W.P. Allis [3]. A widespread form of the equation arising after taking the determinant is

$$An^4 - Bn^2 + C = 0, \quad (3.45)$$

$$A = S \sin^2 \theta + P \cos^2 \theta, \quad (3.46)$$

$$B = RL \sin^2 \theta + PS(1 + \cos^2 \theta), \quad (3.47)$$

$$C = PLR \quad (3.48)$$

In a later section, *wave-explorer* software will be used to numerically solve for wave normal surfaces, however, some simple cases can be readily checked. For example, let's take propagation parallel to the static magnetic field $\theta = 0$

$$A = P, \quad (3.49)$$

$$B = 2PS = P(R + L), \quad (3.50)$$

$$P(n^4 - (R + L)n^2 + RL) = 0 \quad (3.51)$$

The roots of this equation, or natural modes, are $n^2 = R$ and $n^2 = L$ which, of course, correspond to the circular polarizations. There is yet another solution valid for any n , hence, also when $n \rightarrow \infty$, this is the plasma resonance $P=0$.

Two phenomena occur when the values in the parametric space of plasma properties produce a zero or pole in the dispersion relation for n . Whenever $n \rightarrow 0$ the wave decays until evanescence. Whilst when $n \rightarrow \infty$ there is an infinite growth in the wave spatial frequency, thus, resonance. Inspection of 3.45 shows that Cutoff occurs either when $P = 0$ or $L = 0$ or $R = 0$.

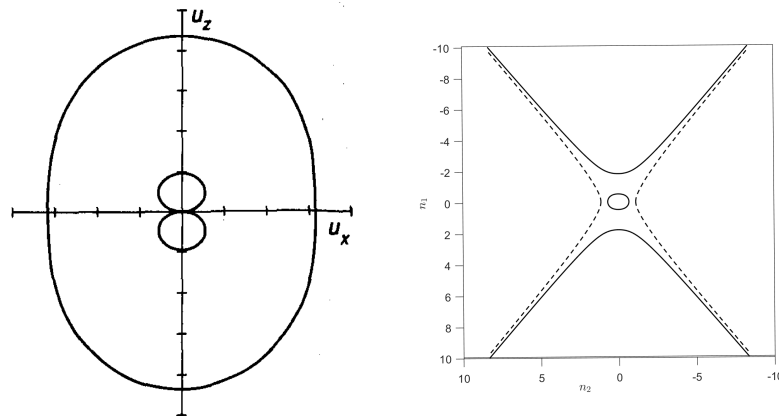


Figure 3.2: Wave normal surfaces of a fast wave (exterior in (a)) and an ion cyclotron wave. Figure (a) corresponds to Stix's [44] representation with $u = 1/n$, namely phase velocity, and (b) was obtained with *wave-explorer* for n , namely normalized wave number or index of refraction.

The two plots in Figure 3.2 are completely equivalent. The difference topology is due to the fact that the right plot was obtained using *wave-explorer* software and is the locus of the tip of the vector $\mathbf{n} = \frac{kc}{\omega} \mathbf{1}_k$, having the direction of wave propagation with magnitude equal to the electric length normalized spatial frequency or refractive index. On the other hand, the surfaces in the left figure have magnitude equal to the normalized phase velocity (representation used by Stix[44]) $\mathbf{u} = \frac{\omega}{kc} \hat{\mathbf{k}} = n^{-1} \mathbf{1}_k$.

Note that there is a resonance in the propagation direction at some angle with respect to the background magnetic field $\mathbf{B} = B_0 \mathbf{1}_z$. In the first plot it is represented by a point in the origin while,

in the second, we can see that $n \rightarrow \infty$ for the two outer branches. The dotted lines correspond to imaginary branches which *wave-explorer* is able to capture. This will be in depth explained in a later section.

It is observed that, when going through a resonance or cutoff, the topology of the wave normal surfaces (one for each mode) can change significantly. P.C Clemmow and R.F. Mullaly gathered in a figure the different normal surfaces found for a single ion collisionless cold plasma [15] as a function of the plasma properties (see Figure 3.3). The number of independent parameters defining P,L and R is only 2 for the case of a single ion species once the ion to electron mass ratio ($\lambda = m_i/m_e$) is known. This is because, assuming charge neutrality, the plasma and cyclotron resonances are precisely related by this ratio.

The transition between regimes may or may not occur for some resonance and can be caused by non-homogeneous plasma properties or by time changes in those properties. For example, an increase in number density of certain species due to ionization caused by heating (more energetic collisions). During that transition, absorption or reflection usually occur. However, this complex topic is out of the scope of the present thesis and no further details will be given. As a reference, T.H. Stix treats extensively the behavior near resonances for several types of plasma waves [44].

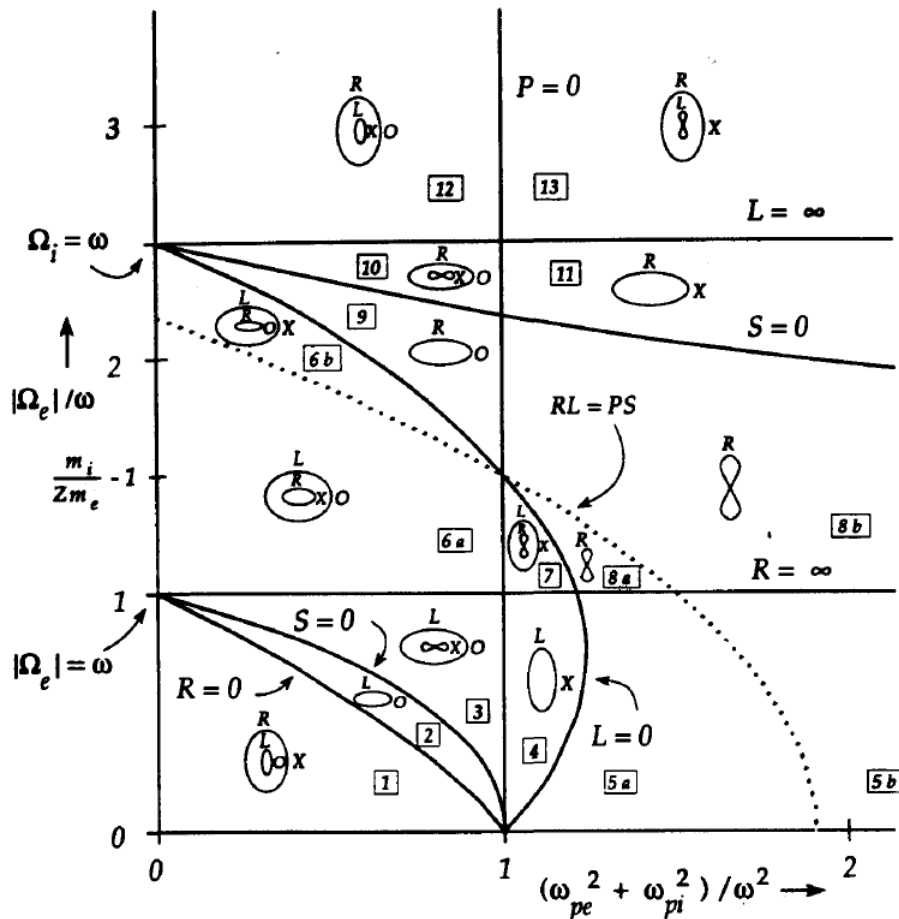


Figure 3.3: Clemmow-Mullaly-Allis diagram for the classification of waves in a cold plasma [44]

The diagram in Figure 3.3 assumes an ion to electron mass ratio of $\lambda = 2.5$, this case is not realistic but was chosen for ease of visualization. For, instance, for argon, the ratio is on the order of $\lambda \approx 10^5$. The independent variables for this two species in a collisionless diagram are Ω_e/ω and $(\omega_{pe}^2 + \omega_{pi}^2)/\omega^2$. The ECRA thruster operation regime lies on regions 7 and 8 where relatively strong magnetic fields are expected. Moreover, downstream the heating region and resonant point, no propagation should

occur corresponding to region 5 on the CMA diagram.

The labeling of the waves is done according to propagation parallel to the static magnetic field and perpendicular to it. It was already shown that the solution for the former case are the two circular polarizations L(for left-hand) and R(for right-hand). Conversely, for perpendicular propagation two other modes are easily recognizable, here labeled as O(for ordinary) and X(for extraordinary). Stix also differentiates between fast wave (outer most mode) and slow wave (inner most mode) to account for phase velocity [44].

All the lines separating regimes, called bounding surfaces in the parameter space[15], correspond to either Cutoff or Resonance. $S = (R + L)/2 = 0$ is indeed a resonance for $\theta = \pi/2$. A more detailed analysis on the features and topological properties of wave normal surfaces and their bounding surfaces is found in the original work by Clemmow and Mullaly [15] and the book by Stix [44]. However, it is important to note that, inasmuch as the diagram does not discriminate between real and imaginary parts of the normal surfaces, only propagating waves are shown and damping due to collisions is not included. The code *wave-explorer* solves this issue enabling the plot of imaginary parts. Nonetheless, Stix actually proves that for a θ interval in which there is not any root giving $n = 0$ or $n = \infty$, the solution remains either real or imaginary but it does not change.

3.2.4 The Electron Cyclotron Resonance

For high enough frequencies, in the range of microwave or even mid RF, ions can be considered as a background fluid with infinite inertia. This is done on the grounds that electron mobility is much higher due to its smaller mass.

L.Tonks and I.Langmuir [33] first used this approximation for the study of plasma oscillations when $P = 0$ or $\omega = \omega_{pe}$. We, in turn, are keen on studying frequencies below those, where $P < 0$, particularly, region 8 in the CMA diagram 3.3. Under the assumption $\frac{m_i}{Zm_e} \ll 1$ it follows $\omega_{pi} \ll \omega_{pe}$ and $|\Omega_i| \ll |\Omega_e|$. The usual plasma parameters for a single ion species then become

$$R \approx 1 - \frac{\omega_{pe}^2}{\omega(\omega + \Omega_e)} \quad (3.52)$$

$$L \approx 1 - \frac{\omega_{pe}^2}{\omega(\omega - \Omega_e)} \quad (3.53)$$

$$P \approx 1 - \frac{\omega_{pe}^2}{\omega^2} \quad (3.54)$$

Taking the determinant in 3.12, equating to 0 and solving for n

$$n^2 = 1 - \frac{2(A - B + C)}{2A - B \pm (B^2 - 4AC)^{1/2}} \quad (3.55)$$

Where A , B and C are parameters in Equation 3.45. After substitution of the new plasma parameters

$$n^2 = 1 - \frac{2\omega_{pe}^2(\omega^2 - \omega_{pe}^2)/\omega^2}{2(\omega^2 - \omega_{pe}^2) - \Omega_e^2 \sin^2 \theta \pm \Omega_e \Delta} \quad (3.56)$$

$$\Delta = [\Omega_e^2 \sin^4 \theta + 4\omega^{-2}(\omega^2 - \omega_{pe}^2)^2 \cos^2 \theta]^{1/2} \quad (3.57)$$

This dispersion relation^[5] attributed to D.R. Hartree and E.V. Appleton¹³ is valid for all the regimes under or near-above $R = \infty$ in the CMA diagram. These are called electron modes because ion motion is completely neglected as a first approximation for wave propagation. Notice that this is an analytic approximation and that a numerical study of the cold plasma is possible retaining all the terms.

Further more, if only the parallel propagation (with respect to the background magnetic field) is to be studied, a quasy-longitudinal approximation is obtained taking into account

$$\Omega_e^2 \sin^4 \theta \ll 4\omega^{-2}(\omega^2 - \omega_{pe}^2)^2 \cos^2 \theta \quad (3.58)$$

$$\Omega_e^2 \sin^2 \theta \ll |2(\omega^2 - \omega_{pe}^2)| \quad (3.59)$$

Accordingly, Equation 3.56 simplifies to the cold plasma longitudinal electron mode dispersion relation

$$n^2 = 1 - \frac{\omega_{pe}^2}{\omega(\omega \pm \Omega_e \cos \theta)} \quad (3.60)$$

It is straight forward to notice that the two solutions correspond to the usual circular polarizations $n^2 = L$ and $n^2 = R$ (See equations 3.52 and 3.53) when $\theta = 0$. As the frequency grows L goes through 0 becoming negative. The refractive index turns into pure imaginary and this mode no longer propagates.

ECR thrusters work in region 8 of the CMA diagram where, parallel to the magnetic field, only the right hand circular polarization mode (R wave) propagates. The **electron cyclotron resonance** arises at $R = \infty$ with $\theta = 0$. Collisions could have been included in the last equations [44].

It is interesting to notice the role of collisions as a damping force preventing pure resonance. The spatial frequency can grow but never go to infinity, physically, the collisions dissipate wave energy into thermal energy due to the randomization in particle motion. This is the heating mechanism and the objective of the engine chamber. It is desired to be close to a resonant point to enhance this heating.

However, this is a problem when it comes to numerical methods as the computational power necessary to resolve higher frequency waves is, generally, proportional to the increase in frequency to the power of the problem dimensions (in our case 2) [45].

¹³Nobel Prize winner for his studies of the ionosphere and his contributions to radar technology

4 Finite Difference Methods

Finite difference methods are based on the discretization of the value of a certain function $f(x)$ over a finite set of points in space x_i (time discretization is also possible) and the approximation of derivatives by algebraic operations [40]. Following this approach, after imposing suitable boundary conditions, it is possible to reduce or approximate a partial differential equation by a system of algebraic equations. Additionally, for electromagnetic problems, these equations are linear and can be analyzed and solved by usual linear algebra techniques [41].

As an example, the centered finite difference approximation for the first derivative is obtained. The position of a given grid point can be written as $x_{i+n} = x_i + nh$ over an uniform 1D mesh i.e. all the points are equally separated by the distance h . The Taylor series around a point x_0 is

$$f(x_0 + h) = f(x_0) + hf'(x_0) + \frac{h^2}{2}f''(x_0) + \frac{h^3}{6}f'''(x_0) + \dots \quad (4.1)$$

$$f(x_0 - h) = f(x_0) - hf'(x_0) + \frac{h^2}{2}f''(x_0) - \frac{h^3}{6}f'''(x_0) + \dots \quad (4.2)$$

The above equations can be combined. Denoting $f^i = f(x_i)$, we solve for the first derivative at node i to obtain [8]

$$\left(\frac{\partial f}{\partial x}\right)^i = \frac{f^{i+1} - f^{i-1}}{2h} + O(h^2) \quad (4.3)$$

Similar procedures can be applied to achieve higher order approximations, in this case, using more than two node points. Forward and backwards approximations can be used instead of centered FDs, this generally lowers the method's order but is useful at the boundaries. Higher order derivatives are also attainable. Although the process is analogous, for the sake of solving Maxwell's equations, cross derivatives are needed, as a consequence, instead of 1D, 2D Taylor expansions are utilized.

The **order** of the scheme is a parameter of enormous importance for numerical methods. Equation 4.3 shows that the error is of the order of h^2 , this means that if the node distance is halved, the error would be four times lower. Higher order schemes are desirable, however, they are difficult to implement, especially, at the boundaries.

FD discretizations are used in each node to represent differential equations. Some of these equations are substituted by boundary constraints at the limits of the problem's domain. For instance, a Dirichlet problem establishes a fixed function value at the boundary. Ultimately, a system of n equations and n unknowns should arise. The system may be solved explicitly if the value in each node can be obtained in consecutive iterations propagating the solution from some initial values. On the other hand, in implicit schemes, all the equations are solved simultaneously using a linear system solver.

Apart from the order of the scheme, there are two other scheme performance indicators. A scheme is **consistent** if the physical solution is obtained in the limit $h \rightarrow \infty$. A propagating scheme is **stable** for a certain step-size if a hypothetical perturbation remains bounded as the iterations go to infinity [24]. This is normally a concern in time evolving methods like FDTD.

4.1 Problem formulation: Frequency domain method

The frequency domain equation provides solutions for the propagation of monochromatic waves. This is representative of the steady state operation of a thruster where an antenna is continuously heating the plasma. It also provides a picture of the absorption and propagation of electromagnetic waves at certain frequencies, this behavior is highly dependant on the excitation frequency which together with the plasma parameters, determines the propagation regime in the CMA diagram 3.3. On the other hand, this method is not able to capture transients and unsteady behavior. For that case, other options are available such as modifications of the vacuum Finite Difference Time Domain (FDTD) algorithm.

Regarding the computational resources consumed by this method, it is generally much faster than time domain methods because the problem only has one ‘time iteration’ after which later time steps are found multiplying by the exponential time expansion term. The frequency domain wave equation 3.9 is shown again below

$$\nabla \times (\nabla \times \hat{\mathbf{E}}) = -\nabla^2 \hat{\mathbf{E}} + \nabla(\nabla \cdot \hat{\mathbf{E}}) = \frac{\omega^2}{c^2} \bar{\bar{\mathbf{k}}} \cdot \hat{\mathbf{E}} + i\omega\mu_0 \hat{\mathbf{j}} \quad (4.4)$$

Where $\mathbf{E}(\mathbf{r}, \omega) \in \mathbb{V} = \{\mathbf{E} : \mathbb{R}^{3+1} \rightarrow \mathbb{C}^3\}$ such that

$$\mathbf{E}(\mathbf{r}, t) = \Re[\hat{\mathbf{E}}(\mathbf{r}, \omega) \exp(-i\omega t)] \quad (4.5)$$

In addition to the usual time expansion, the problem is reduced to 2D with an harmonic expansion along the perpendicular z-direction. The harmonic expansion in the third direction is useful to demonstrate this characteristic for the implementation in the azimuthal direction for axisymmetric codes.

$$\mathbf{E}(\mathbf{r}, t) = \Re[\hat{\mathbf{E}}(\mathbf{r}, \omega) \exp(-i\omega t)] = \Re[\tilde{\mathbf{E}}(x, y, k_z, \omega) \exp(-i\omega t + izk_z)] \quad (4.6)$$

It is convenient to multiply Equation 3.9 by the square of the electric length c/ω (constant for a fixed excitation frequency) before discretizing into the finite difference schemes. This procedure reduces the functional dependence of the matrix of coefficients because the electric length term can be absorbed into non dimensional distances \bar{h} in the scheme equations (see denominator in Equation 4.3)

$$\frac{c^2}{\omega^2} \nabla \times (\nabla \times \tilde{\mathbf{E}}) = \bar{\bar{\mathbf{k}}} \cdot \tilde{\mathbf{E}} + i\frac{c^2}{\omega} \mu_0 \hat{\mathbf{j}} \quad (4.7)$$

In a problem with g nodes, there will be $3g$ degrees of freedom to solved for (three field values per node). All those degrees of freedom are gathered in a vector \mathcal{E} . For all the nodes $p \in \{1, \dots, g\}$ with position vector is \mathbf{r}^p

$$\mathcal{E} \in \mathbb{U} = \{\mathbb{C}^{3g} : \mathcal{E}^l = E_n[\mathbf{r}^p, \omega], n \equiv \{x, y, z\}, p \equiv \{1, 2, \dots, g\}\} \quad (4.8)$$

The discrete current density vector \mathcal{J} can be similarly obtained. Three linear FD equations appear in each node, one for each of the three directions in the vector equation 4.7. Note that boundary conditions can substitute some of these equations. Consequently, there are $3d$ equations for $3d$ unknowns, which can be expressed in the form of a linear system. Introducing the non dimensional position vectors $\mathcal{X} \in \mathbb{R}^g$ and $\mathcal{Y} \in \mathbb{R}^g$ containing the plane coordinates of each node (i.e. \mathcal{X}^p and \mathcal{Y}^p are the components of $(\omega/c)\mathbf{r}^p$), the matrix of coefficients $\bar{\bar{M}} \in \mathbb{C}^{3g \times 3g}$ is

$$\bar{\bar{M}} = \mathcal{N}[\bar{\bar{\kappa}}, \mathcal{X}, \mathcal{Y}] \quad (4.9)$$

$$\bar{\bar{M}} \cdot \mathcal{E} = \mathcal{F} = i \frac{c^2}{\omega} \mathcal{J} \quad (4.10)$$

Where \mathcal{N} is the Finite Difference operator, dependent on the scheme equations, its role is to discretize Equation 4.7 into each node to construct $\bar{\bar{M}}$. This formulation is valid for structure or unstructured grids and homogeneous or non homogeneous media. Once the matrix of coefficients is found, the problem reduces to solving the linear system in 4.10.

Notice that the problem comprises 2 discretizations, both are critical for the performance of the algorithm. Firstly **space** is discretized into a mesh of nodes defined by \mathcal{X} and \mathcal{Y} . Afterwards, the derivatives of the wave equation are discretized into **finite differences**.

We turn now to the study of the Finite Difference operator. The inputs are the non dimensional node position vectors and the dielectric tensor, notice that the non-dimensional form avoids the functional dependence on the excitation frequency. On the other hand, it is necessary to preprocess the dimensional inputs to find the vectors of node coordinates and the forcing term vector \mathcal{F} .

Two different FD discretizations (numerical schemes) are presented below. Each of them has its own advantages and disadvantages in terms of numerical error, implementation and computational performance. These schemes will be later studied by means of numerical wave normal surfaces (Chapter 5) and verified using real simulations (Chapter 6). The two schemes are homogeneous, i.e. the distance between nearby nodes is equal.

Additionally, if the nodes form a Cartesian grid with origin $(\mathcal{X}_0, \mathcal{Y}_0)$ and base formed by $\mathbf{1}_x$ and $\mathbf{1}_y$, it is possible to express the position of each node as

$$\mathcal{X}^{i,j} = \mathcal{X}_0 + i\bar{h}_x \quad \mathcal{Y}^{i,j} = \mathcal{Y}_0 + j\bar{h}_y \quad (4.11)$$

Where $i \in [1, m]$ and $j \in [1, n]$, m and n are the dimensions of the grid or mesh such that the total number of nodes (degrees of freedom) is $d = m \times n$. The node distances \bar{h}_x and \bar{h}_y are dimensionless. Now the field in a node i, j can be written as $\mathcal{E}^{i,j}$. This nomenclature, despite the loss of generality (not valid for unstructured meshes), will be very useful to write the scheme equations.

Note that \mathcal{E} has to be a vector to be input into the linear system solver. The way the components of this vector and the coefficients of $\bar{\bar{M}}$ are arranged is not important as long as it is consistent. The specific details depend on the code and there is not a unique correct organization, more details on the particular way *fdwaves* does this are provided in Chapter 6. The aim of this section is to show the equations that constitute the system. First, the equations used for the center of the domain (almost all nodes) are presented. Later, the necessary boundary conditions to close the system are explained.

4.2 Scheme Equations

4.2.1 Non staggered grid: Sofd3 scheme

A straightforward scheme able to discretize the Maxwell's equations uses centered second order FDs for the first, cross and second derivatives using the closest nearby nodes.

This scheme is simple to implement, additionally it requires a small computational effort during the construction of the matrix of coefficients. The 3×3 computational cell is easily adaptable to simple boundary conditions, moreover, forward differences for the boundaries only require a minor modification in the scheme.

Despite all those advantages, this scheme has several limitations. It can be shown that this setup does not maintain the divergence free characteristic of the electric displacement field (first of Maxwell's 3.1) [32]. This feature limits the capabilities of the scheme. Especially in vacuum, spurious solutions appear with a high excitation frequency and a very fine mesh is needed. This undesired behavior is improved inside a collisional plasma. Chapter 5 analyzes the dispersion relation solutions for this scheme.

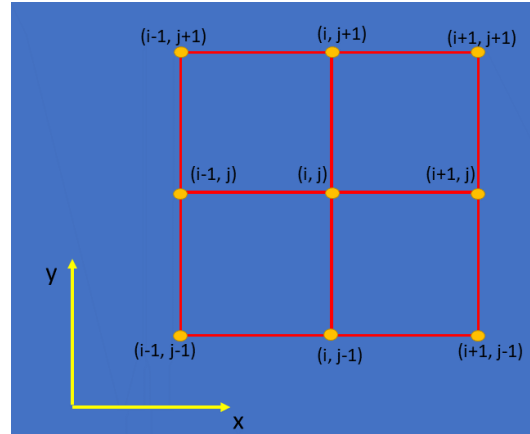


Figure 4.1: Sofd3 Computational Cell

The dielectric tensor components are expressed as $\bar{\bar{\kappa}} = \begin{bmatrix} \kappa_{xx} & \kappa_{xy} & \kappa_{xz} \\ \kappa_{yx} & \kappa_{yy} & \kappa_{yz} \\ \kappa_{zx} & \kappa_{zy} & \kappa_{zz} \end{bmatrix}$

The first derivatives in each direction are (Recall that z derivatives are Fourier expanded):

$$\frac{\partial f}{\partial x} \equiv \frac{f^{i+1,j} - f^{i-1,j}}{2h_x} \quad (4.12)$$

$$\frac{\partial f}{\partial y} \equiv \frac{f^{i,j+1} - f^{i,j-1}}{2h_y} \quad (4.13)$$

$$\frac{\partial f}{\partial z} = ik_z f \quad (4.14)$$

Likewise, second derivatives can be approximated by:

$$\frac{\partial^2 f}{\partial x^2} \equiv \frac{f^{i+1,j} + f^{i-1,j} - 2f^{i,j}}{h_x^2} \quad (4.15)$$

$$\frac{\partial^2 f}{\partial y^2} \equiv \frac{f^{i,j+1} + f^{i,j-1} - 2f^{i,j}}{h_y^2} \quad (4.16)$$

$$\frac{\partial^2 f}{\partial z^2} = -k_z^2 f \quad (4.17)$$

And, finally, the cross derivatives read:

$$\frac{\partial^2 f}{\partial x \partial y} \equiv \frac{f^{i+1,j+1} + f^{i-1,j-1} - f^{i+1,j-1} - f^{i-1,j+1}}{(2h_x)(2h_y)} \quad (4.18)$$

$$\frac{\partial^2 f}{\partial x \partial z} = ik_z \frac{\partial f}{\partial x} \equiv ik_z \frac{f^{i+1,j} - f^{i-1,j}}{2h_x} \quad (4.19)$$

$$\frac{\partial^2 f}{\partial y \partial z} = ik_z \frac{\partial f}{\partial y} \equiv ik_z \frac{f^{i,j+1} - f^{i,j-1}}{2h_y} \quad (4.20)$$

Once the derivatives have been obtained, the vector equation in each node can be written as three different discretized equations with coefficients multiplying the computational cell nodes. The gathering of those coefficients into a compact matrix can be performed by a code such as *fdwaves*, more details about the process are provided at Chapter 6. The scheme equations are presented below, for instance, in the x-direction, we express the vector calculus operators in Cartesian coordinates

$$-\left(\frac{\partial^2 \hat{E}_x}{\partial x^2} + \frac{\partial^2 \hat{E}_x}{\partial y^2} + \frac{\partial^2 \hat{E}_x}{\partial z^2}\right) + \frac{\partial^2 \hat{E}_x}{\partial x^2} + \frac{\partial^2 \hat{E}_y}{\partial x \partial y} + \frac{\partial^2 \hat{E}_z}{\partial x \partial z} = \frac{\omega^2}{c^2} \bar{\kappa} \hat{\mathbf{E}} \cdot \mathbf{1}_x + i\omega\mu_0 j_x \quad (4.21)$$

Now, these derivatives are approximated by Finite Differences, the residual is not shown but can be proven to be $O(h^2)$. Using non-dimensional distances in the denominator of the derivatives and with a forcing term equal $f_x = i(c^2/\omega)j_x$, the FD equation in the x direction is

$$\begin{aligned} & -\frac{\mathcal{E}_x^{i,j+1} + \mathcal{E}_x^{i,j-1} - 2\mathcal{E}_x^{i,j}}{\bar{h}_y^2} + \frac{\mathcal{E}_y^{i+1,j+1} + \mathcal{E}_y^{i-1,j-1} - \mathcal{E}_y^{i+1,j-1} - \mathcal{E}_y^{i-1,j+1}}{(2\bar{h}_x)(2\bar{h}_y)} + \\ & + \bar{k}_z^2 \mathcal{E}_x + i\bar{k}_z \frac{\mathcal{E}_z^{i+1,j} - \mathcal{E}_z^{i-1,j}}{2\bar{h}_x} - (\kappa_{xx}\mathcal{E}_x^{i,j} + \kappa_{xy}\mathcal{E}_y^{i,j} + \kappa_{xz}\mathcal{E}_z^{i,j}) = f_x^{i,j} \end{aligned} \quad (4.22)$$

Where the non dimensional wave number in the z-direction is $\bar{k}_z = (c/\omega)k_z$. Likewise, the equation in the y direction is

$$-\left(\frac{\partial^2 \hat{E}_y}{\partial x^2} + \frac{\partial^2 \hat{E}_y}{\partial y^2} + \frac{\partial^2 \hat{E}_y}{\partial z^2}\right) + \frac{\partial^2 \hat{E}_y}{\partial y^2} + \frac{\partial^2 \hat{E}_x}{\partial x \partial y} + \frac{\partial^2 \hat{E}_z}{\partial y \partial z} = \frac{\omega^2}{c^2} \bar{\kappa} \hat{\mathbf{E}} \cdot \mathbf{1}_y + i\omega\mu_0 j_y; \quad (4.23)$$

$$\begin{aligned} & -\frac{\mathcal{E}_y^{i+1,j} + \mathcal{E}_y^{i-1,j} - 2\mathcal{E}_y^{i,j}}{\bar{h}_x^2} + \frac{\mathcal{E}_x^{i+1,j+1} + \mathcal{E}_x^{i-1,j-1} - \mathcal{E}_x^{i+1,j-1} - \mathcal{E}_x^{i-1,j+1}}{(2\bar{h}_x)(2\bar{h}_y)} + \\ & + \bar{k}_z^2 \mathcal{E}_y + i\bar{k}_z \frac{\mathcal{E}_z^{i,j+1} - \mathcal{E}_z^{i,j-1}}{2\bar{h}_y} - (\kappa_{yx}\mathcal{E}_x^{i,j} + \kappa_{yy}\mathcal{E}_y^{i,j} + \kappa_{yz}\mathcal{E}_z^{i,j}) = f_y^{i,j} \end{aligned} \quad (4.24)$$

And in the z direction we have

$$-\left(\frac{\partial^2 \hat{E}_z}{\partial x^2} + \frac{\partial^2 \hat{E}_z}{\partial y^2} + \frac{\partial^2 \hat{E}_z}{\partial z^2}\right) + \frac{\partial^2 \hat{E}_z}{\partial z^2} + \frac{\partial^2 \hat{E}_x}{\partial x \partial z} + \frac{\partial^2 \hat{E}_y}{\partial y \partial z} = \frac{\omega^2}{c^2} \bar{\kappa} \hat{\mathbf{E}} \cdot \mathbf{1}_z + i\omega\mu_0 j_z; \quad (4.25)$$

$$\begin{aligned} & -\frac{\mathcal{E}_z^{i+1,j} + \mathcal{E}_z^{i-1,j} - 2\mathcal{E}_z^{i,j}}{\bar{h}_x^2} - \frac{\mathcal{E}_z^{i,j+1} + \mathcal{E}_z^{i,j-1} - 2\mathcal{E}_z^{i,j}}{\bar{h}_y^2} + i\bar{k}_z \frac{\mathcal{E}_x^{i+1,j} - \mathcal{E}_x^{i-1,j}}{2\bar{h}_x} + \\ & i\bar{k}_z \frac{\mathcal{E}_y^{i,j+1} - \mathcal{E}_y^{i,j-1}}{2\bar{h}_y} - (\kappa_{zx}\mathcal{E}_x^{i,j} + \kappa_{zy}\mathcal{E}_y^{i,j} + \kappa_{zz}\mathcal{E}_z^{i,j}) = f_z^{i,j} \end{aligned} \quad (4.26)$$

4.2.2 Yee staggered grid modification: Sofd5 scheme

The following method uses a 5×5 computational cell (although some of the nodes are not actually used), basically it keeps using the same nodes as Sofd3 for the first and cross derivatives but uses outer nodes for the second derivatives. The scheme is second order although it should be noted that, from the Taylor series, this order refers to the distance to the outer nodes $O(2h^2) = 4O(h)$ i.e. for the same number of nodes, we expect an error about 4 times greater than with Sofd3 scheme, at least for the second derivatives. Due to the use of a different uncoupled grid for the second derivatives, this scheme also struggles solving problems with discrete (single node) current density sources, this can be solved providing a smooth but sharp distribution across several nodes. Uncoupling is mainly a concern for vacuum. When a full dielectric tensor is present (as in plasma), the grids are no longer independent. Boundary conditions are difficult to map with Sofd5, nevertheless, there exist solutions available including forward differences modifications.

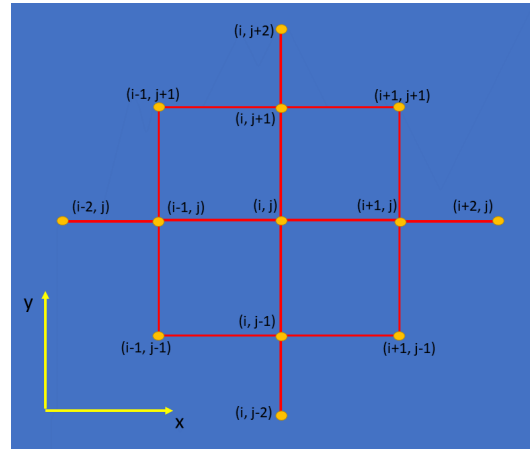


Figure 4.2: Sofd5 Computational Cell

Although it has several disadvantages, including the difficulty to implement into code, Sofd5 also presents a better behavior in terms of spurious solutions. Its good performance is especially noticeable for vacuum propagation where it can be proven that there are no spurious solutions at all. This method is a modification of the staggered computational cell from the original Finite Difference Time Domain Method proposed by Yee in the 1960s [47]. Yee method uses two different grids for the electric and magnetic fields to solve electromagnetic problems in isotropic media. The staggered grid approach guarantees the condition of zero divergence in the electric displacement imposed by the Maxwell's equations 3.1 for zero charge density (vacuum). Due to the presence of a non isotropic dielectric tensor in a cold plasma, it is necessary to have FD coefficients for the electric field in each node to close the problem. This has already been done by interpolating the field, but it was shown that interpolation produces additional errors that eliminate the desirable non-divergent behavior [37]. Sofd5 can maintain the convenient performance of Yee method while evaluating the electric field in all the nodes and avoiding interpolation. These properties will be studied in-depth in Chapter 5 on wave normal surfaces.

The first and cross derivatives are the same for Sofd3 and Sof5, they use the inner rectangle nodes in the computational cell. However, the second derivative approximations are different because the outer nodes are used

$$\frac{\partial^2 f}{\partial x^2} \equiv \frac{f^{i+2,j} + f^{i-2,j} - 2f^{i,j}}{(2h_x)^2} \quad (4.27)$$

$$\frac{\partial^2 f}{\partial y^2} \equiv \frac{f^{i,j+2} + f^{i,j-2} - 2f^{i,j}}{(2h_y)^2} \quad (4.28)$$

$$\frac{\partial^2 f}{\partial z^2} = -k_z^2 f \quad (4.29)$$

Due the change in second derivatives, the FD scheme equations are slightly modified

Equation in the x-direction:

$$\begin{aligned}
 & -\frac{\mathcal{E}_x^{i,j+2} + \mathcal{E}_x^{i,j-2} - 2\mathcal{E}_x^{i,j}}{(2\bar{h}_y)^2} + \frac{\mathcal{E}_y^{i+1,j+1} + \mathcal{E}_y^{i-1,j-1} - \mathcal{E}_y^{i+1,j-1} - \mathcal{E}_y^{i-1,j+1}}{(2\bar{h}_x)(2\bar{h}_y)} + \\
 & + \bar{k}_z^2 \mathcal{E}_x + i\bar{k}_z \frac{\mathcal{E}_z^{i+1,j} - \mathcal{E}_z^{i-1,j}}{2\bar{h}_x} - (\kappa_{xx}\mathcal{E}_x^{i,j} + \kappa_{xy}\mathcal{E}_y^{i,j} + \kappa_{xz}\mathcal{E}_z^{i,j}) = f_x^{i,j}
 \end{aligned} \tag{4.30}$$

Equation in y-direction:

$$\begin{aligned}
 & -\frac{\mathcal{E}_y^{i+2,j} + \mathcal{E}_y^{i-2,j} - 2\mathcal{E}_y^{i,j}}{(2\bar{h}_x)^2} + \frac{\mathcal{E}_x^{i+1,j+1} + \mathcal{E}_x^{i-1,j-1} - \mathcal{E}_x^{i+1,j-1} - \mathcal{E}_x^{i-1,j+1}}{(2\bar{h}_x)(2\bar{h}_y)} + \\
 & + \bar{k}_z^2 \mathcal{E}_y + i\bar{k}_z \frac{\mathcal{E}_z^{i,j+1} - \mathcal{E}_z^{i,j-1}}{2\bar{h}_y} - (\kappa_{yx}\mathcal{E}_x^{i,j} + \kappa_{yy}\mathcal{E}_y^{i,j} + \kappa_{yz}\mathcal{E}_z^{i,j}) = f_y^{i,j}
 \end{aligned} \tag{4.31}$$

Equation in z-direction:

$$\begin{aligned}
 & -\frac{\mathcal{E}_z^{i+2,j} + \mathcal{E}_z^{i-2,j} - 2\mathcal{E}_z^{i,j}}{(2\bar{h}_x)^2} - \frac{\mathcal{E}_z^{i,j+2} + \mathcal{E}_z^{i,j-2} - 2\mathcal{E}_z^{i,j}}{(2\bar{h}_y)^2} + i\bar{k}_z \frac{\mathcal{E}_x^{i+1,j} - \mathcal{E}_x^{i-1,j}}{2\bar{h}_x} + \\
 & i\bar{k}_z \frac{\mathcal{E}_y^{i,j+1} - \mathcal{E}_y^{i,j-1}}{2\bar{h}_y} - (\kappa_{zx}\mathcal{E}_x^{i,j} + \kappa_{zy}\mathcal{E}_y^{i,j} + \kappa_{zz}\mathcal{E}_z^{i,j}) = f_z^{i,j}
 \end{aligned} \tag{4.32}$$

4.3 Boundary conditions

Some of the above equations must be substituted in the domain boundaries to correctly model physical problems. At the time the thesis was written two boundary conditions were available and implemented into *fdwaves*, namely, periodic and perfect electric conductor (PEC) conditions. There is also a third kind of conditions under development. Perfectly Matched Layers (PML) absorb a propagating wave without any reflection, consequently, these boundaries are suitable for modeling infinite domains in which waves simply travel out of the source toward infinity. This problem would be, otherwise, impossible to model because simulating an infinite domain is not feasible with a finite number of nodes. PML conditions are further discussed in Section 8.6.

4.3.1 Periodic Conditions

We might be interested in modeling periodic structures extending to infinity. This is, for a domain with certain forcing term in some of its nodes, there are nearby identical domains extending in x and y-directions and repeated infinite times. For example, this approach can be useful to model 1D problems while working with a 2D code. An infinite line of current density can be set in the y-direction selecting periodic conditions in the upper and lower walls, note that the lateral walls can still be PEC. One such simulation is shown in Figure 4.3. Standing waves can be observed due to the wall reflections.

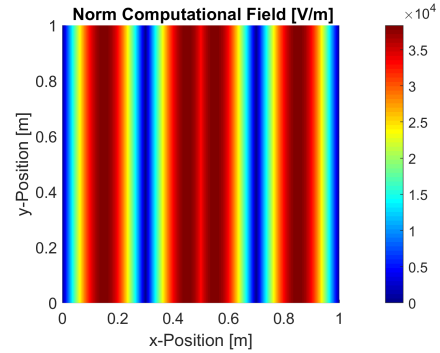


Figure 4.3: 1D vacuum simulation at 500MHz. Central foil of current in z-direction. Showing the norm of E_z field. PEC lateral walls.

Periodic conditions are the easiest to implement. No change of the scheme equations is required. The procedure is based on identifying a node out of the domain when it appears in the equations. Afterwards, the outer nodes are mapped with the first nodes. For instance, for a domain with dimensions $m \times n$, in the x-direction, a node $i = m + 1$ is automatically mapped to $i = 1$, similarly, $m + 2 \rightarrow 2$ or $-1 \rightarrow m - 1$. Notice that $m + 2$ is the further node required by Sofd5 when the equations are taken at node m . This circularly connects the end of the domain with the beginning. The process can be efficiently implemented into numerical codes as *fdwaves*.

4.3.2 Perfect Electric Conductor (PEC)

The other boundary type implemented into *fdwaves* corresponds to the modeling of Perfect Electric Conductor (PEC) walls. Unlike, periodic conditions or PML, PEC elements can not only be applied to the outer boundaries of the domain but it is also possible to simulate internal conducting geometric features. These elements are a very good approximation to metallic parts in which conductivity is very high $\sigma \rightarrow \infty$. Electromagnetic theory states that there is free motion of particles inside a perfect conductor. This means that any perturbation or field in the interior of the conductor is immediately canceled out by the redistribution of charges across its boundaries to assure that there are not electric potential differences ΔV (this is the minimum energy state). Mathematically, this implies that there cannot exist a tangential electric field on the skin of the conductor $\mathbf{E} \times \mathbf{1}_n = 0$, where $\mathbf{1}_n$ is the vector normal to the conducting surface. Due to the Fourier expansion in the z-direction, any conducting structure would be infinite in this direction, hence, the first equation common to any PEC node is straightforward, the tangential field must be null $E_z = 0$.

The remaining two equations (we need three equations in each node) depend on the orientation of the walls where they are applied. In particular, the equations for a corner node are also simple. Any x or y field at a corner would produce charged particle's free motion in those directions, therefore, the tangential fields at a corner must be zero $E_x = 0$ and E_y .

Things are not so simple for straight walls, for example, let's take the wave equation in the y-direction and apply it to a wall perpendicular i.e. oriented in the x-direction. If the equation is written in a node belonging to the upper wall $j = n$, we cannot use the node $j + 1$ because it is out of the domain. A possible modification of Sofd3 could use forward differences for the cross derivatives

$$\frac{\partial^2 f}{\partial x \partial y} \equiv \frac{f^{i+1,j} + f^{i-1,j-1} - f^{i+1,j-1} - f^{i-1,j}}{(2h_x h_y)}; \quad \frac{\partial^2 f}{\partial y \partial z} = ik_z \frac{\partial f}{\partial y} \equiv ik_z \frac{f^{i,j} - f^{i,j-1}}{h_y} \quad (4.33)$$

After which the scheme equation for the x-direction at a node (i, j) is

$$- \left(\frac{\partial^2 \hat{E}_y}{\partial x^2} + \frac{\partial^2 \hat{E}_y}{\partial y^2} + \frac{\partial^2 \hat{E}_y}{\partial z^2} \right) + \frac{\partial^2 \hat{E}_y}{\partial y^2} + \frac{\partial^2 \hat{E}_x}{\partial x \partial y} + \frac{\partial^2 \hat{E}_z}{\partial y \partial z} = \frac{\omega^2}{c^2} \bar{k} \hat{\mathbf{E}} \cdot \mathbf{1}_y + i\omega\mu_0 j_y; \quad (4.34)$$

$$- \frac{\mathcal{E}_y^{i+1,j} + \mathcal{E}_y^{i-1,j} - 2\mathcal{E}_y^{i,j}}{\bar{h}_x^2} + \frac{\mathcal{E}_x^{i+1,j} + \mathcal{E}_x^{i-1,j-1} - \mathcal{E}_x^{i+1,j-1} - \mathcal{E}_x^{i-1,j}}{(2\bar{h}_x \bar{h}_y)} + \bar{k}_z^2 \mathcal{E}_y + i\bar{k}_z \frac{\mathcal{E}_z^{i,j} - \mathcal{E}_z^{i,j-1}}{\bar{h}_y} - (\kappa_{yx} \mathcal{E}_x^{i,j} + \kappa_{yy} \mathcal{E}_y^{i,j} + \kappa_{yz} \mathcal{E}_z^{i,j}) = f_y^{i,j} \quad (4.35)$$

It may be observed that the node $j + 1$ was not used at all. However, this has a price, the error of the scheme is $O(h)$ instead of $O(h^2)$. This explains the need for non-uniform grids capable of providing a higher node density near the boundaries and other critical areas (see section 8.1). Similar lower order equations can be used for the other types of walls. The code should be able to classify the PEC nodes

in any of the 5 categories (corner upper, lower, left and right walls) to apply the correct equations in each of them and allow for arbitrary PEC geometries, not only at the boundaries, but throughout the whole domain. It is also necessary to avoid configurations with single boundary nodes inside the domain because they do not have a clear physical meaning, Chapter 6 explains how this is done in *fdwaves*.

For simplicity, only 3×3 computational cells (Sofd3 modifications) are used in PEC nodes. However, Sofd5 needs two layers of boundary conditions because it uses a 5×5 cell ($i \pm 2$ and $j \pm 2$ nodes). The solution is to identify nodes belonging to the second or ‘neighbor’ layer and apply Sofd3 on them.

5 Von Neumann Analysis of Numerical Dispersion

In order to examine the accuracy of the numerical schemes presented, a modified Von Neumann analysis is proposed. This method was first aimed at analyzing the stability of time-domain finite difference schemes. It appear in an article by Crank and Nicolson [18] and was later developed by John Von Neumann.

The analysis builds on the decomposition of the numerical error in the form of complex exponential terms (Fourier decomposition) [24]. Following a procedure similar to the one described to get the analytic dispersion relation, the stability, or in our case the accuracy, may be obtained. The method is applied to the equations in a single node. For the sake of studying the unforced propagation through the scheme, the forcing term is set to zero locally. It is also assumed that, locally, the dispersion relation can be approximated by the infinite homogeneous plasma wave equation. This is done on the grounds that gradients in the plasma properties are smooth enough.

Less formally, the analysis studies the change in magnitude and topology that suffers a free monochromatic electromagnetic wave in its most general form $\mathbf{u} = \tilde{\mathbf{u}} \exp(-i\omega t + i\mathbf{k} \cdot \mathbf{r})$ in going through a computational cell. This is later compared with the actual analytic propagation solution. Consequently, this study provides the wave normal surfaces for the numerical scheme which can be compared with the analytic surfaces to find divergent or **spurious solutions** in every possible propagation direction with respect to the grid orientation and the background magnetic field.

However, the Von Neumann analysis is strictly local and applied to a single computational cell. Details regarding boundary conditions, specially absorbing ones, and inhomogeneous media are disregarded. The generalized accuracy verification is, therefore, complicated and may relay on comparison against known analytic solutions or other numerical methods.

5.1 Formulation

For a scheme with a local computational cell of size g_L ($g_L = 25$ for Sofd5 and $g_L = 9$ for Sofd3) there are 3 equations in each node with $3g_L$ unknowns, as a consequence, the system is underdetermined. Due to the linearity of the finite difference method, the unforced system can be expressed as

$$\bar{M}_L \cdot \mathcal{E}_L = 0 \quad (5.1)$$

Where $\bar{M}_L \in \mathbb{C}^{3 \times 3g_L}$ is the local matrix of coefficients and \mathcal{E}_L is the vector containing the electric field in the local nodes such that

$$\mathcal{E}_L \in \mathbb{U} = \{ \mathbb{C}^{3d_L} : \mathcal{E}_L^l = E_n(\omega, \mathbf{r}^p), n \equiv \{x, y, z\}, p \equiv \{1, 2, \dots, d_L\} \} \quad (5.2)$$

Where the position of each node \mathbf{r}^p is given by the grid or stencil used. This formulation is valid also for non-uniform grids. The electric field may be expanded in exponential terms in space, we restrict the solution to

$$\mathbf{E}(\omega, \mathbf{r}) \in \tilde{\mathbb{V}} = \{ \mathbf{E} \equiv \tilde{\mathbf{E}}(\omega, \mathbf{k}) \exp(i\mathbf{k} \cdot \mathbf{r}), \tilde{\mathbf{E}} \in \mathbb{C}^3, \mathbf{k} \in \mathbb{C}^3 \} \quad (5.3)$$

Under that condition, the field components in different nodes are no longer independent for a given spatial frequency. Therefore, the system of equations reduces to 3 equations and 3 unknowns. The unknowns been the field components in any of the d_L nodes of the stencil. Once the fields in one node are known the exponential expansion immediately relates the other nodes. The selection of the

‘origin’ node is arbitrary, it produces a multiplying term coming out of the exponential that can be canceled out when solving the homogeneous system.

$$\tilde{\mathcal{E}}_L \in \tilde{\mathcal{U}} = \left\{ \mathbb{C}^3 : \tilde{\mathcal{E}}_L^k = \tilde{E}_n(\omega, \mathbf{k}), n \equiv \{x, y, z\} \right\} \quad (5.4)$$

The undetermined in Equations 5.1 collapses to a 3×3 system, with $\bar{N} \in \mathbb{C}^{3 \times 3}$. Furthermore, if the stencil is uniform in x and y-directions (i.e. there is the same distance between nodes along a direction), the matrix of coefficients can only depend on the excitation frequency, the spatial frequency, the medium (dielectric tensor) and the node distances.

$$\bar{N}(\omega, \mathbf{k}, \bar{\mathbf{k}}, h_x, h_y) \cdot \tilde{\mathcal{E}}_L = 0 \quad (5.5)$$

In general the excitation frequency ω is a complex number, this often leads to the instability of time domain finite difference methods because an exponential factor can multiply the oscillatory field in Equation 5.3 making the field either go to 0 as time passes or grow unbounded.

Conversely, for frequency domain methods, it is possible to further reduce the possible solutions of the characteristic equation 5.5 by setting explicitly $\omega \in \mathbb{R}$. Moreover, dimensional analysis shows that the functional dependence can be scaled down dividing all the terms in the scheme equations by the electric length c/ω . Including the refractive index vector, the dispersion relation becomes

$$\det[\bar{N}(\mathbf{n}, \bar{\mathbf{k}}, \bar{h}_x, \bar{h}_y, \bar{h}_z)] = 0 \quad (5.6)$$

Where $\mathbf{n} = k(c/\omega)\mathbf{1}_k$ and the non-dimensional grid spacing is $\bar{h} = (\omega/h)c$. For convenience, the numerical wave normal surfaces will be plotted with the refractive index magnitude and the same direction as the propagation vector thus being inversely proportional to the wavelength. In general this is a complex vector

$$\mathbf{n} = (n_r + in_i)\mathbf{1}_k \in \mathbb{C}^3 : \{n_r \in \mathbb{R}, n_i \in \mathbb{R}, \mathbf{1}_k \in \mathbb{R}^3\} \quad (5.7)$$

5.2 The *wave-explorer* tool

Obtaining the wave normal surfaces of several numerical schemes is not a simple task. Not only the solutions may diverge from the two analytic modes but completely new surfaces may appear, these are spurious solutions. *Wave-Explorer* is a Matlab code implementing a numerical algorithm capable of finding those surfaces. This software was created by Professor Mario Merino [37] and has been later modified by the author of this thesis to include the study of non-uniform grids.

Plotting the numerical and analytic wave normal surfaces in the same diagram enables a quick identification of spurious and divergent solutions and, thus, a rapid assessment on the validity of the scheme used for a given grid spacing. It also differentiates between real and imaginary parts making possible to detect directions of wave evanescence and of possible propagation.

For the sake of simplicity, the propagation on the plane of the computational cell will be presented. Note that the last version of the code can reproduce any propagation plane for 2D codes like *fdwaves* and is also prepared for more complex 3D grids.

Besides the stencil (the nodes positions on the computational cell) the other input parameters are the plasma properties and the background magnetic field. Both features are modeled by the cold plasma dielectric tensor and *wave-explorer* includes a tool to build it from the fundamental properties. The combined effect of the stencil orientation and the magnetic field orientation creates anisotropy in the

wave propagation depending on the direction (for the analytic case the only cause is the magnetic field).

The algorithm relies on finding a starting point in terms of real and imaginary parts of the dimensionless propagation vector n_r, n_i satisfying the case of study dispersion relation, this is, for a given angle with respect to the static magnetic field, a certain plane of propagation, in a defined stencil and scheme and with a fixed dielectric tensor.

Note that, provided that the magnetic field vector is known, the propagation vector $\mathbf{1}_k$ is fully defined knowing the propagation plane and the angle of this vector with B_0 so the vector $\mathbf{n} = (n_r + in_i)\mathbf{1}_k$ is completely characterized. To plot the normal surface, the propagation vector can be represented on the propagation plane (previously defined) with separated lines for the real and imaginary parts and components parallel and perpendicular to the static magnetic field n_{\parallel} and n_{\perp} . The components can also be projected in Cartesian coordinates n_x and n_y .

The wave normal surfaces may or may not be continuous so several branches can appear in the diagram. For selecting the starting branch points *wave-explorer* includes a branch finder tool. The user must provide a propagation plane and angle, afterwards, a large number of configurations for n_r and n_i are evaluated.

A contour plot (see Figure 5.1) is used to show the interpolated lines of zero dispersion both for the real and imaginary parts (blue and red lines). The intersection of those lines is a solution for a certain propagation angle. However, in order to plot the normal surfaces, the solution for the rest of angles is needed. Continuation of solutions relies on the fact that the the normal surface lines should remain unbroken (continuous) to ensure consistency. Therefore, a differential change in the propagation angle can only produce a differential change in n_r and n_i . The user will manually chose which points will be selected for branch continuation in *wave-explorer* (for example a point with a very large spatial frequency could be ignored).

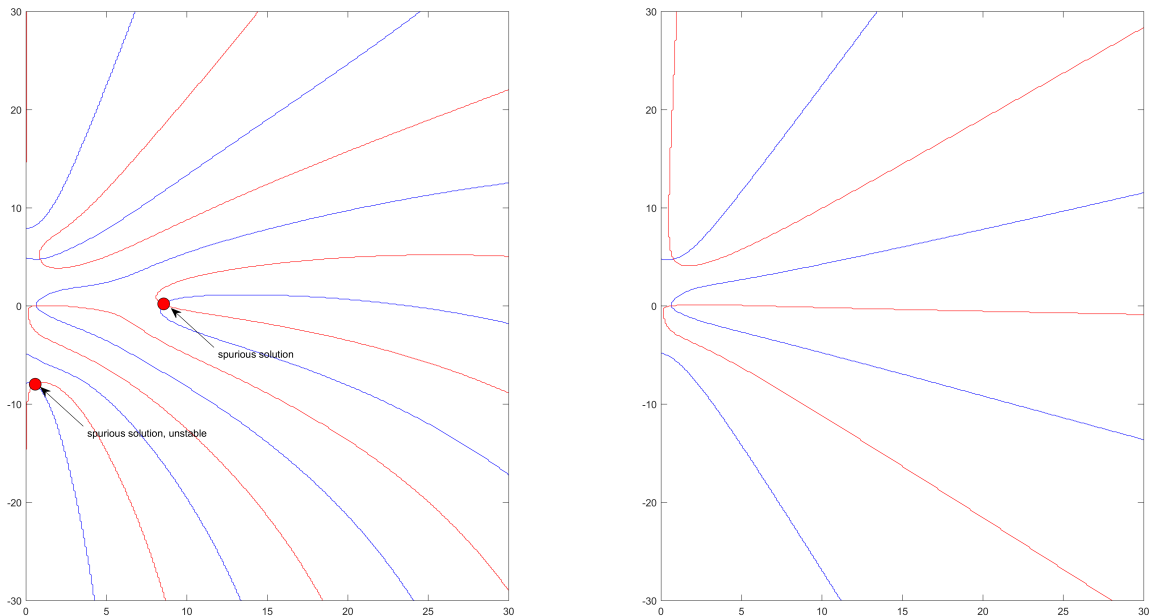


Figure 5.1: Contour plots for numerical dispersion Sofd3 left and analytic dispersion right. The points of intersection are solutions. Note that the numerical scheme has spurious solutions.

Having found a starting point, linearization is used to find a nearby point within a defined arc length (smaller means more precision) on the propagation plane. The new point is the initial guess for a numerical root finder (Newton Method) which further refines its position. The process is continued until the branch is completed. This is known as the method of continuation of solutions. Throughout

the whole process, the dispersion relation is needed. For this task, a code was implemented capable of building the reduced matrix from the finite difference coefficients presented in section 4.2. The gradient is also necessary for linearization and solver speed (it could be obtained numerically at a higher computational cost). Regarding non-uniform grids, the process is slightly different as it uses an automated tool to get the coefficients from the node positions. This code will be explained in depth in section 8.1.

Figure 5.2 shows a flow chart of the *wave-explorer* algorithm including the branch finder utility. Notice that this only includes the numerical dispersion part. There are analytic procedures to find the wave normal surfaces for the analytic dispersion [44], however, continuation of solutions (a numerical approach) was also used as *wave-explorer* allows to easily change the dispersion from the finite difference scheme coefficients to the determinant in equation 3.42.

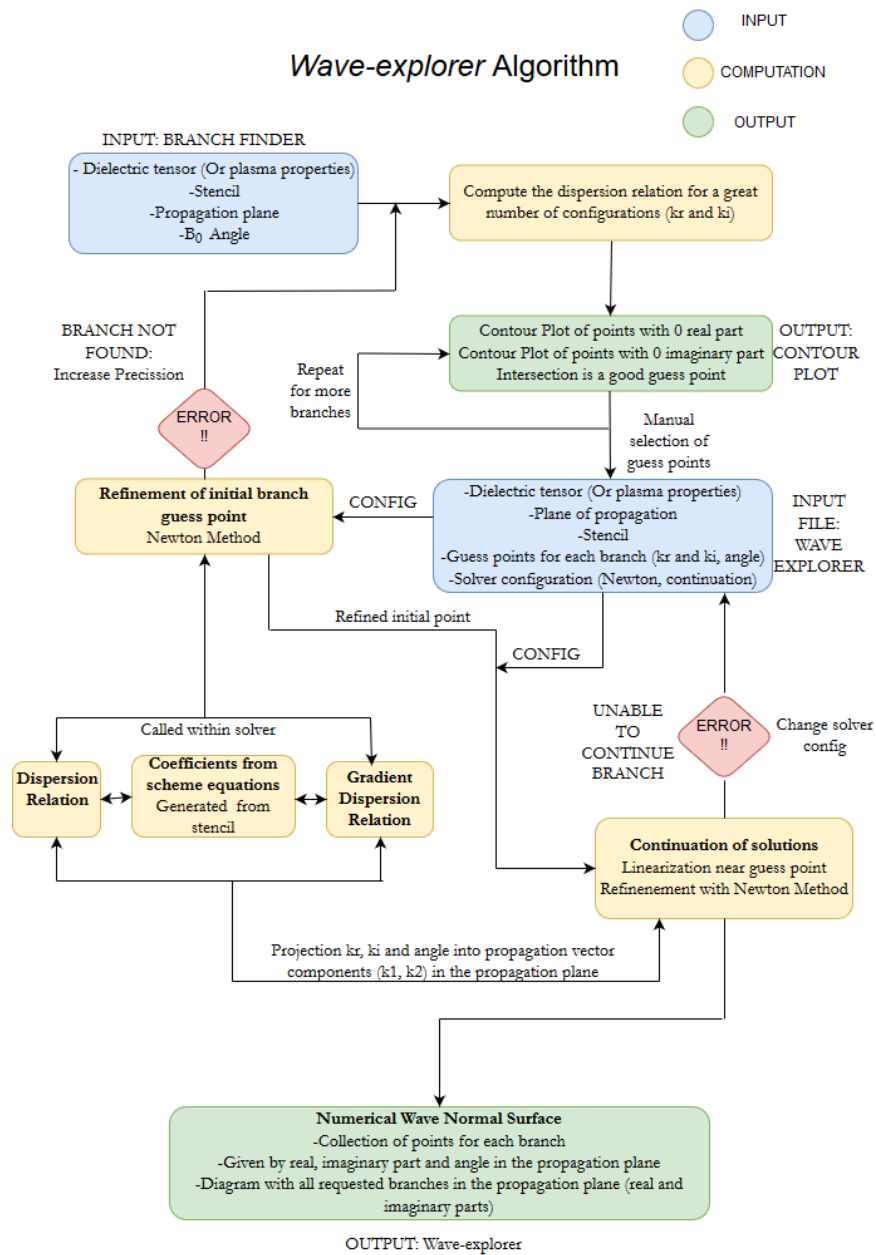


Figure 5.2: *Wave-explorer* code Flow Chart

5.3 Numerical wave normal surfaces

In the following section some wave normal surfaces will be shown. The diagrams include analytic and finite difference solutions for representative cases. The schemes studied are Sofd3 and Sofd5, their different behavior is clearly observed. The plasma configurations chosen correspond to typical regimes for ECR and Helicon thrusters.

Besides those realistic solutions, vacuum and collisionless configurations are considered as they provide interesting information about the propagation phenomena (for instance collisionless resonance) and also serve as means to check the code (the vacuum surfaces are easy to find).

It is important to make a distinction among the different types of errors that may produce numerical surfaces not coincident with the analytic ones:

- **Spurious solutions** are non-physical solutions that arise due to numerical artifacts in the scheme equations. They are a serious issue as, even if they appear for a single propagation direction, they can destabilize a full simulation by interference with reflected or incident waves.
- **Numerical Dispersion** occurs when the real part of the numerical wave is not coincident with the real analytic part. This implies a change in the phase velocity and wavelength. Nonphysical phenomena like superluminal propagation could occur.
- **Numerical Dissipation or Growth** occurs when the imaginary part of the numerical wave is not coincident with the imaginary analytic part. This implies a different damping rate in the case of collisional plasma.

Lastly, although it is not directly observed in the normal surfaces plot, **Numerical Diffusion** occurs due to the difference in the phase velocity error depending on the propagation angle, giving rise to a change in the group velocity and affecting the power transfer rate and direction.

Another important factor affecting the accuracy of the results is the resolution or ability to detect separated waves. Nyquist Sampling Theorem states that at least two points per cycle are needed to prevent aliasing resolving a sinusoidal wave [39]. This imposes limits on the maximum distance between nodes for a certain wave number

$$\Re(k_x) \leq \frac{\pi}{2h_x}, \quad \Re(k_y) \leq \frac{\pi}{2h_y}, \quad \Re(k_z) \leq \frac{\pi}{2h_z} \quad (5.8)$$

Solutions outside the box enclosed by these limits are not distinguishable from lower frequency analogs (waves whose wavelengths are multiples of the shorter one) and, therefore, are not treatable by the numerical method. *Wave-explorer* presents surfaces inside this folding box [37]. For practical matters, a larger number of nodes per wavelength is desired, according to Taflové [45] about 20 nodes are needed for accurate results in FDTD simulations.

Analytic surfaces are figures of revolution around the magnetic field vector as long as the medium remains homogeneous. This is not the case for numerical surfaces which suffer from grid orientation anisotropy. The FD method described in Chapter 4.1 can account for 3D propagation despite strictly being a 2D method. This can be done by means of a harmonic expansion in the z-direction. *Wave-explorer* was initially developed to study 3D codes and it allows to select the plane of propagation for plotting the normal surfaces. Out of mesh-plane propagation is, however, out of the scope of this section.

5.3.1 Vacuum: Grid Anisotropy

Some interesting conclusion are readily available observing the vacuum wave normal surfaces in Figure 5.3. As it was explained in Chapter 3, the normal surfaces (modes) for a wave propagating through vacuum are two circumferences of radius unity when represented in a non-dimensional wave number plot ($\mathbf{n} = \mathbf{k}c/\omega$). Consequently, it becomes obvious that spurious solutions are present in the Sofd3 scheme besides the physical modes. Conversely, Sofd5 seems to map properly the analytic propagation.

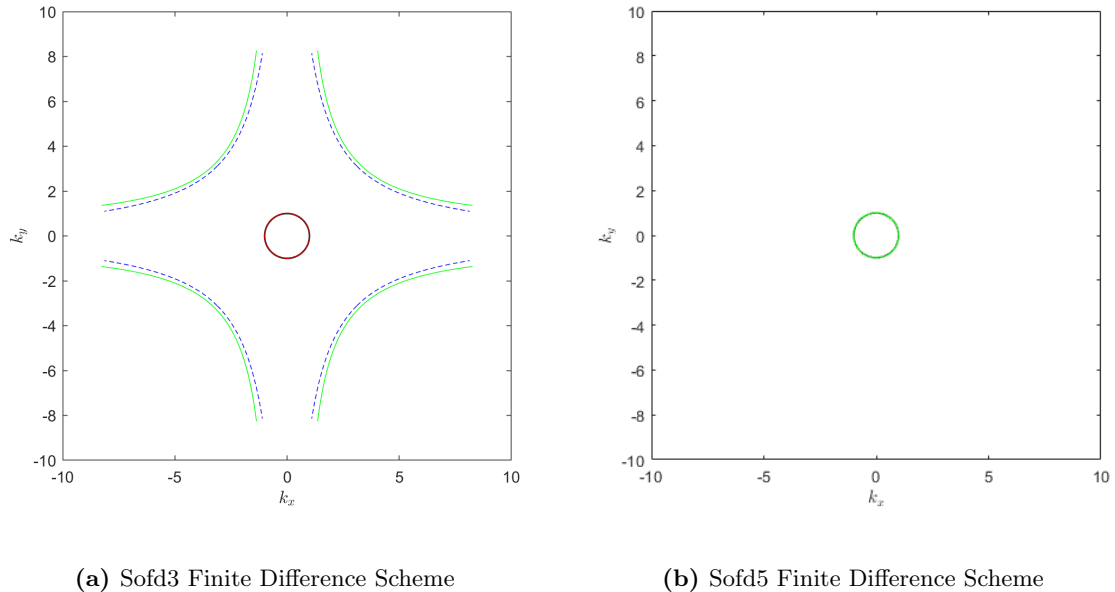


Figure 5.3: Vacuum numerical wave normal surfaces of the finite difference schemes Sofd3 and Sofd5 with $h = 0.2c/\omega$ and uniform stencils. Continuous line representing the real part of the refractive index. Discontinuous line representing the imaginary part of the refractive index. Different colors for different branches.

For both schemes, the perfect analytic surfaces are recovered in the limit $h \rightarrow 0$, this proves the consistency of the schemes. The spurious branches move to even higher frequencies and the physical solution approaches even better the unitary circle as the cell size diminishes. Specially near the plasma resonances, large n solutions may appear¹⁴. This implies that the selection of a small cell size grid (at a higher computational cost) is critical to avoid spurious solutions. This kind of diagram could be very useful for choosing the right settings on those cases.

Coming back to the spurious branches, we observe both real and imaginary branches corresponding to regimes of wave propagation and evanescence. Stix [44] shows that a wave number may only change from purely real to purely imaginary when going through a resonance. This is strictly true only for vacuum and collisionless plasmas where damping is not present. The same behavior has been observe for the numerical vacuum solutions. The branches are either real or imaginary but not any other complex number.

Non-physical or spurious solutions of the Maxwell's Equations in numerical methods have been studied in the literature [34]. For frequency domain finite difference methods and FDTD, the non-physical behavior is related to the divergence-free character of the electric displacement vector $\mathbf{D} = \bar{\kappa} \cdot \mathbf{E}$. Free static charges do not exist in vacuum unless specifically modeled, therefore $\rho = 0$ in all space, from the first of the Maxwell's equations $\nabla \cdot \mathbf{D} = \rho = 0$. Which, for the homogeneous curl-curl equation, is equivalent to $\nabla \cdot (\nabla \times \nabla \times \mathbf{E}) = 0$.

¹⁴In the plots k is non dimensional denoting the refractive index previously called n

It can be shown that this condition is only satisfied by certain schemes such as Sofd5 [37]. For other schemes, like Sofd3, the effect observed is a distortion caused by charge density non-physical equivalents. This is believed to be the cause of the spurious branches in Figure 5.3. In the paper by Merino [37] these are labeled as spurious solutions of the first kind. It is also shown that they can be related to trigonometric factors affecting the dispersion relation in the scheme equations. For Sofd5 there is some scaling error but the topology of the normal surface is not fundamentally altered.

Because the direction of the static magnetic field does not affect the vacuum dielectric tensor and, thus, it neither affects the wave propagation through vacuum, vacuum is the best setup to study the error difference due to the grid orientation. For a plasma this study becomes troublesome as the magnetic field also plays an important role. As it was already stated, grid anisotropy is an important contribution to group velocity error and numerical diffusion.

We know that the wave number solution to the analytic dispersion relation is equal regardless of the direction i.e. the modes lie in two concentric spheres of radius unity. Note that this is not necessarily the case for a general cold plasma.

The anisotropy of numerical surfaces depending on the grid orientation becomes evident looking at Figure 5.3a. The spurious solutions for Sofd3 are asymptotic and disappear for directions parallel to the grid aligned directions. Additionally, in Figure 5.4 a coarser cell size is used and Sofd3 spurious solutions are not shown. The Sofd5 solution is clearly not circular exhibiting peaks at the grid aligned directions.

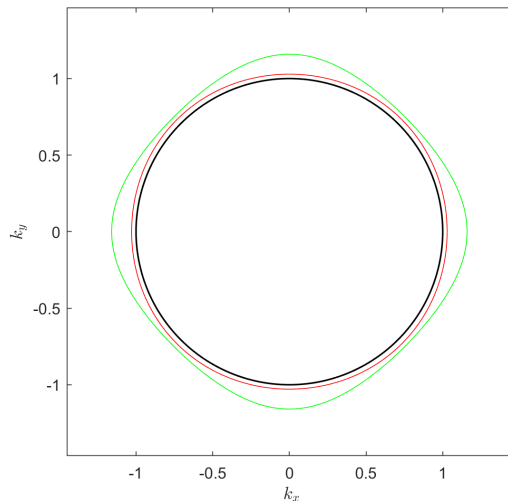


Figure 5.4: Zoom at the Analytic (Black), Sofd3 scheme (Red) and Sofd5 scheme (Green) normal surfaces with $h = 0.8c/\omega$ and uniform stencils. Continuous line representing the real part of the refractive index. Discontinuous line representing the imaginary part of the refractive index.

Above observations, especially for the spurious solutions of sof3, lead to think that numerical diffusion is produced in the cross derivatives of the finite differences schemes. For propagation in the grid align directions, where the cross derivatives are null, the solutions seem to be equal and only numerical dispersion is observed.

5.3.2 Magnetize Collisionless plasma: Static Magnetic Field Anisotropy

A cold plasma with electron cyclotron frequency equal to $\Omega_{ce} = 2\omega$ and plasma frequency equal to $\omega_{pe} = 1.5\omega$ and with negligible particle collisions affecting the dielectric tensor $\nu_m = 0$ was chosen. For this relatively high frequencies, it is possible to neglect the ion motion following the considerations in Chapter 3. Hence, the ion cyclotron frequency is approximately null $\Omega_{ci} \approx 0$, the same applies for the plasma frequency $\omega_{pi} \approx 0$. Here ω is the excitation frequency as usual.

Looking at the CMA diagram, Figure 3.3 in Chapter 3, the plasma parameters above proposed lie on region 7 as labeled by Stix [44]. The R wave of this configuration is representative of both Helicon and Electron Cyclotron Resonance thrusters although they may operate in region 8-8b where the L or fast wave does not propagate.

The analytic topology in Figure 5.5 is inverse to the one in the CMA diagram as expected. Also notice that the magnetic field is directed along the x-axis this time. The central oval like shape corresponds to the L wave. In accordance with the theory presented in Chapter 3, no propagation of the outer R wave is possible perpendicular to the magnetic field. On the other hand there is an asymptotic resonance cone centered along the magnetic field direction.

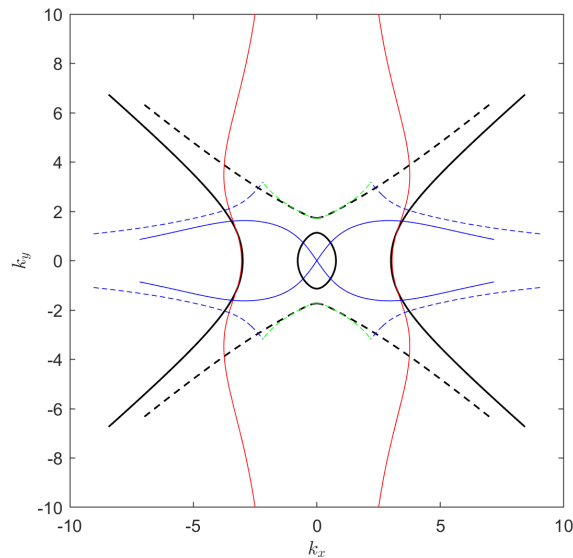


Figure 5.5: Numerical wave normal surfaces for Sofd3 FD scheme with $\omega_{pe} = 1.5\omega$ and $\omega_{ce} = 2\omega$. Node distance $h = 0.2c/\omega$ and uniform stencil. Discontinuous line representing the imaginary part of the refractive index. Different colors for different branches.

Figure 5.6 illustrates the effect of approaching Electron Cyclotron Resonance modeled by SOfd5. Spurious solutions have been eliminated from this plot. The electron cyclotron frequency was changed to $\Omega_{pe} = 1.05\omega$ to get close to the resonance $\Omega_{pe} = 1\omega$. The propagating wave solution branch has moved toward higher spatial frequencies. It is easy to realize that a finer cell size is needed both to properly resolve the wave (Nyquist condition) and to avoid non-physical solutions.

Coming back to Figure 5.5 for the study of Sofd3 scheme surfaces for the collisionless plasma, the first noticeable feature is the presence of an spurious solution near the resonance cone (in blue). It is particularly interesting to recognize the complex components of this branch. We notice that it has both real and imaginary components. Consequently, this solution must be dissipative or grow unbounded spatially in contrast to the either propagating or evanescent branches nearby. This is a clearly non-physical behavior because there is not any mechanism explaining energy dissipation (which can only be caused by collisions) within the current configuration.

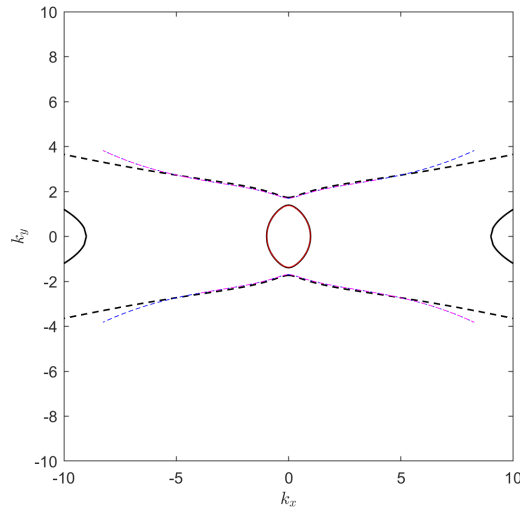
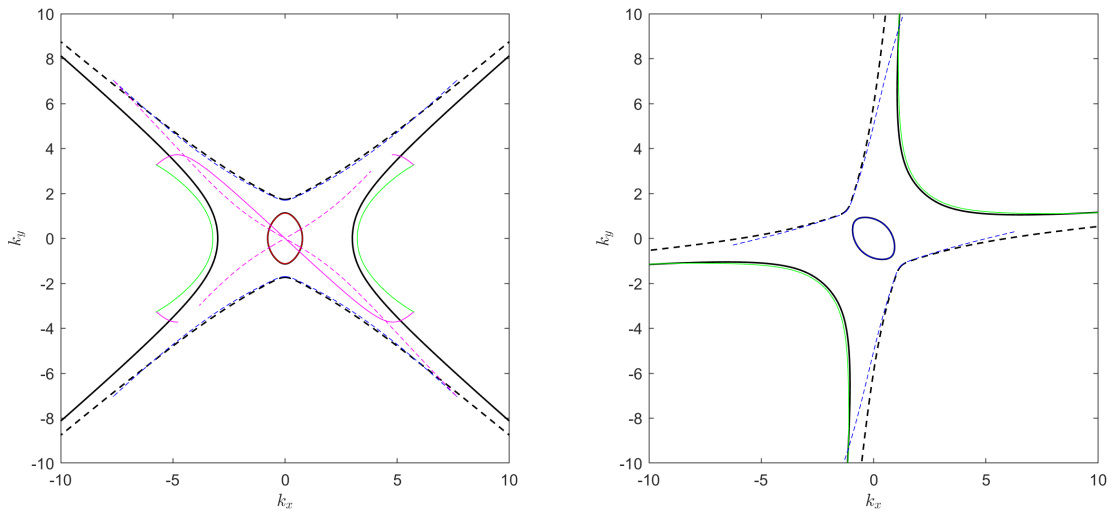


Figure 5.6: Numerical wave normal surfaces for Sofd5 FD scheme with $\omega_{pe} = 1.05\omega$ and $\omega_{ce} = 2\omega$. Node distance $h = 0.2c/\omega$ and uniform stencil. Continuous line representing the real part of the refractive index. Discontinuous line representing the imaginary part of the refractive index. Different colors for different branches.



(a) Sofd5 Finite Difference Scheme $\mathbf{B}_0 \parallel \mathbf{1}_x$

(b) Sofd5 Finite Difference Scheme \mathbf{B}_0 at 45 deg $\mathbf{1}_x$

Figure 5.7: Numerical wave normal surfaces for Sofd5 FD scheme with $\omega_{pe} = 1.5\omega$ and $\omega_{ce} = 2\omega$ at different static magnetic field \mathbf{B}_0 angles. Node distance $h = 0.2c/\omega$ and uniform stencil. No collisions. Continuous line representing the real part of the refractive index. Discontinuous line representing the imaginary part of the refractive index. Different colors for different branches.

Exploring now the dispersion relation solutions in the divergence-free scheme Sofd5 (Figure 5.7), spurious surfaces are also found (magenta lines). These appear near the resonance cone and are termed Spurious Solutions of the Second Kind. These solutions are also complex and, because damping has not been introduced, they lack any physical explanation. In addition to the grid orientation solution dependence, here we also observed the anisotropic behavior with respect to the static magnetic field. The spurious solution comprises two branches following the resonance cone asymptotes when the

static magnetic field is align with either one of the principal stencil directions. When a small angular deviation is imposed, one of the branches disappears. Interestingly, the spurious solutions completely vanish at 45 deg [37] (Figure 5.7b).

5.3.3 Collisional plasma: Damping

In Chapter 3 it was mentioned that particle collisions act as a damping element within the plasma. The damping mechanism is the absorption of energy inside the plasma by thermal randomization of the motion of charge particles through collisions with other particles such as Coulomb collisions. When it comes to wave propagation, this feature is observed as an attenuation of the wave amplitude. This fact is observe in the dispersion relation solution because the refractive index becomes complex i.e. it has both real and imaginary part (pure imaginary solutions do not propagate). Damping is observed in Figure 5.8, for any propagation direction, any normal surface has an imaginary part.

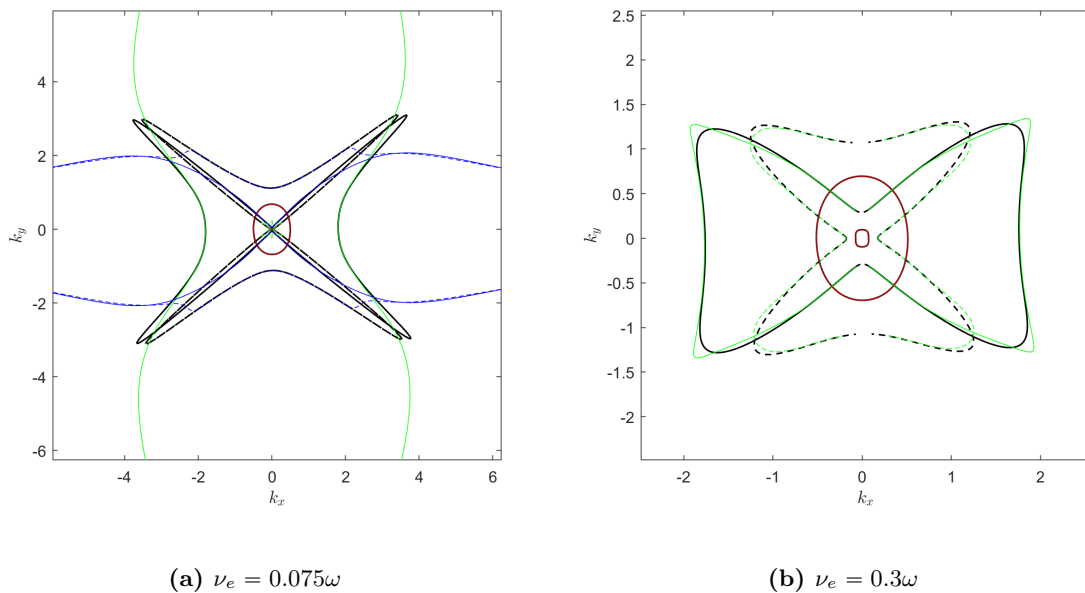


Figure 5.8: Numerical wave normal surfaces for Sofd3 FD scheme with $\omega_{pe} = 1.5\omega$ and $\omega_{ce} = 2\omega$ with different collision frequencies. Magnetic field align with x-axis. Node distance $h = 0.2c/\omega$ and uniform stencil. Continuous line representing the real part of the refractive index. Discontinuous line representing the imaginary part of the refractive index. Different colors for different branches.

Keeping the node distance constant, we can observe the role of collisions as a factor enhancing convergence. The spurious solution (blue) disappears from the folding box when the collision frequency is increased. Also the physical solutions (specially the green branch) attach much better to the analytic surfaces. Collisions also reshape the analytic topology. In figure 5.8a, the ECR (green) resonance cone is really sharp and the refractive index has a large value near the asymptotes. There is also very little damping in the propagation directions inside the cone (there is a small imaginary part looking closer towards the center of the figure). Conversely, the propagation of the R wave (green) is almost negligible perpendicular to the field. Similarly, the fast wave L (red) has very high damping in every propagation direction.

5.4 Non-uniform grid wave normal surfaces

Based on the original *wave-explorer* code, the algorithm was modified to include non-uniform grids. The specific details on the computation of the scheme coefficients from the stencil geometry are explained in Section 8.1. Notice that the flow chart (Figure 5.2) differs slightly but the general continuation of solutions method remains similar.

A more detailed study of the normal surfaces for cold plasma under non-uniform stencils is proposed as future work. However, interesting features are readily observable just looking at the vacuum propagation. Figure 5.9 shows both a sample arbitrary stencil and the resulting normal surfaces.

The plot focuses on the interior circle containing the analytic modes. New surfaces appear inside the circumference. These numerical modes are specially relevant for Sofd5 (red) and small for Sofd3 (green). It is observed that, reducing the global cell size, the spurious solutions shrink toward the center becoming undetectable at moderate cell sizes and proving the consistency of the method. The amount of deformation of the stencil accounts also a significant parameter determining the non-physical behavior.

The spurious surfaces displayed in Figure 5.9 have imaginary refractive indexes. From this fact it is infer that non-uniform grids could induce numerical **wave dissipation**.

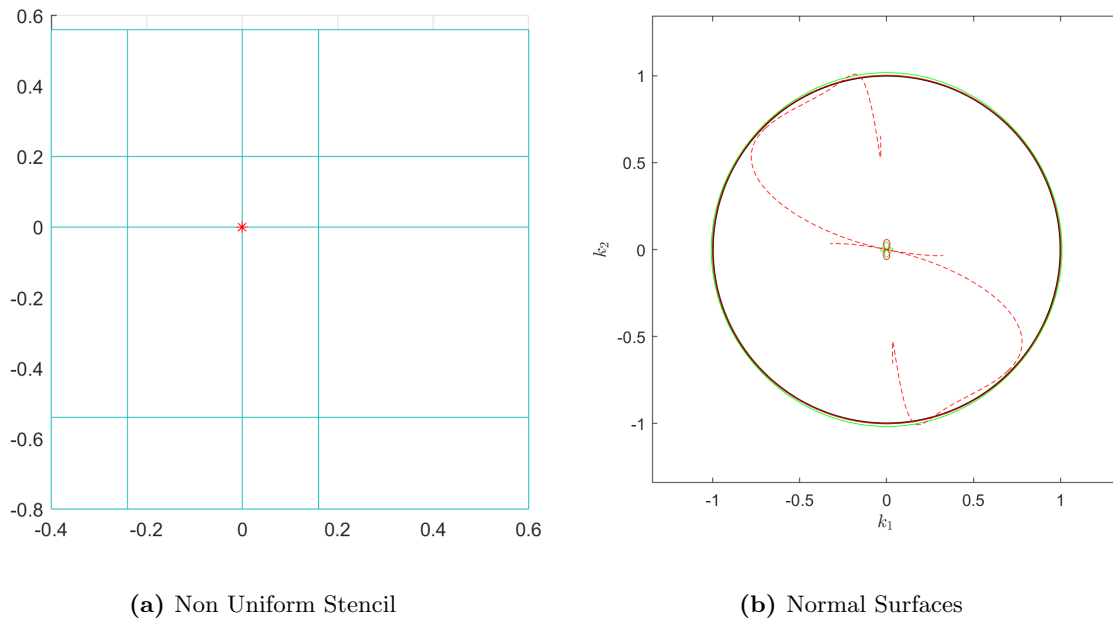


Figure 5.9: Non Uniform Stencil Vacuum Numerical Wave Normal Surfaces, red (Sofd3) and green (Sofd3). Continuous line representing the real part of the refraction index. Discontinuous line representing the imaginary part of the refractive index.

6 Simulation software: *fdwaves*

In order to discretize space in a mesh of nodes, implement the scheme equations and boundary conditions and solve the arising linear system of equations, a numerical code was implemented using in Matlab. In addition to those basic functionalities, this code also includes a preprocessor to treat raw input data and a postprocessor for an easy interpretation of the results. Figure 6.1 shows a schematic flow chart of *fdwaves*.

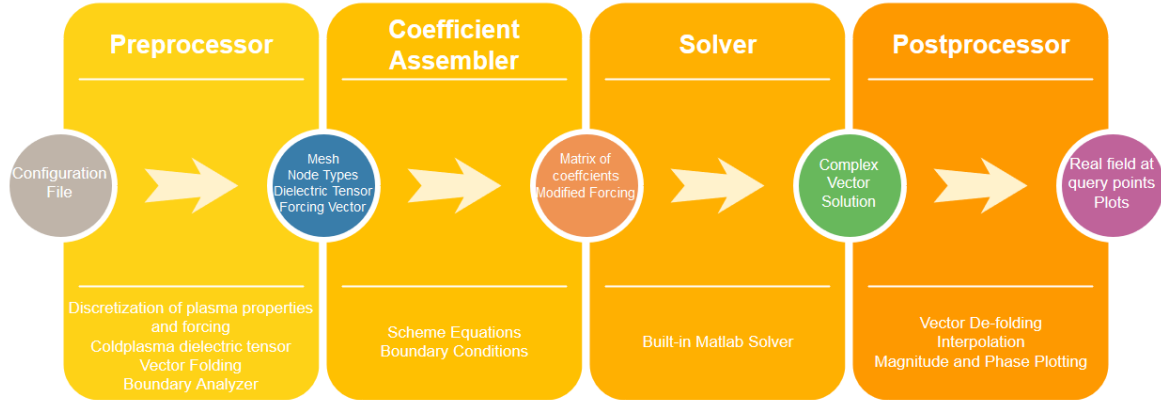


Figure 6.1: *fdwaves* code Flow Chart

6.1 Preprocessor

The first step for the simulation of the electromagnetic problem is to preprocess the configuration inputs provided by the user, *fdwaves* admits the setup options given in an input file, if no file is provided, default options would be used. Additionally, it might be interesting to change some of the file configurations keeping the rest unmodified. For this task, the user can overwrite certain fields in the input file externally. For instance, this is useful for parametric studies where only some problem specifications change from a simulation to the following one. Figure 6.2 shows the operations driven by the preprocessor function. The inputs completely closing the electromagnetic problem and, thus, determining the numerical solution field in all the domain are:

1. Plasma parameters: Space functions for the static magnetic field vector and the ion and electron densities and collisional frequencies.
2. Boundary conditions: PEC nodes and outer periodic conditions in any direction.
3. Mesh: Currently working with Cartesian uniform meshes. The mesh maps the computational domain or nodes coordinates (i,j) with the real node position in the physical domain.
4. Current Density: Spatial vector function for the forcing current density in each direction.
5. Wave parameters: Excitation frequency ω and harmonic z-direction spatial frequency k_z .

In order to model a cold plasma, the dielectric tensor of Equation 3.39 must be obtained in all the points of the domain. Although no results are presented for a non-uniform plasma, *fdwaves* is prepared to handle that kind of simulation. To accomplish this task, once a mesh is provided, the plasma properties given as spatial functions are discretized into each of the mesh nodes. The same applies to the magnetic field. The tensor for a node is build according to the electromagnetic theory presented in chapter 3 and then stored in memory for the implementation into the scheme equations. Cartesian coordinates are used to write the tensor and throughout the whole operation of *fdwaves*.

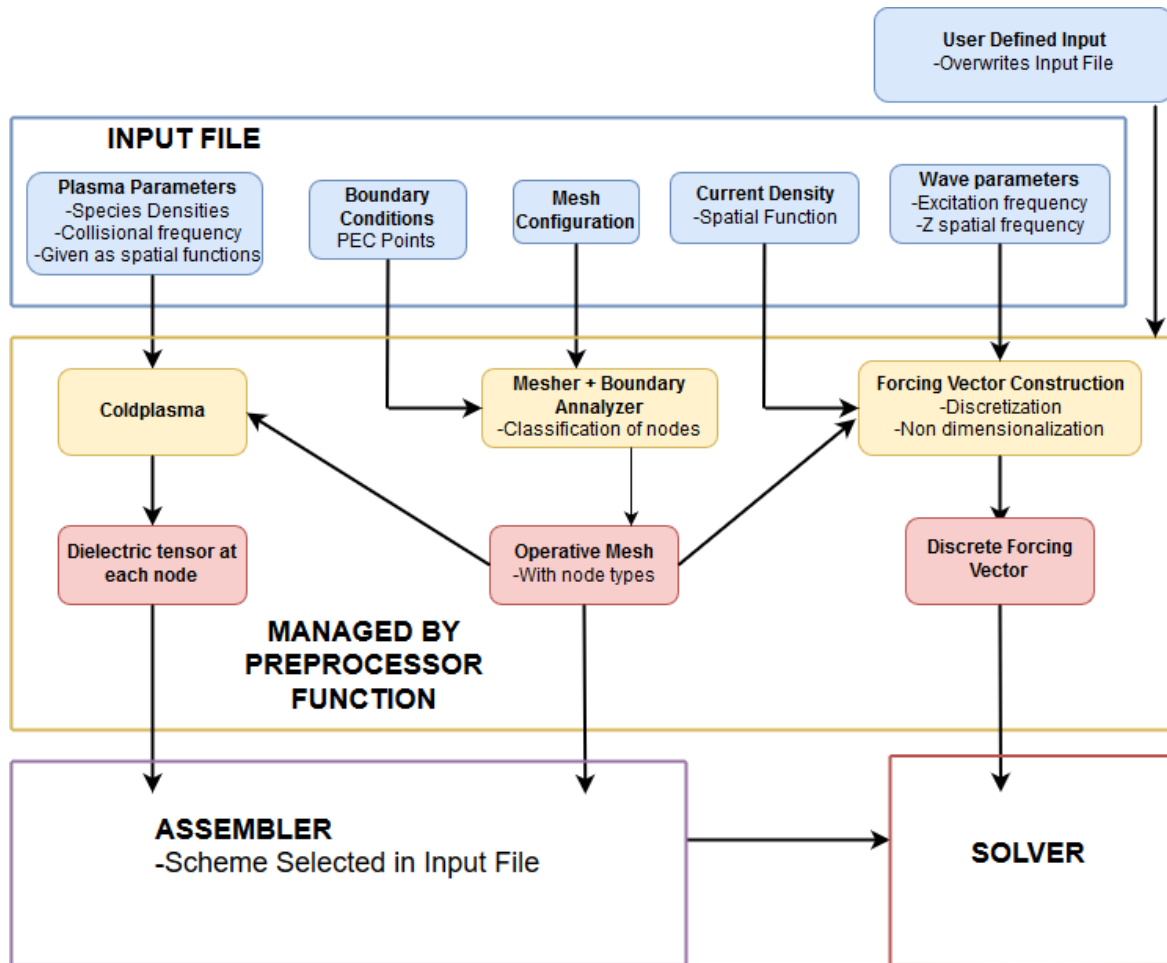


Figure 6.2: Preprocessor package Flow Chart

6.1.1 Mesh and Node Classification

The discretization of space is critical for the attainment of accurate results, the mesh (collection of points) selection is based on two factors:

- The proper mapping of the problem geometry: *fdwaves* is capable of simulating straight PEC walls and corners in addition to periodic conditions on the boundaries. Complex PEC geometries can be modeled using the so called ‘Staircase approximation’[45]. This technique is widely used in Finite Difference codes to represent geometric features by combining walls and corners. However, the accuracy of this approach is relatively poor. To solve this problem a complex geometry mesher using interpolation is proposed in Chapter 8.
- The internal mesh precision: This has to do with the node separation and alignment which, in the most general case, determine the total error of the simulation by respectively setting h and n in the residual of the finite difference approximations $O(h^n)$. Currently, *fdwaves* only uses Cartesian meshes so alignment is not a concern as, adversely, it is for unstructured meshes. The role of the node separation h was observed in the normal surfaces of Chapter 5 as a key factor for the appearance of spurious solutions and the error in the physical branches. There might be regions where more precision is sought due to geometry or the presence of shorter wavelengths. Consequently, non-uniform meshes can help keeping the overall number of nodes within an admissible range while providing more precision in critical areas of the domain. Chapter 8 proposes a possible solution with the new *fdmesher* tool.

As long as the mesh remains structured, the real coordinates of each node can be stored in matrices whose indexes (i,j) correspond to the computational coordinates denoting those nodes (these are integer numbers extending from 1 to m or n, being m and n the total number of nodes in each direction). Notice that, this kind of mesh could be deformed from a Cartesian topology whilst keeping its structure. For unstructured meshes, it is convenient to use vectors with dimensions equal to the number of nodes (degrees of freedom) for each of the physical coordinates. In the case of *fdwaves*, the Cartesian mesh is readily assembled using the built-in MATLAB function *meshgrid*.

For the sake of modeling internal geometric features, the PEC nodes should be classified as upper, lower, left and right walls in addition to corners because different forward FD approximations are used in each of them. Also the so called ‘neighbor’ nodes should be identified when the central scheme is Sofd5, in these nodes, centered Sofd3 is applied to prevent the use of out-of-domain nodes due to the larger computational cell.

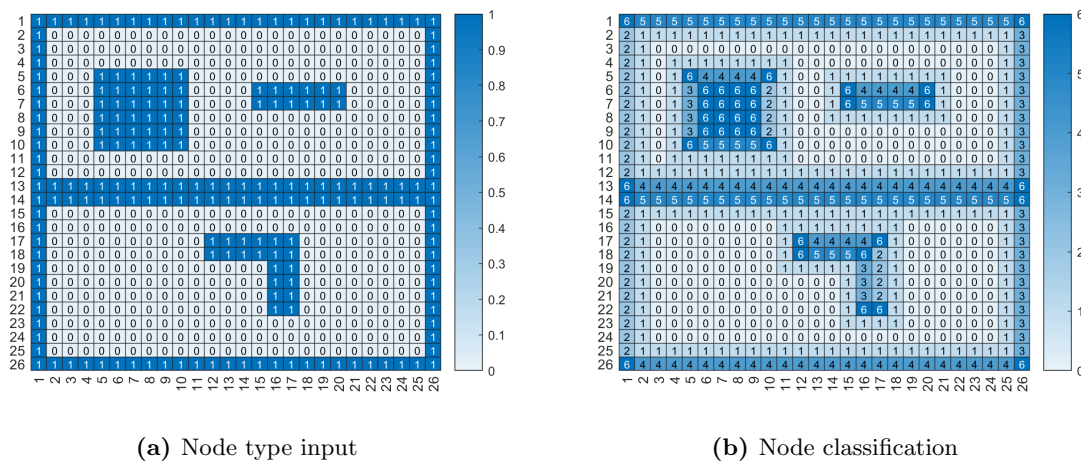


Figure 6.3: Node classification from boundary type input. 0 → Center Node, 1 → Neighbor Node, 2 → Right Wall, 3 → Left Wall, 4 → Upper Wall, 5 → Lower Wall, 6 → Corner

The objective of the node classifier function is to convert a user input, only telling which nodes are PEC, to an operational set of different node types. This code also checks whether there are non-physical configurations like single PEC nodes inside the domain and displays a warning whenever this happens. Following this procedure, the coefficient assembler can apply the proper equation in each node. If any of the outer walls is left without PEC conditions, periodicity is assumed in that directions and the circular call to the nodes explained in Chapter 4.2 is utilized. Figure 6.3 shows the transformation from the user input to the classified nodes, this is done by means of vectorized logical operations to increase performance.

6.1.2 Forcing terms: Sofd5 Grid Uncoupling

When Sofd5 scheme was tested with discrete perpendicular antennas (along the z-direction) a strong field jump was observed from one node to the nearby one. This behavior is thought to be caused by the grid uncoupling between the second and first or cross derivatives in the computational cell. The nature of the uncoupling is better understood considering 1D propagation along one of the principal directions. It might be observed that only second derivatives exist with this setup. Taking, for instance, an even node, due to the computational cell used by Sofd5 with alternating nodes for the second order derivatives, the FD approximations would apply coefficients to the nearby even nodes. On the other hand, odd nodes would only be connected to other odd nodes. As a result, we would be solving two different problems for even and odd nodes.

Although, difficult to show in a simple manner, a similar behavior is expected for 2D propagation.

Depending on the forcing term positioning, the two superimposed grids might have different field values. It is also possible that plasma induced some soft grid coupling alleviating this issue.

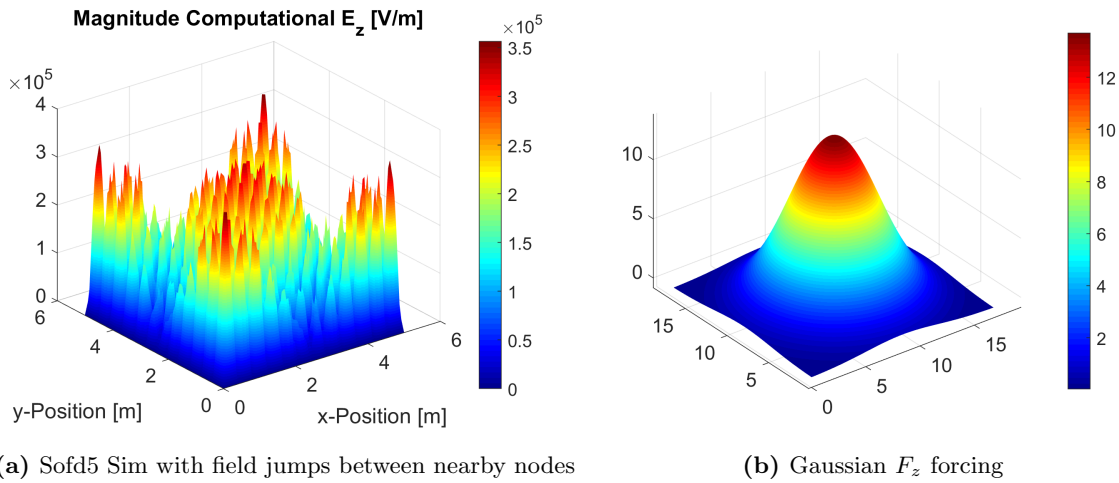


Figure 6.4: Sofd5 uncoupling issue and Gaussian Forcing model of a perpendicular antenna. In a real simulation the function is sharper around the central excitation node.

A solution was found in order to simulate perpendicular z-directed antennas without Sofd5 uncoupling. If, instead of a discrete single node current density, a smooth function is used as the forcing term, the undesired behavior shown in Figure 6.4.(a) is prevented. A suitable option for the representation of discrete antennas is the utilization of a Gaussian 2D function centered around the antenna position such as the one shown in Figure 6.4.(b) but much sharper for correctly mapping a thin wire. In order to correctly model an electric current, it is possible to integrate the value of this function (current density) on the whole domain and scale the amplitude to match the desired current.

6.2 Coefficient Assembler and Solver

	$\mathcal{E}_x^{1,1}$	$\mathcal{E}_y^{1,1}$	$\mathcal{E}_z^{1,1}$...	$\mathcal{E}_x^{1,n}$	$\mathcal{E}_y^{1,n}$	$\mathcal{E}_z^{1,n}$...	$\mathcal{E}_z^{m,n}$
$eqn_x^{1,1}$									
$eqn_y^{1,1}$									
$eqn_z^{1,1}$				⋮					
⋮			...	$\bar{M}[\mathcal{E}_{c_u}^{i_u, j_u}, eqn_{d_e}^{i_e, j_e}]$...				
$eqn_z^{m,n}$				⋮					

Table 4: Arrangement of coefficients in \bar{M} . Where i_u, j_u, c_u denote the node computational coordinates and the Cartesian component (x, y, z) of the unknown or degree of freedom. Similarly, i_e, j_e, d_e are used for the equation in a node defined by the coordinates (i_e, j_e) and in the direction established by $d_e \equiv (x, y, z)$.

In Chapter 5, the scheme equations and boundary conditions were presented, nevertheless, it was not explained how the coefficients appearing in the equations are collected and arranged before being introduced in the solver. This needs to be done due to the fact that linear system solvers work with the usual matrix of coefficients multiplied by the vector of unknowns nomenclature. Table 4 shows the particular configuration used in *fdwaves*, the rows correspond to equations and the degrees of freedom are placed in different columns. Specific details about the code will not be provided because there are other equally valid methods to accomplish the same results.

As a summary, the equations are applied according to the pre-classified node types and keeping the consistent index arrangement described in Table 4. For this task, vector-matrix wrapping and

unwrapping functions are used because it is easier to work with the electric field solution in matrix form (with i and j node coordinates) to write the scheme equations and for post-processing and plotting. The same applies to the forcing matrix which is unwrapped to vector form prior to solving. The coefficient matrix uses an special data type called ‘sparse matrix’ to save memory. Sparse arrays only store the non-zero elements in memory so they are appropriate for FD methods where the matrix of coefficients has zero value for almost all its entries. Having found the matrix of coefficients and the forcing term vector, a built-in Matlab solver is used.

Once the electric field is known in the whole domain, Faraday’s Law of Induction 3.2 can be used to compute the Magnetic flux density or induction vector \mathbf{B} , normally simply referred as magnetic field. After Fourier expansion in space, we have

$$\nabla \times \hat{\mathbf{E}} = -\frac{\partial \hat{\mathbf{B}}}{\partial t} \quad (6.1)$$

$$\mathbf{B}(\mathbf{r}, t) = \Re[\hat{\mathbf{B}}(\mathbf{r}, \omega) \exp(-i\omega t)] \quad (6.2)$$

$$\nabla \times \hat{\mathbf{E}} = i\omega \hat{\mathbf{B}} \quad (6.3)$$

Equation 6.3 can be discretized by finite differences in each node of the domain. Solving for the magnetic field, with $\mathcal{B}^{i,j}$ denoting the discrete value of the field in a node, we obtain

$$\mathcal{B}_x^{i,j} = -\frac{i}{\omega} \left(\frac{\mathcal{E}_z^{i,j+1} - \mathcal{E}_z^{i,j-1}}{2h_y} - ik_z \mathcal{E}_y^{i,j} \right) \quad (6.4)$$

$$\mathcal{B}_y^{i,j} = -\frac{i}{\omega} \left(ik_z \mathcal{E}_x^{i,j} - \frac{\mathcal{E}_z^{i+1,j} - \mathcal{E}_z^{i-1,j}}{2h_x} \right) \quad (6.5)$$

$$\mathcal{B}_z^{i,j} = -\frac{i}{\omega} \left(\frac{\mathcal{E}_y^{i+1,j} - \mathcal{E}_y^{i-1,j}}{2h_x} - \frac{\mathcal{E}_x^{i,j+1} - \mathcal{E}_x^{i,j-1}}{2h_y} \right) \quad (6.6)$$

This is the wave magnetic field not to be mistaken for the static background magnetic field which is usually several orders of magnitude stronger. Normally the wave magnetic field is just neglected, nonetheless, we have proven its derivation. Figure 6.6 shows the components of the electric and magnetic field for an arbitrary simulation. For completeness, a complex geometry consisting of a domain with perfectly electric conductor walls and another internal PEC box was chosen. Figure 6.5 shows the boundary conditions and forcing setup, the field is excited with two perpendicular antennas at different phases and with different currents.

An interesting fact to be noticed is that there are not E_x , E_y nor B_z fields in the vacuum simulation. This corresponds to the Transverse Magnetic Mode (TM_z) polarization. It can be shown that the equations for the three excited fields are completely decoupled from the other three equations when the derivatives in the z -direction are null. On the other hand, plasma induced currents produce a complete coupling of all 6 fields as shown in Figure 6.7.

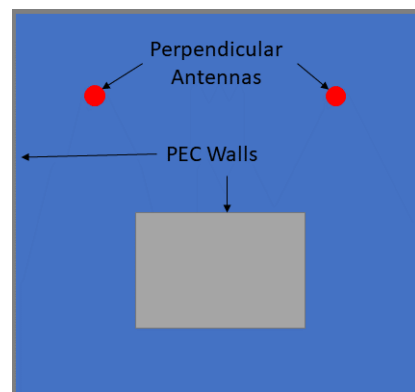


Figure 6.5: Simulation domain layout for the tests

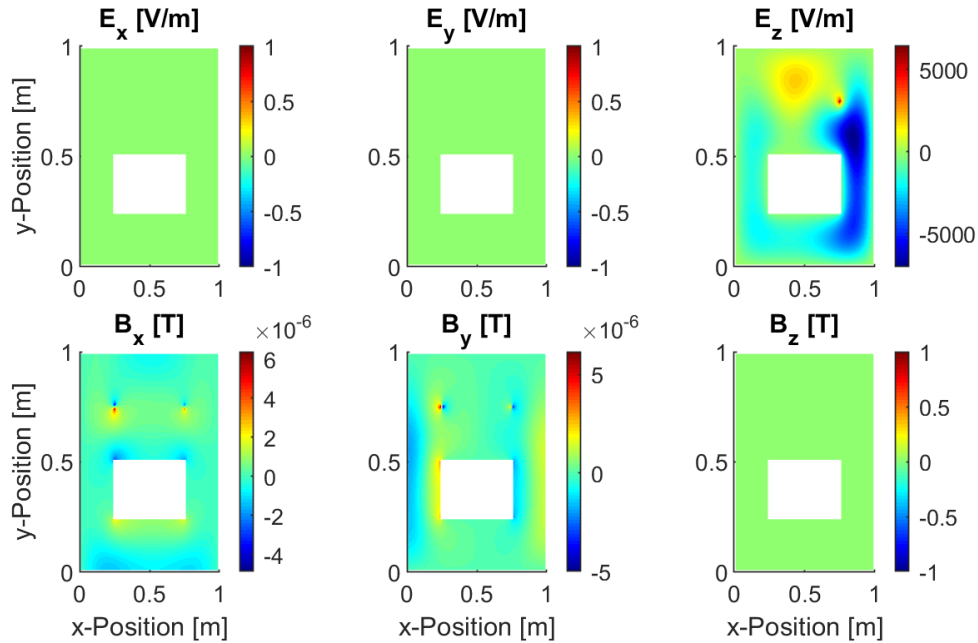


Figure 6.6: Complete set of solution fields of an electromagnetic problem. Simulation with $k_z = 0$, field shown at $z = 2m$ and $t = 7.5s$. Vacuum. Cartesian mesh with 401×401 nodes

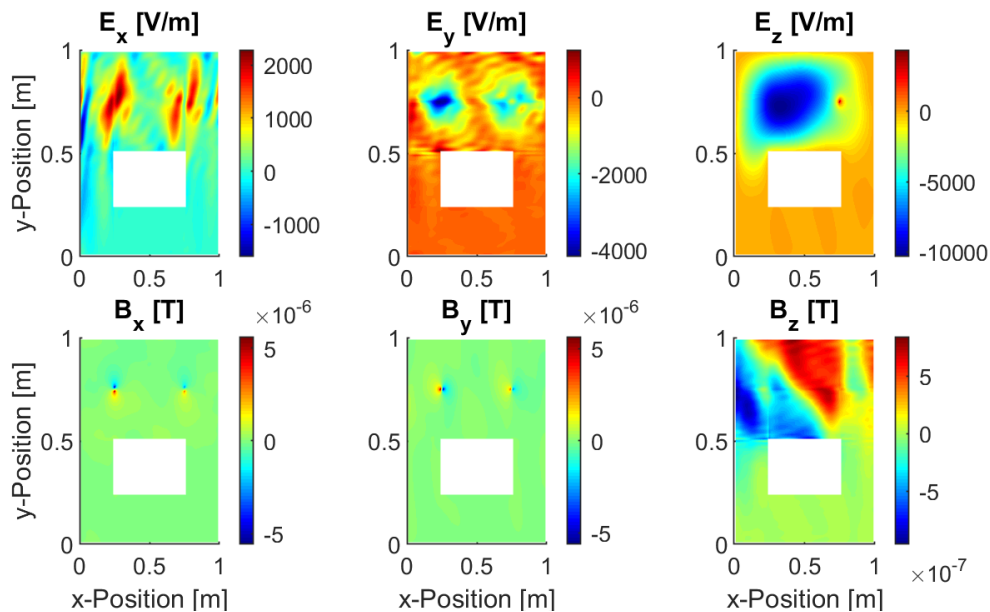


Figure 6.7: Complete set of solution fields of an electromagnetic problem. Simulation with $k_z = 0$, field shown at $z = 2m$ and $t = 7.5s$. Plasma parameters $\omega_{pe} = 1.5\omega$, $\Omega_{ce} = 2\omega$, $\nu_m = 0.5\omega$. Excitation angular frequency $\omega = 3.3301 \times 10^9 rad$. Cartesian mesh with 401×401 nodes

The fields shown above are the real fields at a given instant and z position. Nonetheless, it might be more useful to represent the magnitude and phase of each of those fields. Such plots completely define the solution fields and can be time and z expanded using the harmonic exponential terms. Moreover, for simulations like the one shown in Figure 6.6 it might be enough to represent the E_z field norm and phase because this is a decoupled mode with no other electric field components, the magnetic components can be later obtained from this unique field. For a TE_z mode we could as well represent the magnetic field in the z -direction and disregard all other fields. This kind of techniques are useful to obtain straightforward field visualizations that would, otherwise, be complicated if one had to pay attention to all 6 fields' magnitudes and phases.

6.3 Computational Performance and Limitations

For the sake of studying the performance of *fdwaves*, several simulations were performed with an increasing number of nodes. The field in different domain locations is checked against a most precise simulation which is, as a first approximation, assumed to be error-less when compared with coarser simulations. Then, the residual relative mean error is plotted. This procedure is used for convergence tests in a later section where it will be explained in detailed. Figure 6.8 shows the consistency of the method with the error going to 0 for an infinite number of nodes.

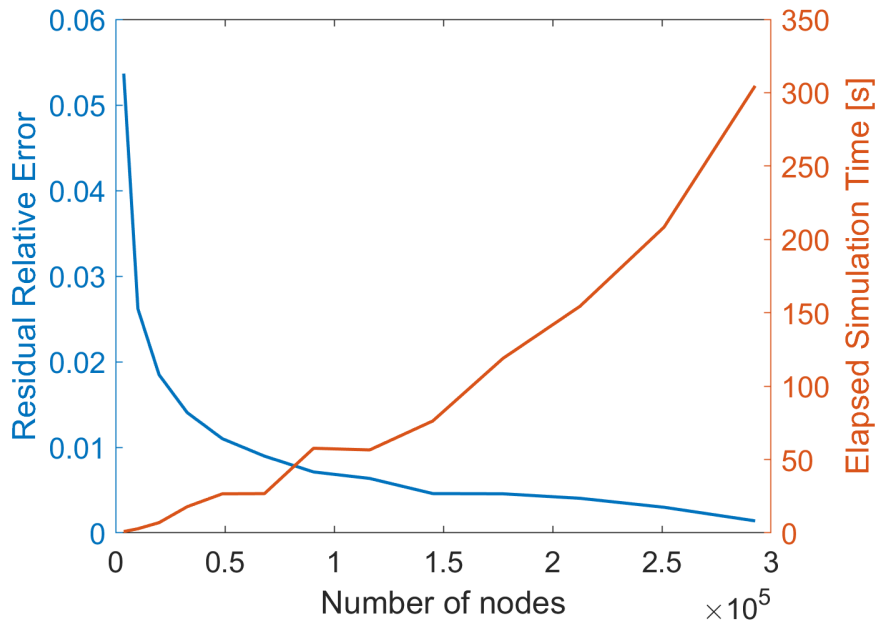


Figure 6.8: Residual error between interactions and elapsed time as a function of the number of nodes. Simulation with $k_z = 0$. Plasma parameters $\omega_{pe} = 1.5\omega$, $\Omega_{ce} = 2\omega$, $\nu_m = 0.2\omega$. Excitation angular frequency $f = 1.5GHz$

Besides the error, the elapsed time for each simulation is also shown. Notice that this figure is unique to the hardware and software used. Nonetheless, the shape of the time function is, in principle, determined by the algorithm. An almost linear dependence on the number of nodes is observed. This behavior is desirable because the error decreases faster than the increase in the simulation time.

However, there is a very important limitation that breaks the trend shown in Figure 6.8. The linear solver currently used (Matlab built-in) uses a considerable amount of computer internal memory. When the 16GB available with the system used to carry out the simulations are used up, Matlab starts working with a much slower hard disk allocation. This, in practice, means that the simulation is unsuccessful (we would probably have to wait for hours instead of a few minutes). The programming of *fdwaves* was done efficiency-oriented, with several vectorized functions and special data types

(sparse matrices). On the other hand, the solver used is meant to be versatile and multipurpose to solve any system of linear equations without focusing on the specific characteristics of the problem (symmetry, matrix type...).

In order to solve this inconvenience, the utilization of other solvers is under study. This might include some compile code in a lower level and more efficient language such as FORTRAN or C.

Profile Summary
Generated 20-Sep-2018 22:27:07 using performance time.

Function Name	Calls	Total Time	Self Time*	
bar_solv	1	23.607 s	23.607 s	Solver
coeff	1	13.747 s	8.888 s	Assembler
sofd3	159201	4.265 s	4.265 s	Scheme Equations
lsq	643204	3.978 s	3.978 s	Preprocessor Functions
permat	1	7.507 s	3.391 s	
coldplasma	160801	2.925 s	2.925 s	
jacob	1	6.480 s	2.502 s	Preprocessor Functions
preprocessor	1	17.757 s	1.387 s	
lin2vect	1	1.711 s	1.261 s	Postprocessor Functions
magnetic	1	1.149 s	1.149 s	

Other Functions
≈ 10 s
↓

Figure 6.9: Elapsed time in *fdwaves* functions. Plasma Simulation with 401×401 nodes.

Figure 6.9 shows a summary of the elapsed time in the most important *fdwaves* functions. The solver takes more than half the time. If the number of nodes is further increased, the portion of the total time used by the solver is even larger. Other main contributions are the matrix assembler and the preprocessor although this functions are not memory critical and, hence, do not represent a serious issue.

6.4 Finite difference method accuracy: Analytic Solutions

This section is devoted to finding simple analytic solutions that can be compared against the numerical output, hence, providing a means of verification for the numerical method. As shown in Chapter 3, the wave equation after Fourier analysis in time and space is

$$\left[\begin{pmatrix} -k_y^2 - k_z^2 & k_x k_y & k_x k_z \\ k_x k_y & -k_x^2 - k_z^2 & k_y k_z \\ k_x k_z & k_y k_z & -k_x^2 - k_y^2 \end{pmatrix} + \frac{\omega^2}{c^2} \begin{pmatrix} \kappa_{xx} & \kappa_{xy} & \kappa_{xz} \\ \kappa_{yx} & \kappa_{yy} & \kappa_{yz} \\ \kappa_{zx} & \kappa_{zy} & \kappa_{zz} \end{pmatrix} \right] \begin{pmatrix} \tilde{E}_x \\ \tilde{E}_y \\ \tilde{E}_z \end{pmatrix} = -i\omega\mu_0 \begin{pmatrix} \tilde{J}_x \\ \tilde{J}_y \\ \tilde{J}_z \end{pmatrix} \quad (6.7)$$

In order to be able to reproduce the wave in the numerical method, the wavenumber must comply with the available boundary conditions. For instance, to obtain a periodic wave, an integer number of wavelengths should appear in the domain i.e. the wavenumbers must obey

$$k_x = \frac{2\pi n_x}{L_x}; \quad k_y = \frac{2\pi n_y}{L_y} \quad (6.8)$$

Where $\{n_x, n_y\} \in \mathbb{Z}$ and L_x and L_y are the dimensions of the domain box. An appropriate yet simple selection of the problem parameters would be $l = m = 1$ with $L_x = L_y = 2\pi$. This gives $k_x = k_y = 1$. It is also possible to select a vacuum permittivity tensor $\bar{\kappa} = \epsilon_0 \bar{\mathbf{I}}$. Besides, $\omega = c$ and $k_z = 0$ are arbitrary values chosen, once more, for the sake of simplicity. The wave equation becomes

$$\begin{pmatrix} 0 & 1 & 0 \\ 1 & 0 & 0 \\ 0 & 0 & -1 \end{pmatrix} \begin{pmatrix} \tilde{E}_x \\ \tilde{E}_y \\ \tilde{E}_z \end{pmatrix} = -i\omega\mu_0 \begin{pmatrix} \tilde{J}_x \\ \tilde{J}_y \\ \tilde{J}_z \end{pmatrix} = \begin{pmatrix} \tilde{f}_x \\ \tilde{f}_y \\ \tilde{f}_z \end{pmatrix} \quad (6.9)$$

Where $\tilde{\mathbf{f}}$ is just a compact form forcing term with no particular physical meaning. Afterwards, an arbitrary value for the electric field complex amplitudes $\tilde{\mathbf{E}}$ is chosen. Applying Equation 6.9, after inversion of the accompanying matrix, the corresponding forcing term complex amplitudes are found. Then it is possible to expand the terms using the coordinates x,y of each of the nodes in the domain

$$\hat{\mathbf{E}} = \tilde{\mathbf{E}} \exp[i(x \cdot k_x + y \cdot k_y)] \quad (6.10)$$

$$\hat{\mathbf{f}} = \tilde{\mathbf{f}} \exp[i(x \cdot k_x + y \cdot k_y)] \quad (6.11)$$

Finally, $\hat{\mathbf{f}}$ is a new forcing term that can be fed into *fdwaves* to find the numerical field solution. Periodic conditions must also be selected. We also have the analytic field solution in all space provided by $\hat{\mathbf{E}}$. Now it is very easy to measure the error of the simulation by just averaging the difference between the analytic and numerical solution in all the nodes or just taking the value at the node with the maximum error. An error plot in the problem domain can also be obtained. Additionally, to make the error assessment simple, we can excite a unique field component in Equation 6.9, for example, $\tilde{\mathbf{E}} = [1, 0, 0]$. The error can be checked in magnitude or phase of the complex $\hat{\mathbf{E}}$ or in terms of a real field at a time and z-position, any of these options avoids using complex amplitudes (difficult to plot).

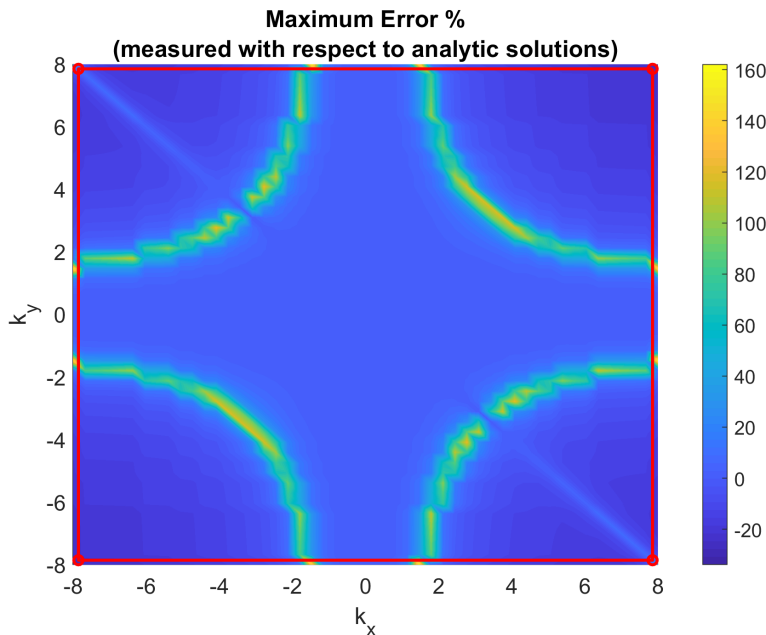


Figure 6.10: Maximum error in the field norm. Sofd3 scheme in vacuum, periodic conditions $\bar{h}_x = \bar{h}_y = 0.2$. 2500 simulations with different \bar{k}_x and \bar{k}_y . Configurations inside the Nyquist sampling box (red line).

Figure 6.10 shows an interesting error profile. The maximum error across all the domain nodes in complex amplitude magnitude (a real number) is represented for 2500 simulations with varying values of k_x and k_y ($k_z = 0$ in all the simulations). All the variables were dimensionless (we selected $\omega/c = 1$) and the number of nodes was automatically varied to obtain a predefined node distance \bar{h}_x and \bar{h}_y while complying with the periodic boundary conditions (integer wavelengths per domain). The error

is shown as the percentage deviation from the analytic field. Negative values mean that the numerical field magnitude is smaller than the analytic one.

Looking at the shape of the error in k -parametric space in Figure 6.10, it can be observed that this figure resembles Figure 5.3 in Chapter 5. This surprising coincidence shows the power of wave normal surfaces to evaluate schemes. However, although the relation might seem crystal clear, we are facing two completely different problems and the explanation to this behavior is more complex and subtle than initially expected.

It might be observed that the error remains within acceptable bounds for low k s. When the parameters get close to the spurious solution in Figure 5.3, the numerical field magnitude becomes much greater than the analytic one. This is a distinguishable characteristic of resonance despite the fact that this resonance is purely numerical and lacks any physical meaning. As k is increased, the numerical field rapidly decays and becomes much smaller than the analytic one, indeed, it is less than 1% of the analytic field. Additionally, the high wavenumber numerical solution is completely out of phase (π rad difference) with the analytic solution, this is shown in Figure 6.11.

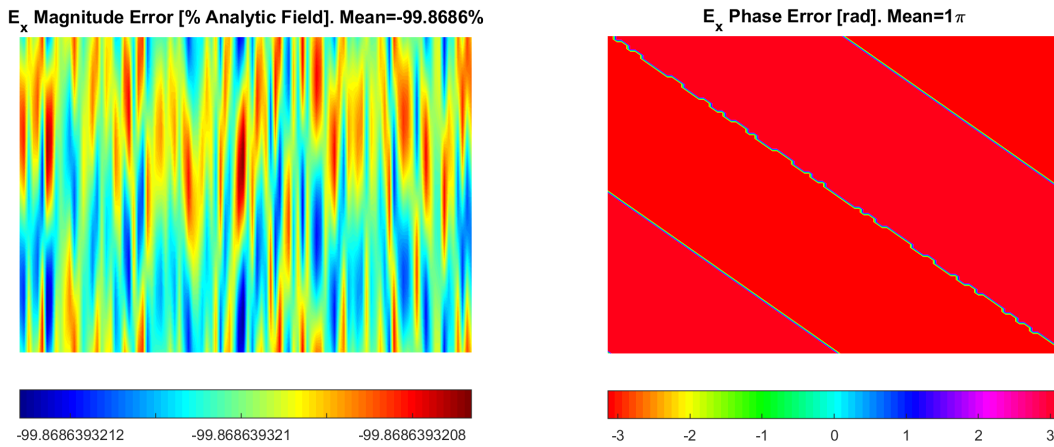


Figure 6.11: Numerical Field Norm and Phase Error $\bar{h}_x = \bar{h}_y = 0.1$. Analytic periodic wave with $\bar{k}_x = k_x \times c/\omega = 20$ and $\bar{k}_y = 10$

A suitable explanation is the divergence of numerical eigenvalues from the analytic ones. We know that any spurious solution corresponds to a zero eigenvalue for the system in a single node, recall that the determinant of the matrix of local coefficients is equaled to 0 in order to obtain the numerical branches in Chapter 5. Due to the fact that the same computational cell is kept throughout the whole domain, a single configuration produces zero eigenvalues in the propagation throughout all the nodes. This means that, regardless of the excitation, at least one natural mode will go to infinity. After going through 0 (i.e. resonance), the eigenvalue would change sign, explaining the π rad phase error in the higher k simulations. Afterwards, the eigenvalue seems to grow very fast making the numerical field go to 0.

The only reason to obtain an error in the simulations so similar to the spurious solution is the use of the same computational cell with the same node spacing in all the domain. Non-uniform meshes may produce other kind of error profiles in the parametric space resulting from the interaction of the errors in different computational cells.

6.5 Finite difference method accuracy: Convergence

Chapter 5 showed the consistency of the schemes. As the computational cell size diminishes, the spurious solutions shrink or go out of the Nyquist box (resolution limit) and the physical solutions

detach later from the analytic surface. This behavior can also be observed in full size simulations. Convergence plots are a suitable tool to demonstrate the validity of a solution without using simple analytic solutions. The consistency illustrated in the normal surfaces is key as it shows that simulations with increasingly finer meshes cannot converge to a spurious solution.

Consequently, we can plot the residual error, this is the field norm difference between a certain simulation and the most precise simulation available. If we observe that the residual goes to 0 we can state that the solution is spurious free i.e. the only possible convergence is to the physical solution. This also stands for boundary conditions where consistent lower order approximations were locally used.

The problem setup described in Figure 6.5 is used to check convergence including the two out of phase perpendicular antennas. Two different frequencies are used throughout the simulations. It was checked that they are not particularly close to any resonance. The simulations include 17 different meshes with the same number of nodes in x and y directions (from 21×21 to 321×321), the reference configuration for the residual was 341×341 .

The error assessment method consisted in finding the values of the electric field norm in 100 random points of the domain (the solution is interpolated) and computing the relative difference with the most precise simulation (341×341). The relative residual averaging all 100 query points is then plotted. Selecting a large number of query points reduces bias due to their random positioning. Notice that the forcing term introduces residual error itself because the antennas are thinner when the number of nodes increases. However, the current density is adjusted in each iteration to model an infinitely thin antenna with certain current. Due to the high current density when many nodes are used, the field is not evaluated for error assessment near the antennas, this restricts the position of the random query points.

It was decided to exclusively study Sofd3 scheme convergence, recall that Sofd5 does not admit discrete antennas. Plasma simulations using Sofd5 have shown similar convergence for continuous distributions of current density, however, the results presented in Chapter 7 were obtained using Sofd3, as a consequence, it is essential to test the accuracy of this scheme. Future work might target convergence of other schemes (not only Sofd5 but higher order methods and non-uniform meshes).

6.5.1 Vacuum Convergence

Inspecting Figure 6.12, it can observe that the solution greatly degenerates at microwave range frequencies as expected. As already stated, this undesirable behavior is caused by the spurious branches shown in Figure 5.3. The residual errors are tremendously high at $f = 2.95GHz$ in contrast with the smooth curve going asymptotically to 0 at $f = 295MHz$. The simulation is not feasible with the number of nodes proposed. Due to the high memory used by the implicit linear solver, accurate vacuum results are very difficult to obtain at mid-low microwave frequencies.

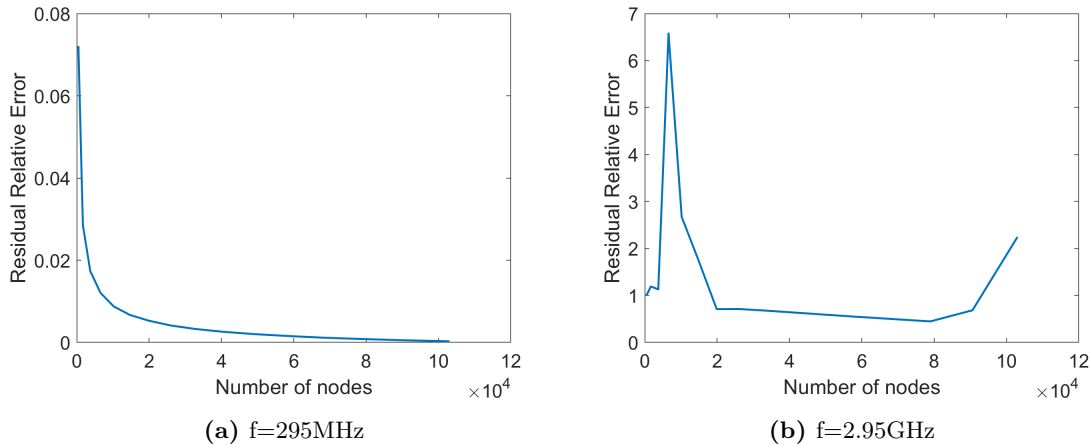


Figure 6.12: Vacuum Convergence Plots.

Nonetheless, Figure 6.13 shows a surprising feature of collisional plasma that could overcome this inconvenience.

6.5.2 Plasma Convergence

Coldplasma simulations representative of Helicon and ECR regimes were setup with characteristic plasma and electron cyclotron frequencies ($\omega_p = 1.5\omega$, $\omega_p = 2\omega$). The electron collision frequency is varied from high values ($\nu_e = 0.2$) to a merely collisionless plasma.

The main conclusion after inspection these plots is that collisions enhance convergence. This fact already arouse in Chapter 5 when the normal surfaces were plot. However, the fact that plasma simulations outperform the simpler vacuum ones is remarkable. Of course the evolution of the plots as the collisionality is lowered is coherent in Figure 6.13. As predicted, the collisionless solution does not converge. This is not only due to the spurious solutions but mainly caused by the resonant cone where the wavenumber goes to infinity and the method is unable to resolve the shorter waves lengths.

This demonstrate that it is possible to obtain accurate results for the wave propagation in a cold plasma with a moderate number of nodes less than $5 \cdot 10^5$. Collisionality is not only the mechanism of energy deposition inside the plasma (the objective in electric thrusters) but it also helps to ease the numerical computations.

Convergence plots changing the magnetic field direction are shown in Figure 6.14 for the same plasma. The orientation of the field with respect to the grid seems to only affect the absolute value of the residual, specially, at 45 deg with respect to the grid. On the other hand, convergence is conserved.

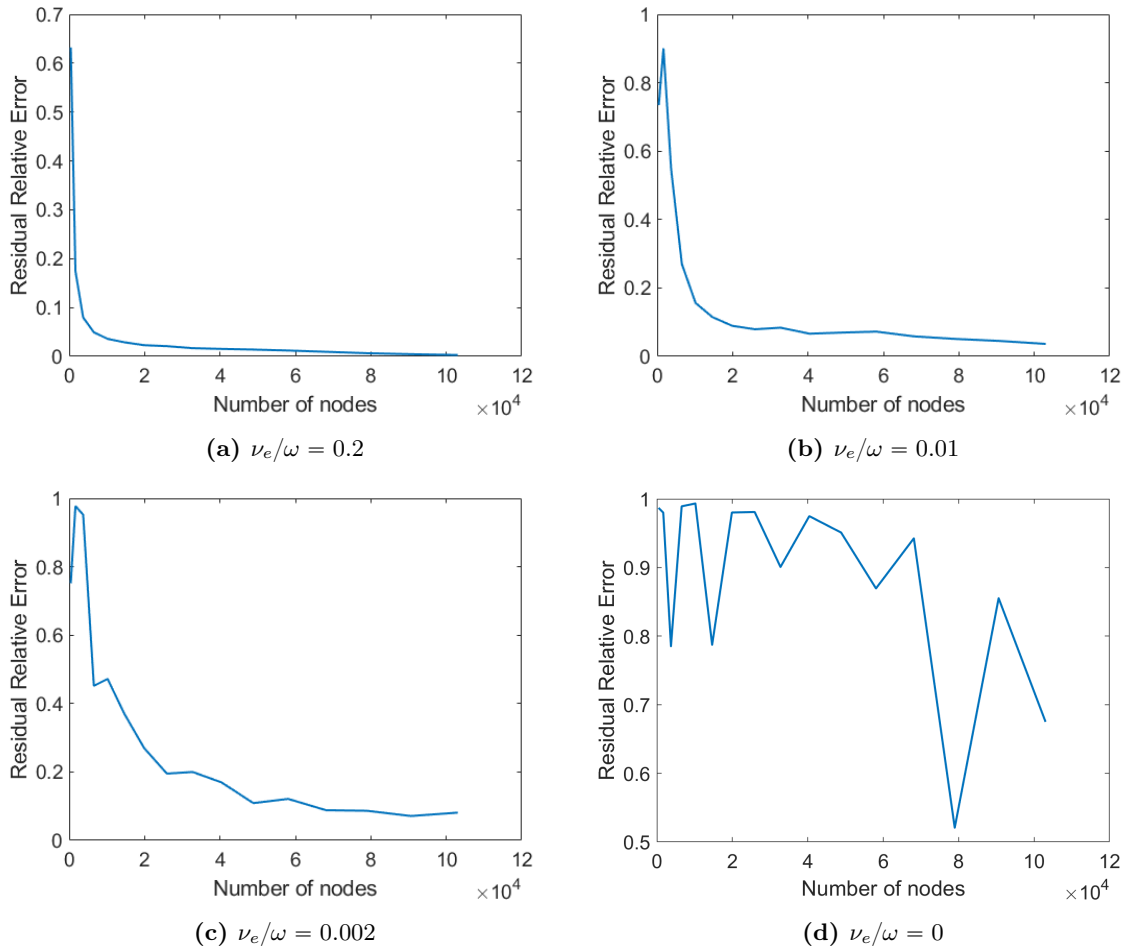


Figure 6.13: Plasma Convergence Plots at $f=2.95\text{GHz}$. Cold plasma with parameters $\Omega_{ce} = 2\omega$, $\omega_p = 1.5\omega$. Ions assume static due to low mobility. Electron collisionality indicated in each plot. Magnetic field aligned with x-axis.

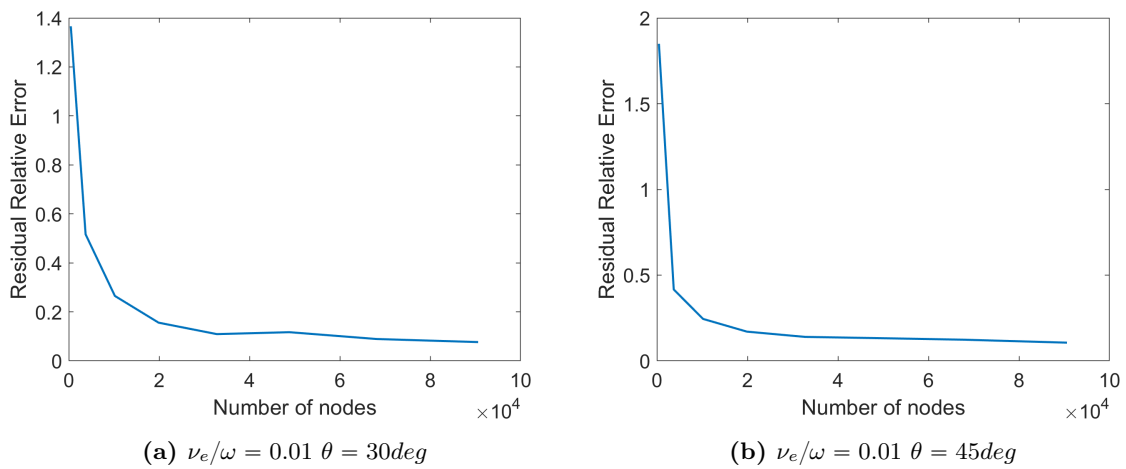


Figure 6.14: Plasma Convergence Plots at $f=2.95\text{GHz}$. Not aligned background magnetic field, θ denotes the angle with the x-axis. Cold plasma with parameters $\Omega_e = 2\omega$, $\omega_p = 1.5\omega$. Ions assume static due to low mobility. Electron collisionality indicated in each plot.

6.5.3 Z-Harmonic Field Convergence

The results when periodicity in z-direction is considered are rather imprecise (see Figure 6.15). This should be further studied as the mechanism of spurious solution formation and physical solution detachment are not well understood. Recall that the normal surfaces have been constrained to the propagation plane contained within the mesh.

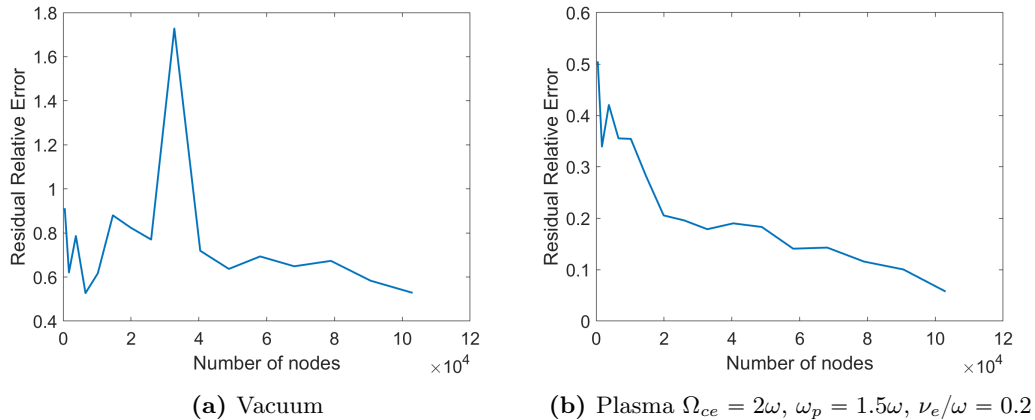


Figure 6.15: Convergence Plots with propagation in z-direction, $k_z = 1.3$, $f=295\text{MHz}$.

Even at a low frequency, the simulations struggle to converge. Moreover, the vacuum plot is not unambiguously convergent. This is an important feature to be researched in the future as it could compromise the results of axisymmetric codes. The relative residuals are very high even with a significantly large number of nodes. As usual, plasma collisions seem to help reaching convergence.

6.5.4 In-plane dipole antenna convergence

It was observed that the error is significantly greater when in-plane dipole antennas are used. The problem is specially remarkable for vacuum propagation where accurate solutions are only obtainable at very low frequencies (under 100MHz). A suitable explanation is that spurious modes are mainly in-plane electric polarizations (E_x and E_y components). This should be the matter of future study. As usual plasma collisions enhance convergence.

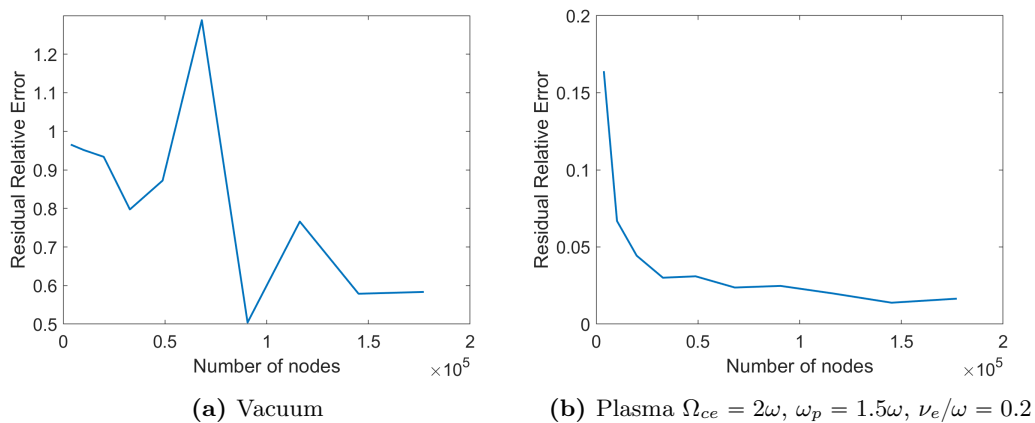


Figure 6.16: Convergence Plots with a central dipole antenna, $f=2.95\text{GHz}$. The simulation has been extended to a larger number of nodes.

6.5.5 Order of the simulation from convergence plot

In a 2 dimensional simulation, the total number of nodes is inversely proportional to the square of the node distance. On the other hand, we know that the truncation error can be written as $(\Delta err) \propto \Delta h^n$, where Δerr is the residual error and n is the FD order. Consequently, and assuming that the most precise simulation is, approximately, error-less, it should be possible to infer the order from the convergence plots. The function should follow $(\Delta e) \propto N^{-0.5n}$, with N denoting the total number of nodes.

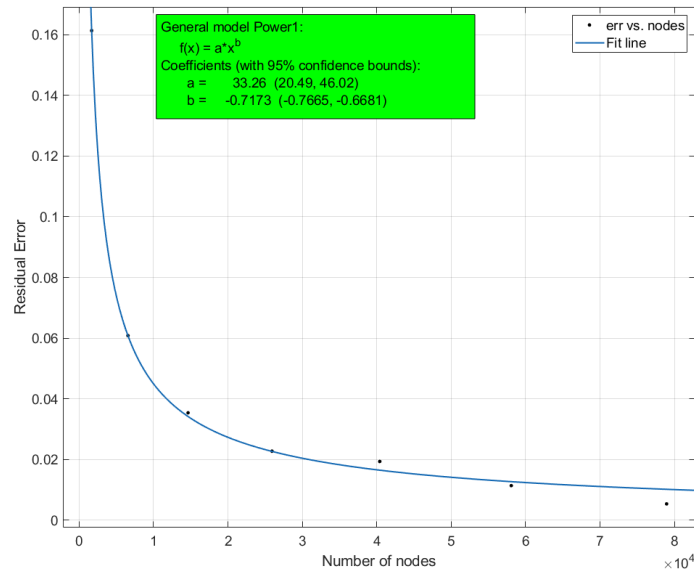


Figure 6.17: Power fit to the err vs. nodes convergence plot of an arbitrary plasma simulation.

Using a power model to fit the data in a convergence test with the parameters of Figure 6.8 (a general plasma simulation), we find an exponent ~ -0.7 , corresponding to an order of simulation of about ~ 1.4 . The value was expected to lie between the order of the forward difference approximations in the boundaries i.e. $n = 1$ and the central domain higher order approximations $n = 2$. It was observed that, from one simulation to another, the overall order could change significantly but was always in this range $1 \rightarrow 2$. Non-uniform meshes are necessary to give a higher node density at the boundaries and overcome this issue (See Section 8.1).

7 Analysis of solutions

The aim of this section is to provide some numerical results of the finite difference code *fdwaves*. Unlike chapter 5, this results come from a full simulation including boundary conditions. In section 8.6 absorbing conditions, in particular PMLs, are proposed for future work. This tool is fundamental to avoid reflections in an exhaustive study of ECR thrusters shown in Figure 7.1. Unfortunately this part of the code was not yet available at the time this thesis was written.

Despite this inconvenience, many significant wave propagation features can be observed with other boundary conditions. Specially interesting is the wave behavior inside a perfectly conducting cavity or resonator (note that periodic conditions are also available). This kind of study is also useful as it allows to set easy simulations for comparison with other codes and, thus, it is a good verification procedure.

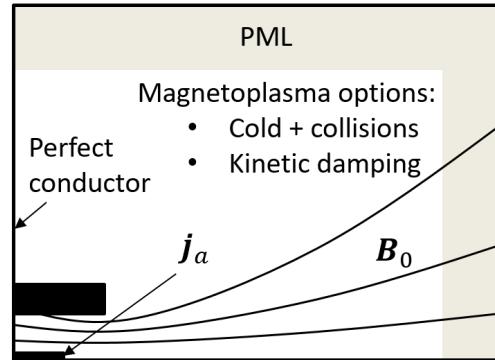


Figure 7.1: ECR domain for the full simulation objective [37]

7.1 Eigenfrequencies of a resonant cavity (PEC)

Plane waves will be studied by setting infinitely long antennas (current densities) perpendicular to the propagation plane and with zero derivatives in the z -direction i.e. $k_z = 0$. This produces an E_z field propagating in the x,y -plane (E_x and E_y fields are 0 in vacuum). The setup excites the so-called magnetic transverse mode with respect to the z -direction or TM $_z$. The wave magnetic field is always contained in the plane perpendicular to the infinitely expanded direction. In vacuum, the resulting field can be represented just plotting the phase and magnitude of E_z instead of the usual 6 fields. We will take advantage of this fact to achieve straightforward field representations.

The TM $_z$ mode, besides the electric transverse mode TE $_z$, is extensively used in waveguides and lasers. However, note that the following simulations do not try to reproduce a waveguide. The nomenclature used by Taflove[45] referring to a TM $_z$ wave exclusively implies null z -derivatives and only E_z component for the electric field in vacuum. Waveguide polarizations differ slightly in their definition, for instance, there is always propagation in the z -direction, indeed, that is the goal of these devices.

We want to study the lower resonant frequencies in the mid RF to low microwave range ($10^8 - 10^9 Hz$). Resonant cavities working at this frequencies, having wavelengths a few centimeters long, are of enormous importance for a wide range of applications such as signal filtering in microwave circuits, Helicon electric thrusters and radar technologies. At slightly higher frequencies (low GHz) we can find the working regime of microwave ovens (2.45 GHz) and, of course, of ECR thrusters. Those frequencies are readily studied with *fdwaves* code provided a fine enough mesh.

As already stated, Sofd5 scheme has problems resolving waves with discrete current density sources, to avoid those problems Sofd3 will be used. Despite preventing cell uncoupling, Sofd3 exhibits spurious solutions at high frequencies, a behavior that was already expected.

Due to the necessity of avoiding spurious solutions, higher excitation frequencies come at a higher computational cost. Some spurious-free solutions have already been obtained using Sofd3 up to 5 GHz in vacuum but the process is troublesome without a powerful computer (about 750×750 nodes are needed). Consequently, it was decided to work at a little longer wavelengths. The physical phenomena observed is completely equivalent. For the second part of this section, where plasma is introduced, the frequencies are increased to match the ECR working regime. This can be done by

virtue of collisional damping and its ability to dissipate the spurious solutions (see Chapter 5).

Resonance is found in many branches of physics such as mechanics and electromagnetism. The common feature is the vibration of a dynamic system at higher amplitudes for certain excitation frequencies. Without a damping mechanism, resonant peaks would, theoretically, go to infinity. Resonance is often related to positive interference, for instance, in the case of wave propagation, waves reflected on the walls of a metallic cavity can sum up if they arrive at a certain point with the same phase. As the wavelength and the peak phase are related to the excitation frequency, the interference phenomenon will only take place at particular ‘resonant’ frequencies.

It is interesting to explore how resonance arises in the finite difference method. For this task, we are going to present a slightly different method for obtaining the field solution. Recalling the problem formulation in Chapter 4.1, once the coefficient \bar{M} matrix has been found, the numerical problem reduces to solving

$$\bar{M}(\omega) \cdot \mathcal{E}(\omega) = \mathcal{F}(\omega) \quad (7.1)$$

It is important to note that $\mathcal{E}(\omega)$ now denotes a discrete vector containing the field in all the multiple degrees of freedom of the problem (for the three spatial components) and it is not position dependant. After obtaining the eigenvalue-eigenvector pairs of \bar{M} we construct a matrix $\bar{P} = [\mathbf{v}_1, \mathbf{v}_2, \dots, \mathbf{v}_n]$ whose columns are the eigenvectors \mathbf{v}_i and a diagonal matrix whose entries are the corresponding eigenvalues $\bar{D} = \text{diag}(\lambda_i)$. By the definition of eigenvalues and eigenvectors

$$\bar{M}\mathbf{v}_i = \lambda_i\mathbf{v}_i, \quad \bar{M}\bar{P} = \bar{P}\bar{D} \quad (7.2)$$

Given that \bar{M} is invertible, the eigenvectors \mathbf{v}_i (normalized to unity) form an orthonormal basis [40]. Afterwards, we can perform a change of basis to the electric field and forcing term. Notice that the tildes no longer mean a transformation to frequency domain but the vectors in the new basis.

$$\mathcal{E}(\omega) = \bar{P}\tilde{\mathcal{E}}(\omega), \quad \mathcal{F}(\omega) = \bar{P}\tilde{\mathcal{F}}(\omega) \quad (7.3)$$

Upon substitution of Equations 7.3 and 7.2 into Equation 7.1 a solution for the system is found

$$\tilde{\mathcal{E}}(\omega) = \bar{D}^{-1}\tilde{\mathcal{F}}(\omega) \quad (7.4)$$

$$\mathcal{E}(\omega) = \bar{P}\bar{D}^{-1}\bar{P}^{-1}\mathcal{F} \quad (7.5)$$

This diagonalization method is completely analogous to inverting the coefficient matrix. Thanks to the fact that the matrix \bar{D} is diagonal, it is straightforward to inspect the components of the vector $\tilde{\mathcal{E}}$, these are the weights of the natural modes (eigenvectors) determining the solution

$$\tilde{\mathcal{E}}_i = \frac{\tilde{\mathcal{F}}_i}{\lambda_i} \quad (7.6)$$

The linear combination of eigenvectors determines the solution. Straightaway, it becomes clear that resonance appears when one of the eigenvalues becomes 0 i.e. \bar{M} is singular. If that is the case, one of the **eigenmodes** grows indefinitely large regardless of the excitation (unless the excitation

component is also null). Therefore, numerical resonance occurs for excitation frequency values that make \bar{M} non invertible, in other words, when the determinant of the square matrix is null.

It is critical to realize that, although similar in form, this problem has nothing to do with finding the normal surfaces via solving the dispersion relation for a particular computational cell. Matrix \bar{M} contains the coefficients for all the degrees of freedom of the numerical problem, includes the boundary conditions and, once a forcing term is selected, determines the field response. Whereas, numerical normal surfaces only give the propagation through a single computational cell. However, it could be compared to the solving of the analytic dispersion for an uniform infinite medium after time and space Fourier expansions, providing the whole solution field for simple enough boundary conditions.

7.1.1 Vacuum Resonant Modes in a Rectangular Cavity

Inasmuch as the problem remains simple in terms of boundary conditions and geometry, it turns out that analytic solutions for the resonant frequencies can be found. For an uniform and isotropic media, in a rectangular perfect electric conductor (PEC) cavity where waves propagate in TEz or TMz modes; the following expression relates the domain dimensions (L_x and L_y), the number of waves inside the cavity in each direction ($\{m_x, m_y\} \in \mathbb{Z}$ where $m=1$ implies half wavelength) and the resonant frequency f_{m_x, m_y} .

$$f_{m_x, m_y} = \frac{c}{2\sqrt{\mu_r \epsilon_r}} \sqrt{\left(\frac{m_x}{L_x}\right)^2 + \left(\frac{m_y}{L_y}\right)^2} \quad (7.7)$$

There are infinite analytic resonant modes with increasing frequency. To see the process followed to obtain the above expression refer to the book on microwave engineering by Collin[17]. The same result arises taking the determinant of the analytic propagation matrix relation in Chapter 6 if PEC complying forcing terms were introduced instead of periodic ones. We will set a one square meter square domain ($L_x = L_y = 1m$) and study the arising patterns from 0 to 4 waves in each direction. Of course, for vacuum, the relative permittivity and permeability equal 1. The results are shown in Table 5.

Eigenfrequencies in 100MHz					
$m_x \backslash m_y$	0	1	2	3	4
0	0	1.5000	3.0000	4.5000	6.0000
1	1.5000	2.1213	3.3541	4.7434	6.1847
2	3.0000	3.3541	4.2426	5.4083	6.7082
3	4.5000	4.7434	5.4083	6.3640	7.5000
4	6.0000	6.1847	6.7082	7.5000	8.4853

Table 5: Resonant Frequencies of a cavity with dimensions $L_x = 1m$ and $L_y = 1m$ in vacuum

Now that the analytic resonant frequencies are available, there is a very good test consisting on comparing those frequencies with the numerical resonant modes from the finite difference method. Looking at the scheme equations in section 4.2 it turns out that, as long as the dielectric tensor is diagonal at all points in space, (this implies the presence of homogeneous isotropic media) we may rewrite the coefficient matrix as

$$\bar{M} = \bar{C} - \epsilon_r \frac{\omega^2}{c^2} \bar{I} \quad (7.8)$$

Where \bar{C} is a new matrix containing, exclusively, the coefficients of the finite differences discretized derivatives. To find the resonant frequencies another eigenvalue problem can be solved for ω

$$\left(\bar{\bar{C}} - \epsilon_r \frac{\omega^2}{c^2} \bar{\bar{I}}\right) \cdot \mathcal{E} = 0 \quad (7.9)$$

The frequencies ($f = \frac{\omega}{2\pi}$) arising from this computation are completely different to the eigenvalues and eigenmodes found in the last section (λ_i and \mathbf{v}_i), indeed, these frequencies make one or more of the eigenvalues of $\bar{\bar{M}}$ null, thus, producing resonance in one or more eigenmodes. This approach permits the use of efficient algorithms to find the eigenfrequencies. Matlab's *eigs* function can find the resonant points around a given frequency without solving for the often millions of possible modes.

The abovementioned procedure has been implemented into *fdwaves*. The eigenfrequency analyzer function is capable of finding hundreds of resonant modes around the guess frequency and, additionally, it can plot the corresponding normalized modal shapes. This eigenvectors can be plotted either as field components or the total field norm. The eigenfrequency analyzer was used to find the numerical eigenfrequencies corresponding to the analytic resonances in Table 5. With a rather coarse mesh (100 by 100) and usual computational times of about 1s or less, precision up to the fourth significant decimal place in Table 5 are achievable at the 100MHz range.

Besides the frequencies provided at the table, the analyzer also found other eigenvalues. When a full simulation (i.e. not an eigenfrequency search) was performed with a central antenna along z-axis, usual resonant features, such as a high amplitude, were not found for the later frequencies. A suitable explanation is that those frequencies correspond to eigenmodes that are not excited at all by this particular forcing setup. This means that both the numerator and denominator in Equation 7.6 are 0.

Recall that the analytic frequencies shown are only valid for TE_z and TM_z transverse modes, conversely, there are many other resonances for other polarizations. A z-directed antenna only excites the TM_z mode. Figure 7.2 shows the peak amplitudes near one of the analytic transverse mode resonances and near a second kind eigenvalue. It becomes clear that, at least with the current forcing configuration, the excitation frequency in the right plot does not induce resonance despite corresponding to an eigenvalue of $\bar{\bar{C}}$.

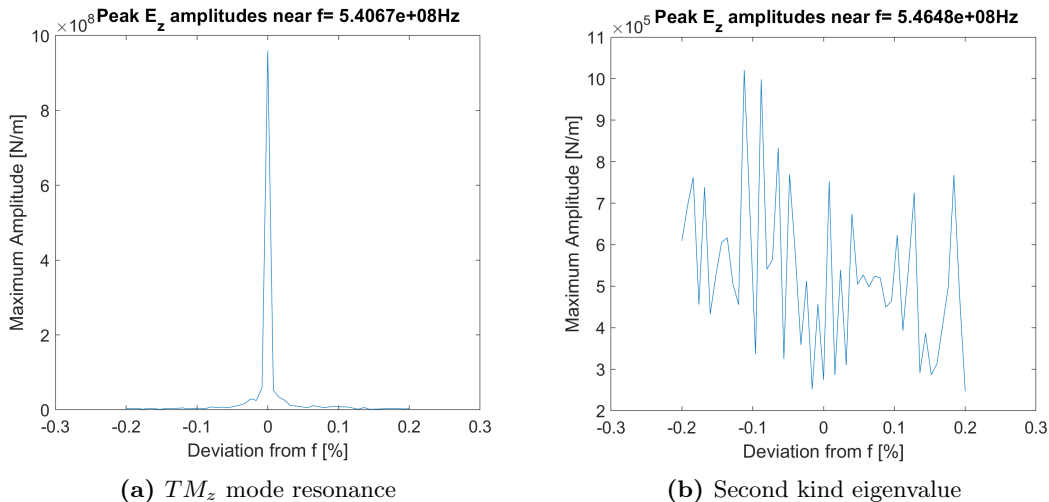


Figure 7.2: Comparison of peak amplitudes near two eigenvalues of $\bar{\bar{C}}$ under TM_z mode excitation. 51 simulations per plot with 100x100 cells per domain. 10 random antennas at random phases and magnitudes (1 to 10 A).

In Figure 7.2a we observe the narrow bandwidth at which resonance takes place. This is a characteristic of undamped systems where the **Quality Factor** is infinitely large $Q \rightarrow \infty$. High values of Q are achieved in resonators when there are no energy losses to the walls or media [17]. In vacuum and with PEC boundary conditions those losses are 0.

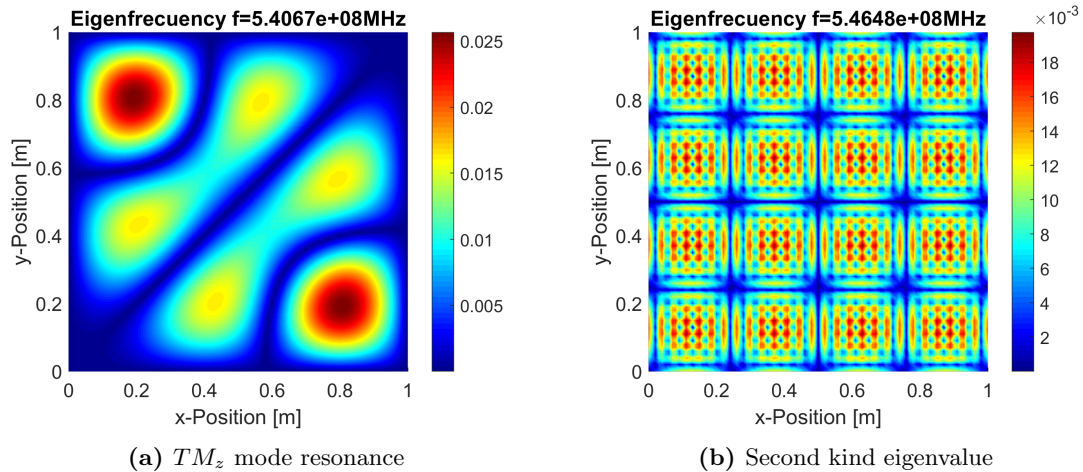


Figure 7.3: Eigenmodes (as field norm) representation for a confirmed resonance and an unidentified eigenvalue. Notice that these are modal shapes, the eigenvector is normalized to unity. 101x101 degrees of freedom.

Additionally, the modal shapes corresponding to the two eigenfrequencies are plotted in Figure 7.3. We realize that the mode in the right plot cannot be excited by z -aligned antennas. Looking at the norm of the field at the walls, it can be noticed that there must be E_x and E_y components of the field because the E_z component is always tangential to the PEC boundary conditions and, hence, null at the wall. The excited TM_z mode only has E_z field component in vacuum. This explains the lack of resonance in Figure 7.2. Both the numerator and denominator of 7.6 are close to 0 and the solution is not well defined, moreover, \bar{M} is not invertible in that case. Fortunately, we do not have to worry about this kind of singular solutions for a plasma with collisions (ultimately, the simulation objective of this thesis) because pure resonance $\lambda_i = 0$ cannot occur.

According to Equation 7.6, if one resonant mode is excited by $\tilde{\mathcal{F}}$, that mode will be much greater than the rest of non-resonant excited modes. This means that, if a random forcing is set at a resonant frequency, the response field shape is fixed regardless of the shape of the forcing term. The total magnitude is not infinite due to numerical error, in turn, it still depends on how much the forcing term excites the resonant mode.

Consequently, a good way to test resonance is to set a series of antennas with random positions, phases and currents (recall that the forcing term is a current density but we model an infinitesimal antenna with the equivalent density i.e. scaling the current density so that the integral of its interpolated value on the domain area matches the antenna current). Afterwards, several simulations are performed, if the same shape is repeatedly obtain, the system is resonant (or it is close to resonance). Certainly, an increase in amplitude will also be observable.

For the following simulations, 10 antennas will be used. Figure 7.4 shows the results (norm and phase) of 2 simulations at exactly the same arbitrary frequency. As expected the different forcing terms produce completely different results (this was not an eigenfrequency). The field is not significantly large either, indeed, the peaks are located near the antennas which are clearly observable. This is an indication that constructive interference is not strong. Observing the phase, we note that there are not detectable standing waves.

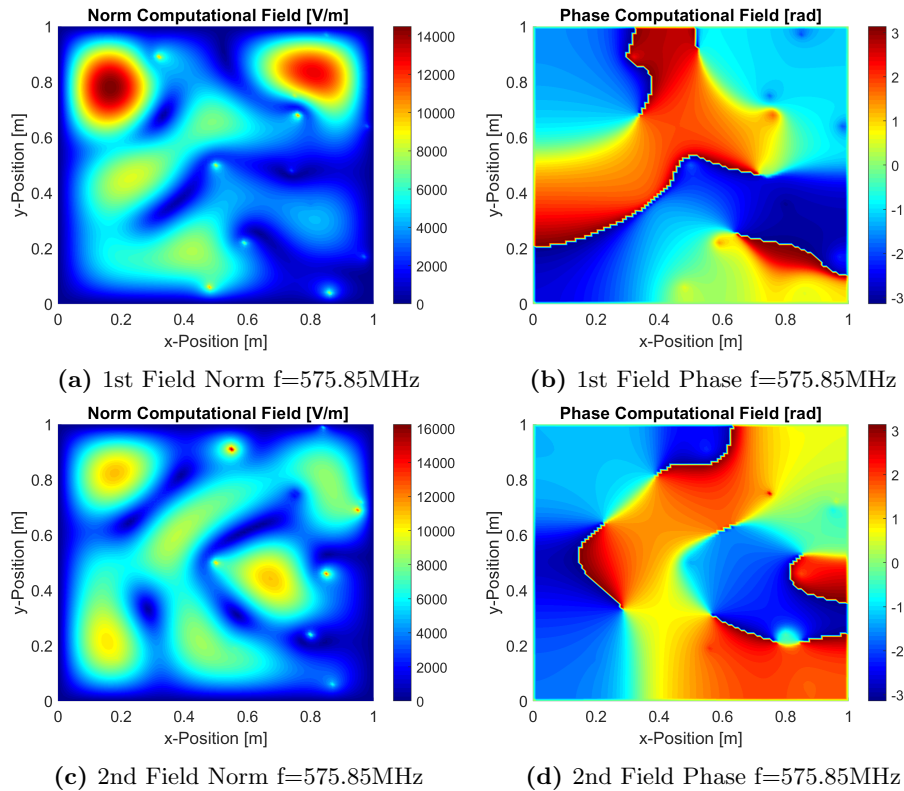


Figure 7.4: Two simulation results using *fdwaves* at an arbitrary (non resonant) frequency. 1m x 1m PEC cavity with 10 random antennas perpendicular to the propagation plane at random phases and magnitudes (-5A to 5A). 101x101 nodes, Sofd3 FD scheme.

Figure 7.5 shows the first four principal resonances of the cavity (0 frequency is disregarded because it corresponds to an electrostatic mode). These are diagonal entries in Table 5. The modal shapes appear regardless of the forcing term, randomly varied in consecutive simulations. The modes preserve symmetry across the x and y axes and the diagonals, having the same number of wavelengths in each direction. The first mode comprises half wavelength and the wave numbers of the subsequent modes are its multiples. Resonance is evident comparing the maximum amplitude of these simulations to the ones presented in Figure 7.4. The peaks are on the order of 10^7 V/m in contrast with 10^4 V/m previously found despite having the same configuration of 10 random antennas with currents from -5A to 5A. The antennas are no longer perceptible because the higher peaks are created by constructive interference.

Regarding the phase plots, two phase regions are visible in each simulation. The two regions are completely out of phase (π rad difference). It is this phase difference and not the actual value what actually determines the steady state solution (the frequency domain method is inherently steady state). The difference in the phase value in each plot, due to the the random phase of the antennas, is completely irrelevant. The simulations can be repeated indefinitely with random magnitude and phase in the antennas but the same field topology will show up.

More importantly, these are characteristic patterns of standing waves, probably the most recognizable feature of cavity resonance. The points at which phase transition takes place, called nodes, have 0 magnitude. Oppositely, the points of maximum amplitude in absolute value are called antinodes. The mechanism of formation of standing waves is usually the interference of two equal amplitude waves traveling in opposite directions. At a certain frequency (the resonant one) the higher and lower peaks of both waves arrive at the antinodes at the same time and sum up forming the two phase regions. The opposite effect is observed at the nodes, where both fields are 0. This kind of waves have important properties, specially, with regard to energy transport [22].

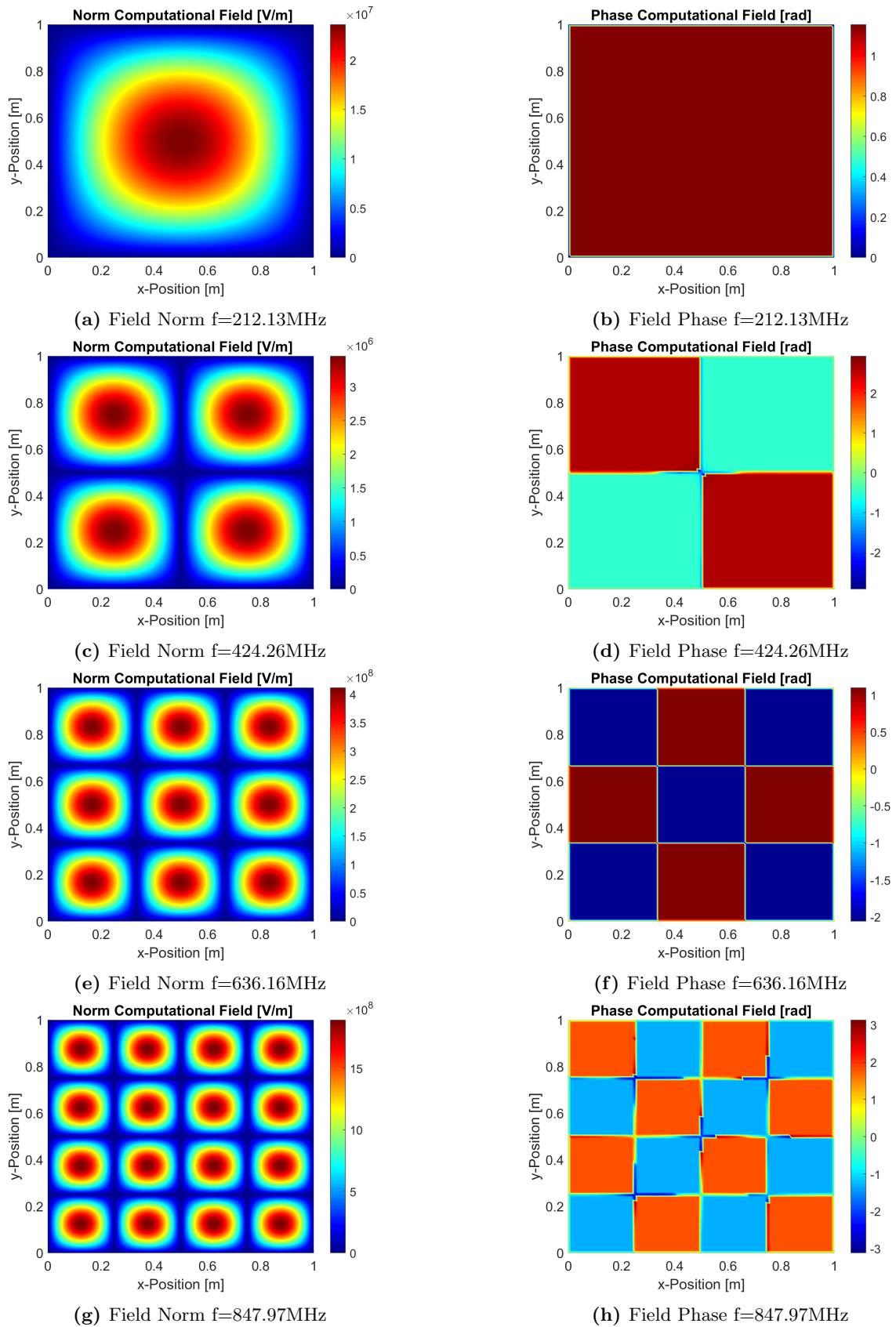


Figure 7.5: Principal resonant modes. 1m x 1m PEC cavity with 10 random antennas perpendicular to the propagation plane at random phases and magnitudes (-5A to 5A). 101x101 nodes, *fdwaves* Sofd3 FD scheme.

Finally, notice that the frequencies in the last two simulations have been slightly tuned from the analytic values (636.40MHz→636.16MHz and 848.53MHz→847.97MHz). The numerical resonance is displaced from the analytic value. This illustrates how errors build up at higher frequencies or shorter wavelengths. The fact that the system is undamped suggests that the amplitudes should go to infinity. Due to numerical inaccuracies this cannot happen. However, providing more precision to the eigenfrequency finder we can achieve much higher amplitudes with the same forcing term and mesh (up to 10^{20}). The values shown in Figure 7.5 are not noteworthy besides being large.

Turning now to the study of the eigenfrequencies out of the diagonal in Table 5, the first recognizable feature is that the matrix of frequencies is symmetric. This obviously agrees with the symmetry of the problem for a square cavity. If there is a resonant mode with 2 wavelengths in x and 1 wavelength in y, there must be another resonant mode with 1 wavelength in x and 2 in y at the same eigenfrequency. As a consequence, those eigenfrequencies must be multiple roots of the characteristic equation $\det(\tilde{C}) = 0$.

Figure 7.6 shows the resonant field created by a unique central antenna with 1A current oscillating at an off-diagonal eigenfrequency. Because the eigenfrequency is a multiple root, it is expected to have multiple corresponding resonant modes. In this particular case, the central antenna seems to only excite one of those modes.

On the other hand, Figure 7.7 shows 2 different simulations using the usual 10 random antennas at the same excitation frequency. Unlike with the diagonal frequencies, where the same modal shape always appeared, there are different shapes in the amplitude and phase plots. Additionally, there are not observable standing waves. However, there is an enormous field amplitude not expected for the small currents applied (see Figure 7.4). It seems that resonance is present but not in the usual form.

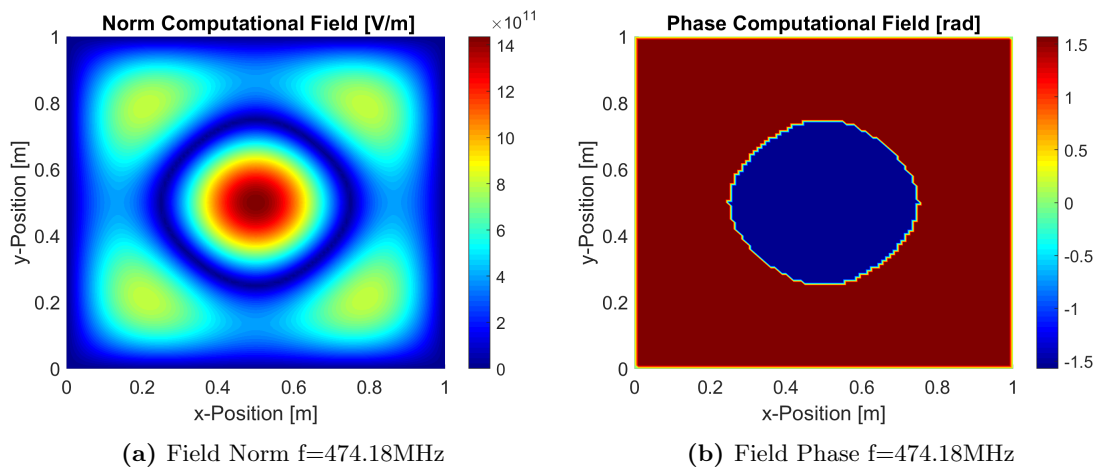


Figure 7.6: Simulation results using *fdwaves* at an off-diagonal eigenfrequency. 1m x 1m PEC cavity with 1 central antenna perpendicular to the propagation plane (1A and 0 rad phase shift). 101x101 nodes, Sofd3 FD scheme.

The explanation to this phenomenon is the interaction among comparatively large modes excited randomly by the antennas. From one simulation to another, the modes are excited in a different manner due to the random position and magnitude of the antennas. As there are several modes with eigenvalues going to 0, some of them might have comparable amplitudes and interact. The additional phase shift of the antennas also contributes to the vanishing of standing waves. Moreover, in some simulations (see Figure 7.7b), a background standing wave is still noticeable in the phase plot with some noise. This could be caused by the presence of a dominant mode (more excited by the forcing term) and the superposition of weaker ones.

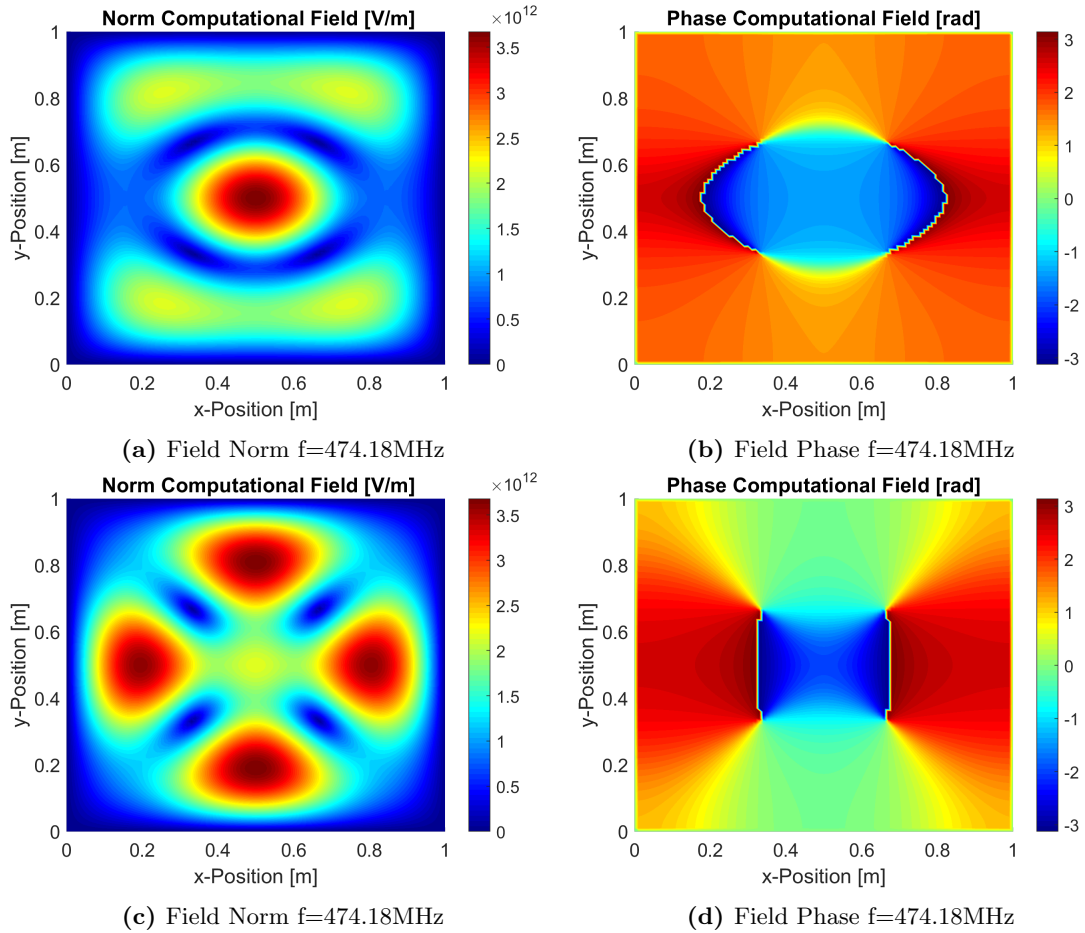


Figure 7.7: Two simulation results using *fdwaves* at an off-diagonal eigenfrequency. 1m x 1m PEC cavity with 10 random antennas perpendicular to the propagation plane at random phases and magnitudes (-5A to 5A). 101x101 nodes, Sofd3 FD scheme.

7.1.2 Vacuum Resonant Modes with Complex Geometry

The actual usefulness of numerical methods stands out when complex geometric features are included. If that is the case, analytic solutions might be very difficult or even impossible to come up with. Figure 7.8 shows a simulation with a rectangular exterior perfect electric conductor wall and another interior PEC box. The forcing term continues to be the random arrangement of antennas.

The resonant mode shown was found using the eigenfrequency analyzer utility described above. Standing waves form indicating that the modal shape is unique to the resonant frequency, this was expected considering the lack of symmetry of the problem. Another important feature observed was that the bandwidth at which resonance takes place in this problem is narrower than for a simple box. High precision in the frequency is needed to find the resonances correctly.

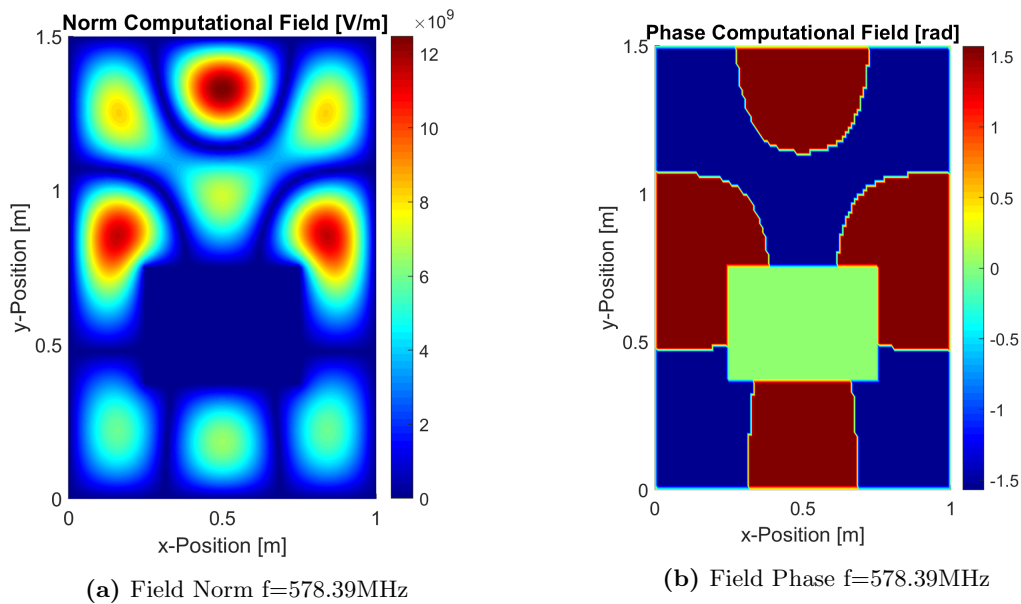


Figure 7.8: Resonant field in a complex geometry PEC cavity. 10 random antennas perpendicular to the propagation plane at random phases and magnitudes (-5A to 5A). 101x101 nodes, *fdwaves* Sofd3 FD scheme.

7.1.3 Plasma Resonant Modes

Equation 7.8 can be modified to account for plasma, in this case a matrix containing the dielectric coefficients from the schemes in Chapter 4.2 and for all the degrees of freedom is introduced

$$\bar{M} \cdot \mathcal{E} = \left(\bar{C} - \frac{\omega^2}{c^2} \bar{K} \right) \cdot \mathcal{E} = 0 \quad (7.10)$$

To take advantage of the advanced eigenvalue and eigenvector finder algorithms, we wish to modify the equation so it becomes an eigenvalue problem

$$\det \left(\bar{K}^{-1} \bar{C} - \frac{\omega^2}{c^2} \bar{I} \right) = 0 \quad (7.11)$$

The resonant modes and frequencies arise from the eigenvalues and eigenvectors of the matrix $\bar{R} = \bar{K}^{-1} \bar{C}$. The problem can be solved by the eigenfrequency utility included in *fdwaves*. Inverting matrix \bar{C} , multiplying by \bar{K} and, afterwards, looking for the eigenvalues is a considerable computational workload. For a 101×101 nodes configuration these are non-symmetric sparse matrices with dimensions 30603×30603 . Although it will be shown that plasma simulations converge at microwave frequencies $\sim 2.5\text{GHz}$ with about 10^5 nodes in a $1m \times 1m$ cavity, we will keep the 101×101 nodes setup and lower the frequencies to the 500MHz range to ensure convergence while reducing the computational time.

Two resonant modes are shown in Figure 7.9. The plasma parameters are $\omega_p = 1.5\omega$ and $\Omega_e = 2\omega$ with the static magnetic field vector aligned with the x-axis and negligible ion contribution to particle motion. The first is a highly collisional plasma with $\nu_e = 0.25\omega$. Conversely, the second simulation is configured with a very low collision frequency $\nu_e = 0.0001\omega$. We do not expect convergence in the last simulation for such a low collisionality as there might be waves propagating at very short wavelengths near the resonant cone. Regardless of the accuracy, this simulation is still useful to illustrate the interesting behavior explained below.

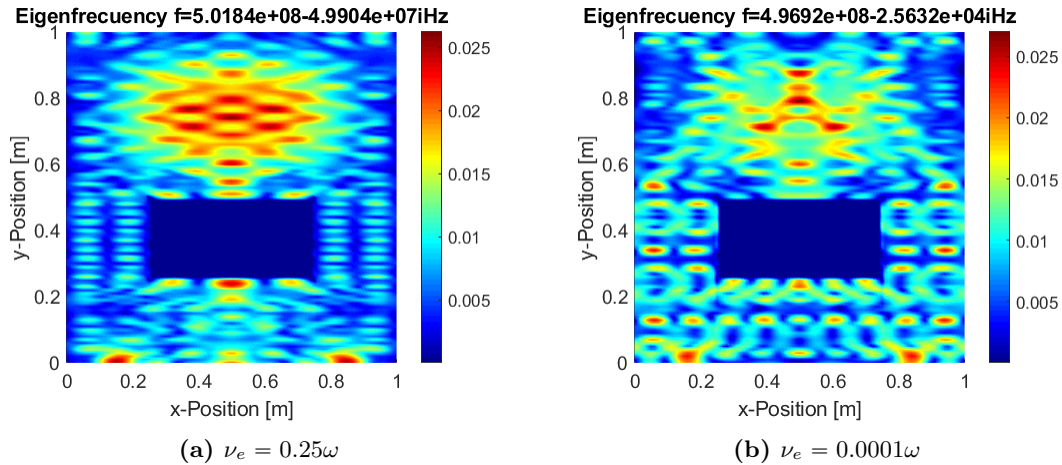


Figure 7.9: Resonant field in a complex geometry PEC cavity. 10 random antennas perpendicular to the propagation plane at random phases and magnitudes (-5A to 5A). 101x101 nodes, *fdwaves* Sofd3 FD scheme.

Looking at the eigenfrequency values shown in both plots, it can be observed that both have imaginary parts. The same behavior is detected for every single analyzed eigenfrequency. This means that there is not any zero eigenvalue λ_i for real excitation frequency configurations (the eigenvalue finder tolerance is 10^{-14}). Resonance is not achievable when collisions are present. This behavior was expected as stated in Chapter 3. Nonetheless, notice that, for very low collisionality, the imaginary part is several orders of magnitude smaller than the real part. A close enough real frequency could significantly excite this mode. Although pure resonance does not occur, great field amplitudes can arise. It is clear that the quality factor grows when the collision frequency diminishes and quasi-resonant conditions are achievable.

7.2 ECR waves in Plasma

We turn now to the study of wave propagation in plasma and inside a perfectly conducting box. The wave patterns created at the resonant modes are mainly caused by interference of reflected waves. As a consequence, they hide the underlying mechanisms of wave propagation. Therefore, it might be good to study the behavior away from cavity resonant frequencies. At this point, recall that plasma resonances observed in wave normal surfaces (see Figure 3.3) and cavity resonance are different phenomena. The former refer to the unbounded growth of spatial frequency leading to a change of propagation regime in the absence of collisions.

High resolution simulations were performed with 401×401 nodes. This is necessary to get residuals less than 1% in the most critical case (magnetic field at $> 30deg$ with respect to the grid orientation and less than 0.1ω collision frequency). The excitation frequency was lowered from prior plasma simulations in the convergence tests ($\sim 2 - 3GHz$) to $1.5GHz$ (although this frequency is still much higher than vacuum thanks to the role collisions). This also helps visualization because the wavelengths are not excessively short. It was checked that this value is not a plasma cavity resonant frequency for the chosen cavity geometry.

A single central node perpendicular antenna is set up. This forcing produces waves initially propagating in every plane direction. Note that the area near the antenna has been obscured. Due to the sharp resolution and the single point configuration, there was a very high current density in the antenna node producing a really large field nearby. The antenna was too bright and it was hiding other interesting wave features. Instead of scaling the whole field it was decided to eliminate the antenna from the electric field norm plot. Also note that, unlike vacuum, the field in plasma might have components in all the three directions even with forcing directed along the z-direction.

Figure 7.10 shows the resulting field norm. Reflected R wave interference patterns are observed along the x-direction aligned with the static magnetic field. Recall that the R,L labeling refers to the polarization of the wave traveling parallel to the magnetic field. The wavelengths become shorter away from the x-axis. The resonance cone is observable and there is a very low propagation perpendicular to the static magnetic field. The low intensity field along the perpendicular direction is created by a fast L-polarized wave appearing in regime 7 of plasma properties in the CMA diagram, (see Figure 3.3).

Despite all the abovementioned facts lead to identify the parallel propagating wave as an R wave, interference due to reflection makes this results hard to interpret. We observe the formation of quasi-standing waves (the field at the nodes is not zero, neither is the standing wave ratio) and the phase plot (not shown here) becomes rather chaotic.

Without PML boundary conditions, it is difficult to isolate the wave from the interference produced by reflections. Nevertheless, it is possible to set a very strong damping by particle collisions. Then the wave is absorbed within the plasma before reflecting. Unfortunately, setting a very high collision frequency changes the topology of the normal surfaces as shown in Figure 7.13. Another strategy is to keep a low collision frequency and simulate the propagation on a very large domain. This procedure relies on the wave decay before arriving at the walls. The main limitation in this case is the number of nodes and the computational resources available. These issues illustrate the need for a perfectly match layer (PML) for future studies.

The simulation shown in Figure 7.11 is a compromise between these two factors. The domain was enlarge to $5m \times 5m$. The collision frequency was risen to $\nu_e = 0.8\omega$. The wave normal surface changes significantly from the one expected in an ECR thruster (with lower collisionality) but keeps most characteristic features of these waves as explained later in this section.

In Chapter 3 the polarization of different waves in plasma was explained. Parallel R waves have right hand polarization with respect to their main propagation direction i.e. the direction of the static magnetic field. If the wave is excited by an antenna perpendicular to the plane, the field will always have a periodic E_z component. Another field component perpendicular to the propagation direction but contained in the propagation plane also appears. Circular polarization implies that both E_z and E_{\parallel} components are out of phase and have the same amplitude (refer to Chapter 3 or the book by Stix [44] for a detailed explanation on plasma wave polarization).

Consequently, it was decided to plot the E_z component phase of the field. Due to the periodicity and the circular polarization, the wavefronts and wavelengths should be clearly shown in such a plot. The magnetic field was oriented at 30deg with the x-axis in order to show the anisotropy in the wave propagation. The high collisionality makes this setup lie on region 7 of the CMA diagram although ECR thrusters usually work on region 8. Despite this inconvenience, an R wave arises at this configuration together with a fast L wave that would not propagate on region 8.

The E_z field phase is shown in Figure 7.11. L (fast) and R (slow) waves are clearly observed. Recall that the L and R tags refer only to polarization in the propagation direction parallel to the magnetic field. For any other direction, the polarization is not necessarily circular. The resonance cone is also observable. There are also noisy areas that are thought to be caused by reflections. However, this noise is irrelevant because the intensity of the field is very low in this regions as shown in Figure 7.12

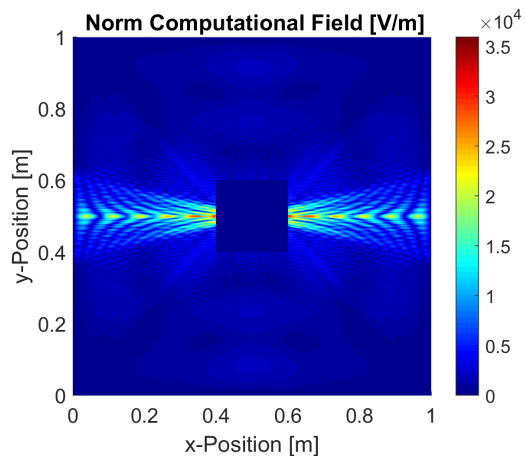


Figure 7.10: Interference pattern from reflection, quasi-standing ECR waves. Plasma parameters $\Omega_e = 2\omega$, $\omega_p = 2\omega$, $\nu_e = 0.1\omega$. 501×501 nodes *fdwaves* simulation

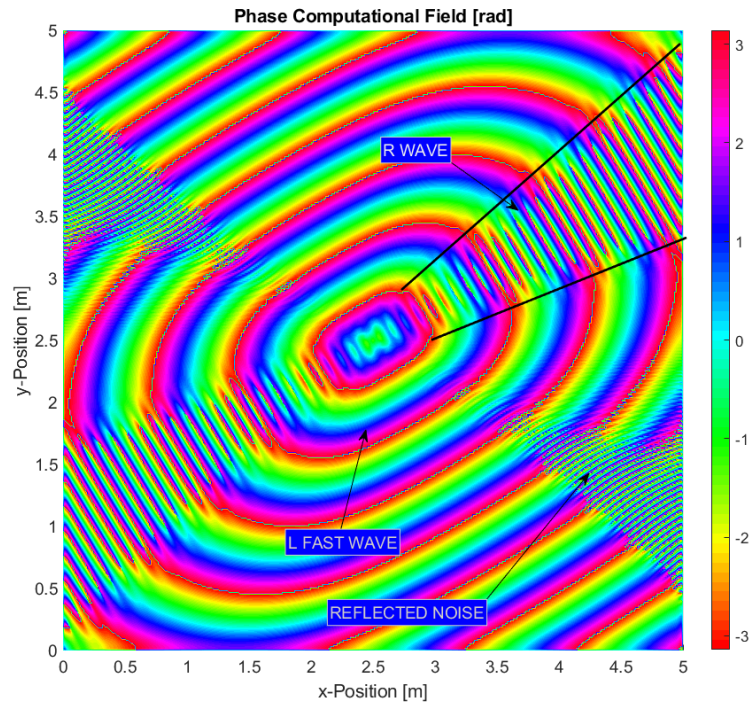


Figure 7.11: Highly damped ECR waves, E_z field phase. Plasma parameters $\Omega_e = 2\omega$, $\omega_p = 2\omega$, $\nu_e = 0.8\omega$. Magnetic field at 30deg with x-axis. Excitation frequency $f=1.5\text{GHz}$. 501×501 nodes *fdwaves* simulation

where it was necessary to use a logarithmic plot due to the high damping and the rapid wave decay.

For a further study of the arising waves, it is convenient to inspect the normal surfaces corresponding to this plasma parameters in Figure 7.13b. As usual, the different polarizations are represented with different colors and the imaginary part is dashed. Convergence to the analytic solution is completely achieved for the selected step size so the solutions to the dispersion relation are physical.

Starting by the L wave (red), we observed an inner oval of low spatial frequencies, this means that the phase velocity is high and the wavelengths long. The wavenumber is still slightly lower in the direction parallel to the magnetic field (30deg with the x-axis). Regarding the imaginary part, there is high damping in every direction, somehow stronger perpendicular to the magnetic field.

Looking now at the R wave (red), a much noticeable anisotropy is observed. The spatial frequency is maximum in the region comprised by the resonance cone where it is kept almost constant. This comes with low damping due to collisions with a minimum for propagation parallel to the magnetic field. On the other hand, perpendicular propagation is highly damped and has lower spatial frequencies. The enormous damping in this direction explains the lack of propagation observe in Figure 7.11.

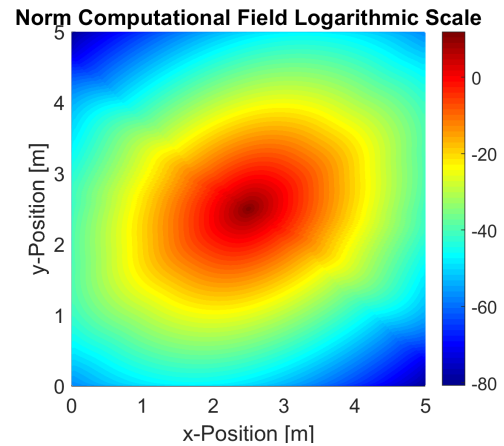


Figure 7.12: E_z field Logarithmic Scale of the field shown in Figure 7.11

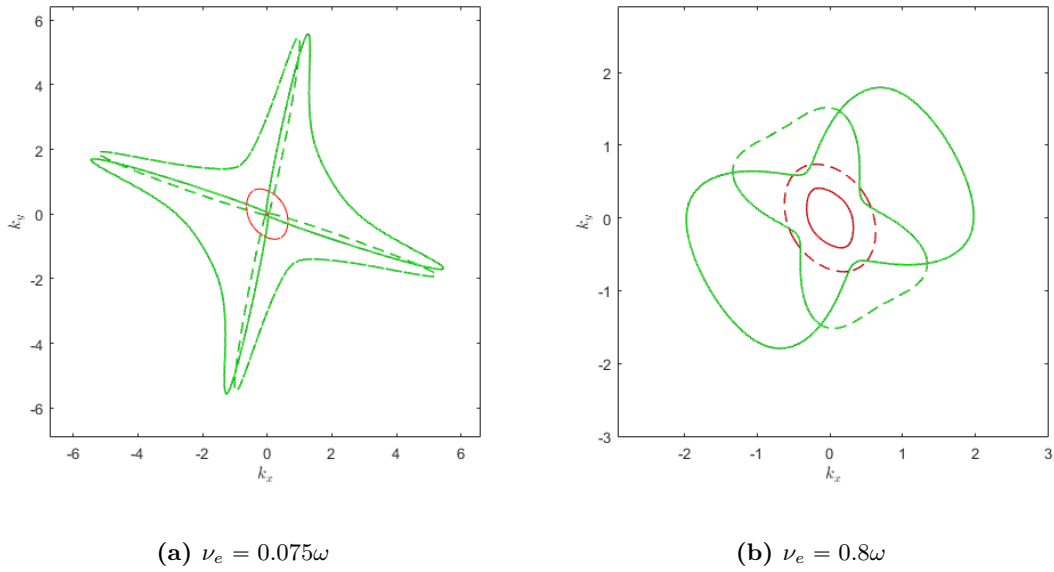


Figure 7.13: Spurious free normal surfaces, high precision $h = 0.005c/\omega$. Fast L wave (red), R wave (green). Plasma parameters $\Omega_e = 2\omega$, $\omega_p = 2\omega$, $\nu_e = 0.8\omega$. Magnetic field at 30deg with x-axis.

To end the discussion on ECR wave propagation, let's inspect what would be expected for a more realistic case with lower collision damping. Figure 7.13a shows this kind of configuration. The L wave's real part has shrunk to a very small oval. As a consequence, a really long and damped wave would appear, this essentially makes the wave negligible so, in practice, there is no propagation. There is not any propagation of the R wave in the direction perpendicular to the magnetic field either. Inside the resonance cone damping is really light so wave attenuation would only be observed after long traveled distances. This clearly explains the difficulty to avoid reflected waves without a PML.

In the phase plot of Figure 7.11 we observe almost straight R wave's wave-fronts. The reason is that the spatial frequency is almost constant inside the resonance cone. This no longer happens when the collision frequency is lowered. The wavenumber becomes greater away from the magnetic field direction. The consequence is the deformation of the wave shown in Figure 7.14. The central part moves faster and the wavefronts are closer in the limits of the cone.

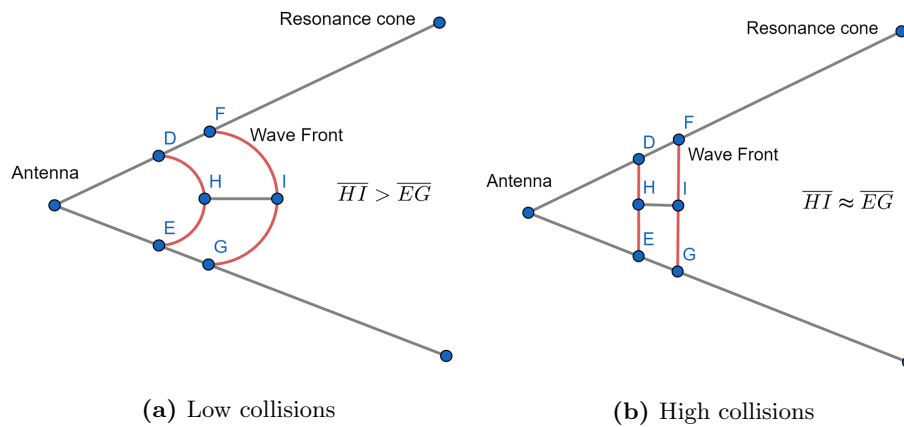


Figure 7.14: Resonant cones and R wave fronts with high and low collisionality.

8 Future work

Albeit interesting results were achieved with the current *fdwaves* capabilities, the code is still lacking of some powerful characteristic needed to carry out precise simulations with an accurate geometric modeling of a certain thruster. This chapter is devoted to the introduction of some of those tools keeping in mind that they have not been integrated in any working simulation code. This means that no testing has been performed and their validity has not yet been proven. All the functionalities presented are either under study or in an advanced phase of development.

8.1 Non-uniform grids: *fdschemes*

The following derivations are based on the Finite Difference Calculator by Cameron Taylor[11]. The integration of the cross derivatives and the vector calculus operators was done during the development of this thesis and implemented in the Matlab function *fdschemes* for the application in the arbitrary geometry FD code presented in a later section. Let's suppose we wished to find an approximation for the fourth derivative $d = 4$ in an uniform and centered stencil with dimensions $N=5$ such that

$$\frac{\partial^4 f}{\partial x^4} \approx c_1 f(x-2h) + c_2 f(x-h) + c_3 f(x) + c_4 f(x+h) + c_5 f(x+2h) \quad (8.1)$$

We can write the Taylor expansion until the fifth derivative $d + 1 = N$ for all the terms in Equation 8.1 yielding

$$\begin{aligned} c_1 f(x-2h) &= c_1 \left(-(2h)^1 f'(x) + \frac{1}{2}(2h)^2 f''(x) - \frac{1}{6}(2h)^3 + \frac{1}{24}(2h)^4 f^{IV}(x) - \frac{1}{120}(2h)^5 f^V(x) + \dots \right) \\ c_2 f(x-h) &= c_2 \left(-(h)^1 f'(x) + \frac{1}{2}(h)^2 f''(x) - \frac{1}{6}(h)^3 + \frac{1}{24}(h)^4 f^{IV}(x) - \frac{1}{120}(h)^5 f^V(x) + \dots \right) \\ c_3 f(x) &= c_3 f(x) \\ c_4 f(x+h) &= c_4 \left((h)^1 f'(x) + \frac{1}{2}(h)^2 f''(x) + \frac{1}{6}(h)^3 + \frac{1}{24}(h)^4 f^{IV}(x) + \frac{1}{120}(h)^5 f^V(x) + \dots \right) \\ c_5 f(x+2h) &= c_5 \left((2h)^1 f'(x) + \frac{1}{2}(2h)^2 f''(x) + \frac{1}{6}(2h)^3 + \frac{1}{24}(2h)^4 f^{IV}(x) + \frac{1}{120}(2h)^5 f^V(x) + \dots \right) \end{aligned}$$

In order to cancel out first, second and third derivatives, the following system of equations arises. Note that the truncation error for this approximation is $O(h^5)$.

$$\begin{pmatrix} 1 & 1 & 1 & 1 & 1 \\ -2 & -1 & 0 & 1 & 2 \\ 4 & 1 & 0 & 1 & 4 \\ -8 & -1 & 0 & 1 & 8 \\ 16 & 1 & 0 & 1 & 16 \end{pmatrix} \begin{pmatrix} c_1 \\ c_2 \\ c_3 \\ c_4 \\ c_5 \end{pmatrix} = \frac{1}{h^4} \begin{pmatrix} 0 \\ 0 \\ 0 \\ 0 \\ 24 \end{pmatrix} \quad (8.2)$$

A detailed analysis of the system in Equation 8.2 provides the general method of coefficient search for any derivative in an arbitrary stencil. Denoting \mathbf{s} the vector containing the relative position of the nodes in a certain stencil with 0 being the node in which derivatives are sought ($\mathbf{s} = [-2, -1, 0, 1, 2]$ for the problem above)

$$\begin{pmatrix} c_1 \\ \vdots \\ c_N \end{pmatrix} = \frac{1}{h^d} \begin{pmatrix} s_1^0 & \cdots & s_N^0 \\ \vdots & \ddots & \vdots \\ s_1^{N-1} & \cdots & s_N^{N-1} \end{pmatrix}^{-1} \begin{pmatrix} 0 \\ \vdots \\ d! \\ \vdots \\ 0 \end{pmatrix} \quad (8.3)$$

Where N are the dimensions of the stencil and d is the derivative sought. The factorial of the derivative $d!$ must be placed in the $d + 1 \leq N$ entry in the last vector of Equation 8.3. Written in compact form, this equation reads

$$s_1^n c_1 + \cdots + s_N^n c_N = \frac{d!}{h^d} \delta(n - d) \text{ for } 0 \leq n \leq N - 1 \quad (8.4)$$

Where $\delta(x = 0) = 1$ and $\delta(x \neq 0) = 0$. Equation 8.3 was implemented in Matlab in a vectorized form for improved performance. Using the procedure above, we can define an operator giving the finite difference coefficients for a derivative d from an arbitrary stencil vector.

$$\mathcal{C}(\mathbf{s}, d, h) = \mathbf{c} \quad (8.5)$$

Note that this operator always provides the **higher order approximation** for the input stencil. For instance, let's try to find the first, second and cross derivatives in a 9×9 computational cell. The stencil is completely defined by two vectors \mathbf{s}_x and \mathbf{s}_y , remember that this scheme is not uniform but it is structured so the two vectors define a grid element with coordinates $S^{i,j} = (s_x^i, s_y^j)$ for $1 \leq i \leq 3$ and $1 \leq j \leq 3$. Additionally, we define a matrix of function values in the stencil S , $\bar{F} \in \mathbb{C}^{3 \times 3}$ and coefficients matrices $\bar{C} \in \mathbb{R}^{3 \times 3}$ such that

$$\bar{C}_x = \begin{pmatrix} 0 & \vdots & 0 \\ 0 & \mathbf{c}_x & 0 \\ 0 & \vdots & 0 \end{pmatrix} \quad \bar{C}_y = \begin{pmatrix} 0 & 0 & 0 \\ \cdots & \mathbf{c}_y^T & \cdots \\ 0 & 0 & 0 \end{pmatrix} \quad (8.6)$$

$$\frac{\partial f^d}{\partial x^d} \approx \langle \bar{C}_x F \rangle_F \quad (8.7)$$

Where $\mathbf{c}_x = \mathcal{C}(\mathbf{s}_x, d, h)$ and $\langle \bar{C}_x F \rangle_F$ denotes the Frobenius inner product which is simply the element-wise multiplication and the subsequent sum of all terms. This nomenclature, that is not otherwise necessary for first and second derivatives (the same could be done using vector inner products), will be useful later to work with cross derivatives. From now on, we will name \bar{C}_x the coefficient matrix for the first derivative and \bar{C}_{xx} for the second derivative, same applies to the y-direction. It is straightforward to find the first and second derivative coefficients for the implementation into the scheme equations. However, it is not so clear how to obtain the cross derivatives.

For the construction of the cross derivative coefficient matrix, we take advantage of the distributive property. It is possible to take the first derivative in the x-direction in the center nodes of each of the three columns in the stencil S and, afterwards, apply the y-derivative of the resulting x-derivatives in the central row. The opposite procedure is completely equivalent. Mathematically, the operation is represented by the outer tensor product (Kronecker product) of the two vectors producing a matrix

$$\bar{C}_{xy} = \mathbf{c}_x \otimes \mathbf{c}_y \quad (8.8)$$

$$\frac{\partial^2 f}{\partial x \partial y} \approx \left\langle \bar{C}_{xy} F \right\rangle_F \quad (8.9)$$

Note that, in general, the cross derivative matrix does not have 0 components through either rows and columns as do the first and second derivatives matrices which only used aligned nodes. The advantage of using the matrix nomenclature is clearly observed when derivatives are mixed, for instance, the curl-curl operator projected in the x-direction can be easily discretized using this procedure

$$\begin{aligned} [\nabla \times (\nabla \times \mathbf{E})] \cdot \mathbf{1}_x &= -\left(\frac{\partial^2 E_x}{\partial x^2} + \frac{\partial^2 E_x}{\partial y^2} + \frac{\partial^2 E_x}{\partial z^2}\right) + \frac{\partial^2 E_x}{\partial x^2} + \frac{\partial^2 E_y}{\partial x \partial y} + \frac{\partial^2 E_z}{\partial x \partial z} \approx \\ &\approx \left\langle (\bar{C}_{yy} + \bar{C}_{zz}) \mathcal{E}_x \right\rangle_F + \left\langle \bar{C}_{xz} \mathcal{E}_y \right\rangle_F + \left\langle \bar{C}_{xy} \mathcal{E}_z \right\rangle_F \end{aligned} \quad (8.10)$$

Where \mathcal{E} denotes the field values in the stencil nodes. This method is easy to implement into code in a very compact form preventing common errors in large coefficient functions. It is also very flexible and can be used to discretize arbitrary equations with high order derivatives in any valid non-uniform structured stencil. For example, to obtain the coefficients in Sofd5, the only necessary modification from Sofd3 is to feed a stencil $\mathbf{s}_{x2} = [-2, 0, 2]$ for the construction of the second derivative matrix. On the other hand the first and cross derivatives still use the standard stencil $\mathbf{s}_{x1} = [-1, 0, 1]$.

Interestingly, the same Sofd5 computational cell can be used to obtain a fourth order scheme for the second derivatives using a 5 component stencil $\mathbf{s}_{x2} = [-2, -1, 0, 1, 2]$. This was not done during the development of *fdwaves* due to the expected appearance of spurious solutions of the first kind (see Chapter 5). Nonetheless, a deeper study is proposed for the future as this issue does not seem to be as critical for a collisional plasma. Also note that the *fdwaves* code is already prepared to handle 25×25 computational cells.

Notice that the order of the Finite Difference approximation for a certain scheme can be easily found by plotting the error in the derivatives of a general analytic function¹⁵ as a function of the node spacing and, subsequently, fitting the arising curve with a power model of the form $f(x) = ax^b$, where b is the order of the scheme; this was already done in chapter 6.

It has been proposed to upgrade this automatic scheme coefficient writer to 2 and 3 dimensions to increase the order of the derivatives. Finally, it must be taken into account that this is not the most efficient method for the implementation into a simulation code due to the need for a matrix inversion. However, it is the most versatile and easy form of implementation once a function is created (this was done in a vectorized form in Matlab). It was also shown that the assembly of the matrix of coefficients is not as critical as the solving step (see Chapter 6 for performance figures), consequently, this method is still quite useful for preliminary scheme evaluation.

¹⁵Trigonometric functions can be tricky to handle because some terms in the Taylor series might cancel out due to the symmetry of these functions. A function with no symmetry such as an exponential is preferred for testing

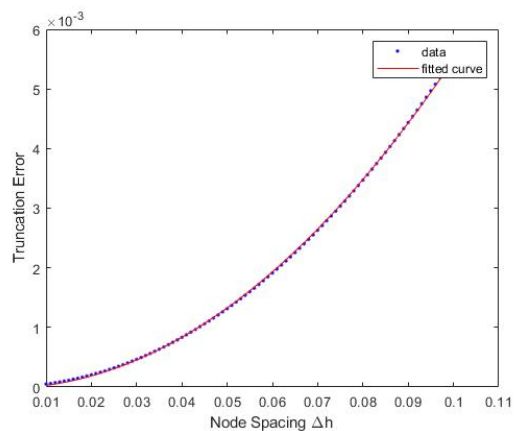


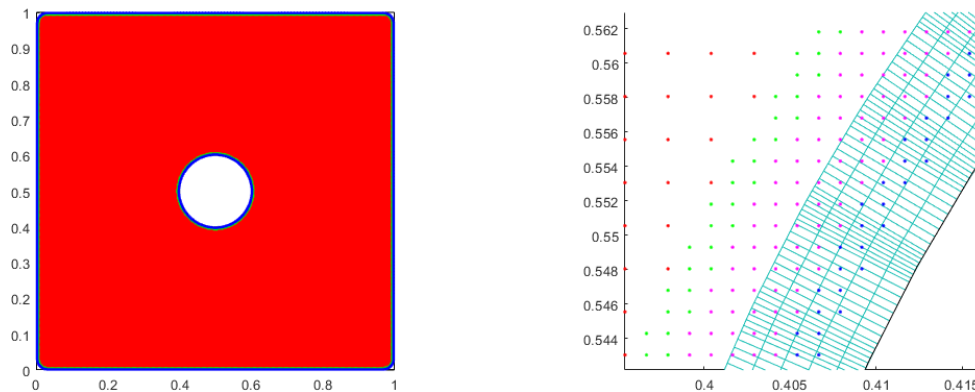
Figure 8.1: Truncation error as a function of the node spacing. First derivative with $\mathbf{s} = [0, 1, 3]$ stencil. Results show $b=2.026$ in the power curve fitting $f(x) = ax^b$. We conclude that this scheme is order 2.

8.2 Arbitrary geometry: *fdmesher* code

Probably the most significant limitation of Finite Difference methods is the difficult mapping of complex geometric features. Several alternatives such as unstructured meshes have been introduced in the literature [45]. The solution here proposed relies on the utilization of multiple independent grids for the mapping of walls, either external or internal, and the interior of the domain. The main drawback of this approach might be the introduction of error due the interpolation among grids. Bearing this in mind, a powerful interpolation method was used. The first part of a new simulation package has already been created and tested, this corresponds to the discretization of the problem geometry and the construction of the superimposed meshes. The procedure for the construction of the matrix of coefficients comprises several steps, a complete implementation is not currently available but important steps toward it are described below.

8.3 Types of Meshes

There are two distinguishable meshes for any boundary imposed in the problem; a wall mesh mapping the geometry of the boundary (cyan in Figure 8.2) and a transition mesh. Additionally, the transition mesh is subdivided in inner (blue), central (pink) and outer (green) nodes. Finally the transition mesh connects to the background mesh (red) which is common to the whole domain independently of the boundary regions. Figure 8.2 shows two wall and transition meshes for the exterior wall and the interior circle respectively, however, the background mesh is unique. The setup is for Sofd5 FD scheme. Due to the different computational cell, Sofd3 would only need one row of outer and inner transition nodes. The role of each mesh is explained below.



(a) Computational Domain with Internal Feature (b) Detail of the wall, transition and central meshes

Figure 8.2: Mesh created with *fdmesher*, 233728 nodes, maximum curvature limited to 0.47 deg.

- The **background mesh** (red) is uniform and is built with a considerably higher node distance than the wall mesh. The objective of this mesh is to reduce the total number of nodes. Due to its easy implementation. being a mesh without boundary conditions or forward differences, higher order schemes could be included.
- The **outer transition nodes** (green) belong to the transition mesh and are used to connect the background mesh nodes with the lower computational cell size near the wall. Forward FD equations have to be applied in some directions due to the lack of nearby background nodes (see Figure 8.2b).
- In the **central transition nodes** (pink) conventional uniform scheme equations are applied. Notice that throughout the transition mesh, a cell size on the order of the wall mesh is sought to achieve high quality interpolations.

- In the **Inner transition nodes** (blue) interpolation equations, explained later, are used to connect these nodes to the wall mesh. There is certain penetration of the transition mesh into the wall mesh to assure that every node can be interpolated.
- The **wall mesh** (cyan) is the most critical part of the code. In the outer most rows (2 rows for Sofd5 and 1 for Sofd3), interpolation equations are used with the transition mesh nodes as reference points. The achievement of the coefficients for the rest of the nodes is explained below:

In order to correctly map the boundary geometry, the wall mesh must be deformed into an unstructured stencil in certain regions. This induces significant errors and lowers the order of the scheme. The explanation is illustrated in Figure 8.3. It can be observed that the effective point at which derivatives are taken (red) is not coincident with the reference central point of the stencil (blue). Nevertheless, it can be shown that the order approaches the nominal structured stencil order (2 for Sofd3 and Sof5) for very small deformation angles $\theta_1 + \theta_2 \rightarrow 0$. The mesher must keep this curvature low. This is done by means of a compromise between the correct mapping of the geometry and the total number of nodes.

Besides unstructured, the wall mesh contains non-uniform stencils for the transition between high node density curving areas and low density straight regions, this can be observed in Figure 8.2b. The non-uniform coefficient writer function *fdschemas* is utilized for this task.

Furthermore, the equations on the boundary nodes are much easily implemented if a local coordinate system is used (green in Figure 8.3). This greatly simplifies the equations at the price of having to apply linear combinations of the coefficients accompanying the scheme nodes to account for the change of basis and the postprocessing of the arising fields in these nodes to express them in the global Cartesian coordinate system.

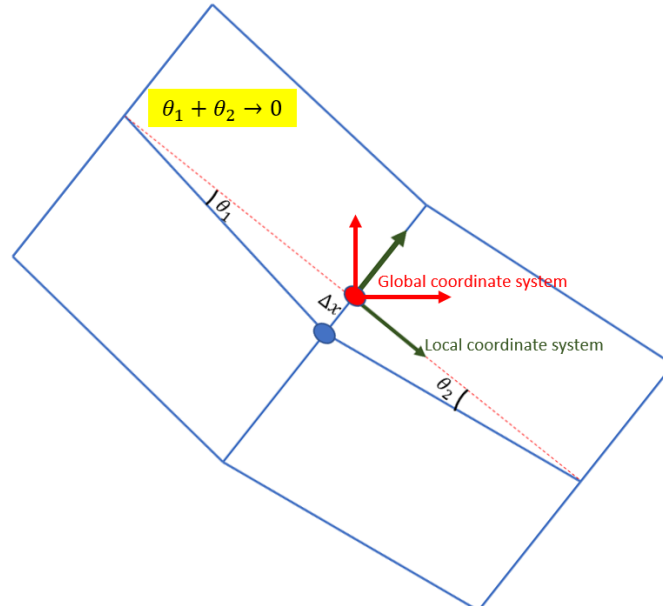


Figure 8.3: Wall Mesh Structure

8.3.1 Mesh construction

Specific details on the complex *fdmesher* algorithm are out of the scope of this thesis. Nonetheless, the steps followed for the generation of the different meshes are as follows: Firstly, the geometric

features input by the user are discretized in 1D (these inputs are closed contour lines for physical meaningfulness). Afterwards, the wall mesh is propagated from the discrete points. Finally, transition and background meshes are placed to fill the internal domain. This last step permits the attainment of a high node density near the wall while keeping the total number of nodes acceptably low (lower density is needed in the inner domain). The set of meshes are built pursuing three main objectives:

- Accurate modeling of the problem geometry: Any geometrical feature within an acceptable range of sharpness for a certain number of nodes is modelable. The shapes can be input in the mesher function as collections of connected wall nodes (the final node should be nearby the initial one), strange setups are rejected by the program. The user should provide the wall type i.e. interior or exterior. In addition to boundary regions, independent mesh regions can be created. This is meant to be used in areas where higher precision (higher node density) is sought.
- Avoidance of corners: Staircase approximations to model different geometries have been used in several FD codes, however, this approach produces a high field concentration on the corners increasing with the node resolution (a typical ‘lightning rod’ behavior well known in electromagnetism). This behavior is non-physical and undesirable. Either for exterior or interior walls, the new code eliminates any corner, indeed, the geometry is discretized rounding any sharp turn. This also adapts better to real problems where infinitely sharp corners do not exist. Of course, indefinitely sharp geometries can be modeled if the necessary number of nodes is provided by diminishing the radius of curvature of rounded corners.
- Limitation of the curvature across a single computational cell: As explained in the last section, the deformation of the wall mesh lowers its order and induces error. In order to prevent excessive deformation, the user can provide a maximum turning angle in all the stencils. The mesher assures that this value is not surpassed by increasing the node density when needed or rounding the corners to a higher radius of curvature, hence, losing precision in the mapping of the geometry. This operation is governed by a set of configuration parameters.

Looking at the setup in Figure 8.2, some preliminary conclusions arise. With about 250000 nodes, we achieved a very precise mapping of the geometry (the rounding of corners is almost imperceptible). Simulations with more than 500000 nodes have been performed in a few minutes using *fdwaves* so we expect the solver to work fine up to this number. At the same time, the wall mesh deformation was kept at a maximum of 0.47deg per computational cell. In principle, the method seems computationally feasible. Of course, we will need to wait to the first simulations to actually test it.

It should be mentioned that the configuration parameters for mesh generation have not been studied in detailed, for example, we don’t exactly know which is the optimal number of levels for the wall mesh or which is a good value for the maximum turning allowance in the wall stencil. This should have to be determined when simulations are available and a parametric and performance analysis is carried out.

8.4 Interpolation

Probably the most powerful feature of the proposed code is the high precision interpolation technique used to connect the independent grids. Bicubic interpolation, a method initially used in image processing [30], was implemented. This has been proven to be a much accurate technique than nearest node and bilinear interpolation.

For instance, if an outer wall node were to be interpolated (query point), the 4 nearest transition nodes forming a square surrounding it would be utilized as reference points. Additionally, in order to construct a cubic function in two dimensions, it is necessary to know the derivatives and cross derivatives on those nodes totaling 16 coefficients in the polynomial expression. Those derivatives are found using finite difference coefficients and the function value of the immediately outer nodes.

To sum up, this interpolation is able to resample discrete data gathering information of 16 nodes in contrast to just 4 nodes in a bilinear approximation (see Figure 8.4). Therefore, in a similar manner as we did for FD schemes with different local stencils, we can consider a computational cell for interpolation at a given node, this time the size being 4×4 .

Although the interpolation problem reduces to solving a system of linear equations when the function values are explicitly known (basically inverting a 4×4 matrix), the development of a general function capable of implementing the bicubic method into the matrix of coefficients is almost impossible to attain manually. Among the complications we should mention that there is functional dependence on the position of the query node with respect to the surrounding nodes, FD approximations are involved and, in the most general case, the mesh is not uniform. The symbolic toolbox of Matlab had to be used to obtain the entries to the coefficient matrix, these expressions are several lines of code long for all the 16 coefficients (one for each node used). This is obviously an issue when it comes to computational times but the method is implemented on the grounds that the solver is several times slower than the coefficient matrix assembler.

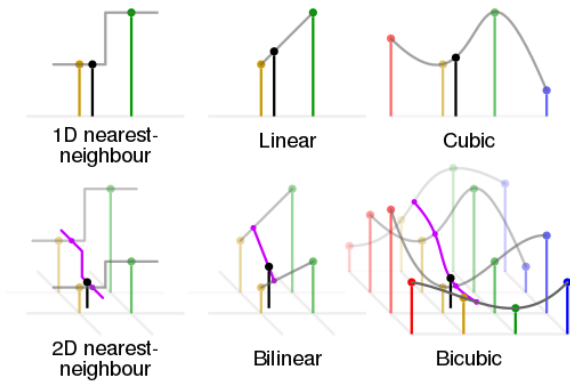


Figure 8.4: Comparison of nearest-neighbour, linear, cubic, bilinear and bicubic interpolation methods courtesy of CMG Lee [16]. The black dots correspond to the point being interpolated, and the red, yellow, green and blue dots correspond to the neighbouring samples.

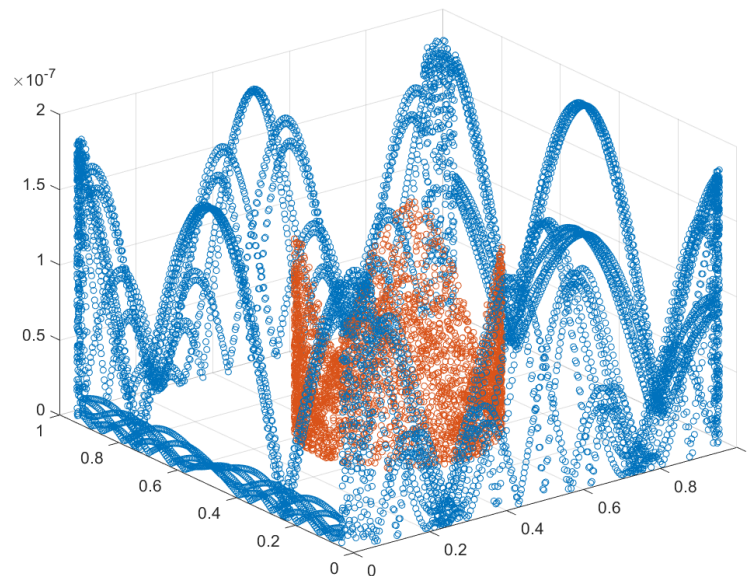


Figure 8.5: Relative Error in the Bicubic Interpolation of a sinusoidal function with 10 wavelengths per domain. Real wall nodes from the mesh shown in Figure 8.2 were used.

The objective of this complex interpolation was to induce such a small error that it could be neglected when compared to Finite Difference residuals. Figure 8.5 shows the error of the interpolation of the outer wall mesh nodes using the transition nodes. The test function is a sinusoidal wave with 10 wavelengths along the domain both in the x and y directions. The resulting relative error is on the order of 10^{-7} about 3 orders of magnitude below the error in the first derivatives induced by the Sofd3 discretization.

8.5 Expected Issues and Limitations

On preliminary studies, at least two factors were recognized that could limit the applicability of the proposed method:

- The accumulation of errors in a particular direction in the wall mesh: Specially in corners or pronounce turns, the errors in the FD approximations across nearby nodes could sum up due to the similarity in the computational cells and the expected error anisotropy produced by the deformation of the stencil. This problem is difficult to evaluate prior to the implementation of real simulations.
- The performance of the linear equation solver with a highly non-symmetric matrix of coefficients produced by interpolation and non-uniform meshes. The construction of the matrix of coefficients and mesh is also certainly slower than for *fdwaves* but the solver is still expected to be the most critical step in the simulation. Undesired performance might be tackle with the utilization of powerful solvers written in lower level programming languages (FORTRAN or C) which are expected to be significantly faster than Matlab's generic solvers.

8.6 Perfectly Matched Layer (PML)

We might be interested in avoiding 'hard wall' reflections and modeling outgoing waves traveling out of the problem domain and toward infinity. Unlike for the wave equation, a hyperbolic partial differential equation, other kinds of PDEs can rely on the function decay within the problem boundaries. In vacuum, the wave decay is slow, for spherical waves, it is proportional to the square of the distance to the source according to energy considerations [22]. We may, nonetheless, simulate plane or uni-dimensional waves having no decay at all. Although some attenuation is expected when collisions are introduced in plasma, low damping directions of propagation and wave resonance seem to make the task of avoiding reflections rather challenging. Furthermore, the thruster operation is an exemplary problem in which waves traveling to infinity, in this case downstream the thruster, should be modeled. This is clearly exposed in Figure 8.6 with the region of interest being the thruster itself.

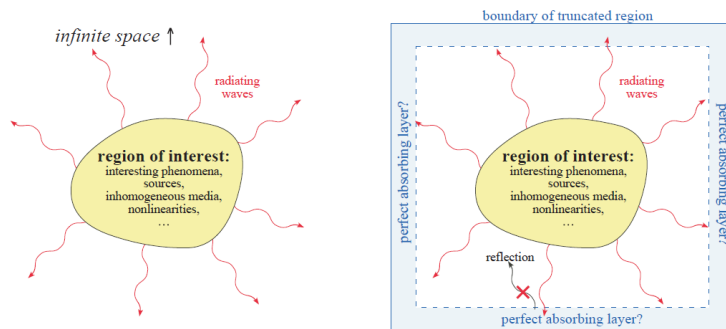


Figure 8.6: Perfectly Matched Layer (PML) boundary conditions schematic.

Perfectly matched layers [45] are the best option to avoid wall reflection. There are several formulations on PMLs derived from the original work of J.P. Berenguer [7]. Uniaxial Perfectly Matched Layer (UPML) is the most common option in modern codes. No details will be given on the mathematical construction of these boundary conditions besides that they can be implemented in frequency domain methods with a relatively simple modification of the dielectric tensor as long as inhomogeneities are kept smooth enough. Interestingly, a quite neat procedure using a complex coordinate transformation and analytical continuation before converting back to the initial basis can be used to demonstrate that PMLs work as an absorbing material on the boundaries of the domain [29]. The thickness of these layers in terms of the number of nodes and the angle of wave incidence will, eventually, determine the absorbing performance.

9 Concluding Remarks

The finite difference simulation package *fdwaves* has been successfully implemented and verified using different techniques. Propagation of electromagnetic plane waves through vacuum and homogeneous plasma can be studied in the frequency domain with a considerably high computational efficiency and short simulation times. Albeit non-homogeneous plasma modeling would, in principle, be possible with the current *fdwaves* version, this functionality was not thoroughly tested and is left for future research. Periodic and ‘hard wall’ perfect electric conductor (PEC) boundary conditions are available.

Much of the work accomplished during this dissertation might be considered State of the Art. For instance, albeit Von Neumann analysis has been used in the literature for the study of propagation in vacuum and isotropic media, there are very few studies of this kind targeting the electromagnetic problem for anisotropic plasma with resonance cones and analyzing the effect of the magnetic field orientation with respect to the mesh. An extensive in-depth analysis of the numerical error in simulations with plasma media does not exist in literature either.

The work has served to verify the utility and limits of application of FDFD to study ECRA. It has been decided to continue this path to complement a FEM code under development in the EP2 team at UC3M. The work done here involves a detailed analysis of the numerical properties of several methods. This goes beyond the state of the art in the literature, and sheds light on the problems that exist when simulating magnetized plasmas in the regime relevant to ECRA.

Elaborating deeper into the procedure followed, this dissertation was structured according to the natural process of research and development of any new technology:

- The necessity for plasma thrusters and their role for in-space propulsion were exposed. **State of the art** and the different alternative technologies were presented together with their advantages and shortcomings, out of them, electrodeless thrusters showed up to be powerful candidates for more efficient and durable propulsion systems.
- Despite their exceptional prospects, the complete comprehension of the physical phenomena and operation of the thrusters has not already been achieved and continues to be under extensive research in the preliminary phases of technology maturity with technology readiness levels TLR 4/5. One of the most critical points in the thruster operation is the electromagnetic wave propagation and absorption by plasma. The **Problem Statement** and the main objective of the present thesis was to obtain the necessary tools for the study of the wave-plasma interaction. Electromagnetic theory and its application to the specific behavior and modeling of plasma media was presented under simplifications and assumptions which were, anyhow, stated and recognized as a limitation for the accuracy of such a study.
- Among the methods available to study the proposed problem, numerical techniques arise as the most suitable **Solution Proposal** due to the complexity of the problem and the obvious difficulty to treat the governing equations analytically. Particularly, a Finite Difference and Frequency Domain method is chosen as the preferred alternative thanks to its relative simplicity while being capable of effectively simulating the study state monochromatic propagation phenomena.
- Finite difference schemes were exhaustively analyzed using von Neumann stability analysis. Boundary conditions are also studied. The **Solution Implementation** is accomplished with the *fdwaves* code. Convergence, performance and consistency were tested for vacuum and plasma simulations.
- **Results** were obtained for ‘academic’ case studies, i.e. although not aiming at analyzing a real thruster operation, they provide useful insight into important physical phenomena such as resonance. Importantly, those relatively simple simulations could be used to verify the code with analytic solutions. Moreover, some real plasma simulations were also achieved with parameters very close to the ECR operational regime.
- Finally, **Future Work** was proposed targeting a functional simulation of actual thrusters,

including complex geometric features and more realistic boundary conditions. The introduction of a future absorbing condition via a Perfectly Matched Layer is recognized as a fundamental improvement for the study of the wave-plasma interaction phenomena by means of reflection avoidance. So is the implementation of non-homogeneous meshes and, eventually, the arbitrary geometry modeling tool *fdmesher*.

The work that was presented is intended to be continued in a Master's Thesis. Besides developing the new computational tools presented in Chapter 8, an extensive simulation and analysis effort is needed. Once a powerful and efficient code is developed, it could be used to study phenomena not addressed in this thesis. In this regard, energy deposition in the medium and the plasma response would be specially interesting to study and useful for a future thruster design.

References

1. Ahedo, E. Plasmas for space propulsion. *Plasma Physics and Controlled Fusion* **53**, 124037 (2011).
2. Ahedo, E. & Navarro-Cavallé, J. Helicon thruster plasma modeling: Two-dimensional fluid-dynamics and propulsive performances. *Physics of Plasmas* **20**, 043512 (2013).
3. Allis, W. Waves in a Plasma. *Sherwood Conf. Contr. Fusion* (1959).
4. Amateur Radio Network. *Antenna Circular Polarization* Available at <http://qrznow.com/antenna-circular-polarization> (QRZnow, Amateur Radio Network).
5. Appleton, E. The influence of the Earth's Magnetic Field on Wireless Transmission. *U.R.S.I, Washington Assembly* (1928).
6. Åström, E. Magneto-Hydrodynamic Waves in a Plasma. *Nature volume 165* (1950).
7. Berenger, J.-P. A perfectly matched layer for the absorption of electromagnetic waves. *Journal of computational physics* **114**, 185–200 (1994).
8. Bonilla, L. . *Advance Mathematics Course Notes* Available at <http://scala.uc3m.es> (Material Science and Engineering Department, Universidad Carlos III de Madrid).
9. Bramanti, C., Izzo, D., Samaraee, T., Walker, R. & Fearn, D. Very high delta-V missions to the edge of the solar system and beyond enabled by the dual-stage 4-grid ion thruster concept. *Acta Astronautica* **64**, 735–744 (2009).
10. Bryce Space and Technology, LLC. *Global Space Industry Dynamics 2017* Available at https://brycetech.com/downloads/Global_Space_Industry_Dynamics_2017.pdf (Bryce Space and Technology, LLC).
11. Cameron Taylor. *Finite Difference Coefficient Calculator* Available at <http://web.media.mit.edu/~crtaylor/calculator.html> (Web Media MIT).
12. Cardinali, A., Melazzi, D., Manente, M. & Pavarin, D. Ray-tracing WKB analysis of Whistler waves in non-uniform magnetic fields applied to space thrusters. *Plasma Sources Science and Technology* **23**, 015013 (2014).
13. Choueiri, E. Y. New Dawn for Electric Rockets. *Scientific American* **300** (2009).
14. Clark, S. *Electric propulsion could launch new commercial trend* Available at <https://spaceflightnow.com/news/n1203/19boeing702sp/> (Space Flight Now).
15. Clemmow, P. & Mullaly, R. Dependence of the Refractive Index in Magneto-Ionic Theory on the Direction of the Wave Normal. *Physics of the Ionosphere, Report of the Conference held at the Cavendish Laboratory, Cambridge* (1954).
16. CMG Lee. *Interpolation Techniques* Available at https://commons.wikimedia.org/wiki/File:Comparison_of_1D_and_2D_interpolation.svg (Creative Commons License Wikimedia).
17. Collin, R. E. *Foundations for Microwave Engineering* ISBN: 0780360311 (IEEE The Institute of Electrical and Electronics Engineers, New York, 2001).
18. Crank, J. & Nicolson, P. A Practical Method for Numerical Evaluation of Solutions of Partial Differential Equations of Heat Conduction Type. *Proc. Camb. Phil. Soc* (1947).
19. Diaz, F. R. C. The VASIMR rocket. *Scientific American* **283**, 90–97 (2000).
20. Al-Ekabi, C. & Ferrerti, S. *Yearbook on Space Policy 2016* (ESPI, Springer, 2017).
21. EP2 Research Team UC3M. *MagnetIc NOzzle thruster with elecTron cyclOtron Resonance', coordinated by ONERA and financed by the European Union's Horizon 2020 Reasearch and Innovation Programe under Grant Agreement N° 730028* Available at <http://ep2.uc3m.es> (EP2 Team, Universidad Carlos III de Madrid).
22. Feynman, R., Leighton, R. & Sands, M. *The Feynman Lectures on Physics Addison-Wesley world student series v. 2.* ISBN: 9780201021172 (Addison-Wesley Publishing Company, 1965).

23. Haus, H. A. & Melcher, J. R. *Electromagnetic Fields and Energy (MIT OpenCourseWare)* Available at <https://ocw.mit.edu/resources/res-6-001-electromagnetic-fields-and-energy-spring-2008> ().
24. Higham, N. J. *Accuracy and Stability of Numerical Algorithms* (Society for Industrial and Applied Mathematics, University of Manchester, 2002).
25. Huang, S. J. & Li, F. FDTD implementation for magnetoplasma medium using exponential time differencing. *IEEE microwave and wireless components letters* **15**, 183–185 (2005).
26. Jackson, J. D. *Classical Electrodynamics* ISBN: 978-0-471-30932-1 (John Wiley & Sons, Hoboken, NJ, 1998).
27. Jahn, R. G. *Physics of Electric Propulsion* (McGraw Hill, New York, 1968).
28. Jarrige, J., Elias, P.-Q., Packan, D. & Cannat, F. *Characterization of a coaxial ECR plasma thruster* in *44th AIAA Plasmadynamics and Lasers Conference* (2013), 2628.
29. Johnson, S. G. *Notes on Perfectly Matched Layers (PMLs)* (MIT OpenCourseWare. Numerical Methods for Partial Differential Equations 18.336 Class Notes, 2010).
30. Keys, R. Cubic convolution interpolation for digital image processing. *IEEE transactions on acoustics, speech, and signal processing* **29**, 1153–1160 (1981).
31. Kuninaka, H. *et al.* Assessment of Plasma Interactions and Flight Status of the HAYABUSA Asteroid Explorer Propelled by Microwave Discharge Ion Engines. *IEEE Transactions on Plasma Science*, *34* (2006).
32. Liu, Y. Fourier Analysis of Numerical Algorithms for the Maxwell Equations. *Journal of Computational Physics* *124* (1996).
33. L.Tonks & I.Langmuir. Oscillations in Ionized Gases. *Phys. Rev.* *33*, 195 (1929).
34. Lynch, D. & Paulsen, K. Origin of Vector Parasites in Numerical Maxwell Solutions. *IEEE Transactions on Microwave Theory and Techniques*, *Vol. 39* (1991).
35. *Mechanics and Thermodynamics of Propulsion* ISBN: 9788131729519 (Pearson Education, 2009).
36. Merino, M. & Ahedo, E. Contactless steering of a plasma jet with a 3D magnetic nozzle. *Plasma Sources Science and Technology* **26**, 095001 (2017).
37. Merino, M. *et al.* *Wave Propagation and Absorption in ECR Plasma Thrusters* in *35th International Electric Propulsion Conference, No. IEPC-2017-105, Electric Rocket Propulsion Society, Fairview Park, OH* (2017).
38. Miller, D. & Bethke, G. Cyclotron resonance thruster design techniques. *AIAA JOURNAL*, *Vol. 4*, *No. 5* (1966).
39. Nyquist, H. Certain Topics in Telegraph Transmission Theory. *Trans. AIEE.* *47* (1928).
40. Riley, K. F., Hobson, M. P. & Bence, S. J. *Mathematical Methods for Physics and Engineering* ISBN: 9780521861533 (Cambridge University Press, Cambridge, UK, 2006).
41. Rylander, T., Bondeson, A. & Ingelström, P. *Computational Electromagnetics* ISBN: 978-1-4614-5351-2 (Springer, New York, 2010).
42. Saitoh, I., Suzuki, Y. & Takahashi, N. The symplectic finite difference time domain method. *IEEE Transactions on magnetics* **37**, 3251–3254 (2001).
43. Sercel, J. C. & Fitzgerald, D. J. ECR Plasma Thruster Research: Preliminary Theory and Experiments. *AIAA 25th Joint Propulsion Conference* (1989).
44. Stix, T. H. *Waves in Plasmas* ISBN: 0883188597 (Springer, New York, 1992).
45. Taflove, A. & Hagness, S. C. *Computational Electrodynamics. The Finite-Difference Time-Domain Method* ISBN: 1-58053-832-0 (Artech House, Norwood, MA, 2005).
46. The Space Report. *2017 Economic Overview* Available at <https://www.thespacereport.org/year/2017> (The Space Report Online).
47. Yee, K. S. Numerical solution of initial boundary value problems involving Maxwell's equations in isotropic media. *IEEE Transactions on Antennas and Propagation Vol.14* (1966).